Modeling the Severe Plastic and Cyclic Deformations of Structural and Biomedical Alloys by Incorporating Microstructure – Mechanical Property Relationship

by

Orkun Önal

A Thesis Submitted to the

Graduate School of Sciences and Engineering

in Partial Fulfillment of the Requirements for

the Degree of

Doctor of Philosophy

in

Mechanical Engineering

Koc University

March 2015

Koc University

Graduate School of Sciences and Engineering

This is to certify that I have examined this copy of a Ph.D. thesis by

Orkun Önal

and have found that it is complete and satisfactory in all aspects,

and that any and all revisions required by the final

examining committee have been made.

Committee Members:

Demircan Canadinç, Ph.D. (Advisor)

Murat Sözer, Ph.D.

Özgür Birer, Ph.D.

Umud Esat Öztürk, Ph.D.

Ercan Gürses, Ph.D.

Alper Uzun, Ph.D.

Date: 13.03.2015

ABSTRACT

The first aim of the work presented herein is to investigate thickness reduction in steel plate heat exchangers utilized in combi boilers. A multi-scale modeling approach was utilized to predict thickness reduction, as well as crack initiation sites due to severe plastic deformation. Specifically, texture and microstructural effects were considered with appropriate coupling of crystal plasticity and finite element analysis. The crystal plasticity simulations were carried out in order to attain appropriate multi-axial hardening rule to define the material strain hardening during forming operation. The multi-axial hardening rules were successfully incorporated into the finite element metal forming simulations. The analysis not only showed the success of multi-scale modeling approach but also demonstrated that failure of plate heat exchangers can be prevented at the design stage by predicting crack initiation sites. Furthermore, crack initiation analysis was extended to rail materials for complicated loading condition and the multi-scale modeling approach was also applied to biomedical and structural materials, in order to further verify both approaches in different materials and under different conditions.

Initially, crack initiation in rail materials (bainitic and pearlitic steel) was analyzed under rolling contact loading. In particular, analytical Jiang – Sehitoglu model was performed to predict the ratcheting and multiaxial fatigue damage in these rail steels. It was observed that bainitic rail steel withstood higher loads as compared to its pearlitic counterpart at low shear tractions. As the shear tractions ascended, the performance of rail steels became similar. Moreover, maximum damage followed by rapid crack initiation was visible in both steels when ratcheting and fatigue damage coincide on the surface. The outcome of this analysis evidences a methodology for the realistic prediction of crack initiation under the action of rolling contact loads. However, it is noted that microstructure was not considered in rolling contact loading simulations as it plays a key role on determining mechanical properties.

For investigating the microstructure-mechanical property relationship, author developed a model that bridges micro and macro scales. For this purpose, impact response of a biomedical niobium-zirconium alloy was investigated incorporating geometric and microstructural aspects utilizing multi-scale modeling approach. Specifically, the roles of texture and stress-strain distribution regarding geometry under loading were successfully accounted for by implementing a multi-axial hardening rule acquired from crystal plasticity simulations into the finite element analysis. It was observed that more reliable results were

obtained with multi-scale modeling approach when compared to those of the classical finite element approach. This analysis constituted a considerable guideline for the design stage of dental and orthopedic implants under impact loading.

In order to further investigate the effects of microstructure on the impact response, the impact behavior of high-manganese austenitic steel was analyzed utilizing multi-scale modeling approach incorporating strain rate effects. This specific steel was analyzed due to the fact that it has a very complex microstructure. A similar modeling procedure was applied to predict the impact response of this steel. The findings emphasized the need of multi-scale modeling approach for reliable impact predictions.

Overall, the results presented in this thesis shed light on the importance of multi-scale modeling approach considering microstructure for a reliable assessment of failure of plate heat exchangers. The significance of this analysis is that plate heat exchangers can be manufactured with lower costs and improved service performance. Furthermore, current work also demonstrates that implementing the gained knowledge to the biomedical and structural materials are of great importance for design procedure of new applications. With this motivation, long term usability of biomedical and structural materials is ensured. Specifically, this leads to safety of patients by eliminating serious injuries as well as bone fractures during service of biomedical materials. Moreover, the strength of structural materials in ballistic and bearing applications may be significantly enhanced.

ÖZET

Burada sunulan tezde amaç kombilerde kullanılan çelik bazlı ısı değiştiricili plakalarda kalınlık azalmasını araştırmaktır. Ağır plastik deformasyona bağlı oluşan çatlak başlangıç bölgeleri ve kalınlık azalmasını tahmin etmek için çok ölçekli modelleme yaklaşımı kullanıldı. Özellikle, sonlu elemanlar analizi ve kristal plastisitenin uygun bir şekilde birlikteliği ile doku ve mikroyapısal etkiler ele alındı. Metale form verilme işlemleri sırasında malzeme gerinim sertleşmesini tanımlamak için uygun çok eksenli sertleşme kuralı, kristal plastisite simülasyonları yardımıyla bulundu. Sertleşme kuralı bulguları, metale form verme sonlu elemanlar simülasyonlarına başarıyla ilave edildi. Analiz, sadece çok ölçekli modelleme yaklaşımının başarısını göstermekle kalmayıp, aynı zamanda ısı değiştiricili plakaların çatlak başlangıç bölgelerinin tahmin edilebilmesiyle arızalarının tasarım aşamasında önlenmesini ortaya çıkarmıştır. Bununla birlikte, çatlak başlangıç analizi, karmaşık yükleme şartları için ray malzemelerine genişletilmiştir. Çok ölçekli modelleme yaklaşımı, aynı zamanda, farklı malzemelerde ve farklı koşullar altında bu yaklaşımı doğrulamak için biyomedikal ve yapısal malzemelere de uygulandı.

İlk olarak, ray malzemelerinde (beynitik ve perlitik çelikler) çatlak başlangıcı haddeleme değme yüklemesi altında analiz edildi. Özellikle, yorulma bozunumu ve çok eksenli yorulma hasarının tahmini için analitik Jiang - Şehitoğlu modeli kullanıldı. Beynitik ray çeliğinin, perlitik eşleniğine göre düşük kayma kuvvetlerinde daha yüksek yüklemelere dayandığı gözlemlenmiştir. Kayma kuvvetleri arttığında ise ray çeliklerinin performansı benzer hale geldi. Bununla birlikte, yorulma bozunumu ve yorulma hasarı yüzeyde kesiştiği zaman, her iki çelikte de ani çatlak başlangıcı kaynaklı maksimum hasar görüldü. Bu analizden çıkan sonuç, haddeleme değme yükleri altında çatlak başlangıcının gerçekçi tahmini için bir metodolojiyi göstermektedir. Ayrıca, haddeleme değme yüklemeleri simülasyonlarında mekanik özellikleri belirlemede kilit role sahip mikroyapının dikkate alınmadığı not edilmelidir.

Mikroyapı-mekanik özellik ilişkisinin incelenmesi için, yazar mikro ve makro boyutu birleştiren bir model geliştirdi. Bu amaç için, çok ölçekli modelleme yaklaşımı kullanılarak geometrik ve mikroyapısal yönlerin ilave edilmesiyle biyomedikal Niyobyum-zirkonyum alaşımının darbe tepkisi araştırıldı. Özellikle, kristal plastisite simülasyonlarından elde edilen çok eksenli sertleşme kuralının sonlu eleman analizine ilave edilmesiyle, geometriyle bağlantılı olarak doku ve gerilim-gerinim dağılımlarının rolü hesaba katıldı. Çok ölçekli

modelleme yaklaşımı ile elde edilen sonuçların, klasik sonlu eleman yaklaşımı ile elde edilen bulgulara göre daha güvenilir olduğu gözlemlendi. Bu analiz, diş ve ortopedik implantların darbe yüklemeleri altındayken tasarım aşaması için önemli ölçüde rehberlik gösterdi.

Mikroyapının darbe tepkisine etkilerini daha fazla incelemek için, yüksek oranda mangan içeren östenitik çeliğin darbe davranışı, çok ölçekli modelleme yaklaşımına gerinim hızı etkileri ilave edilerek incelendi. Bu özel çelik çok karmaşık bir mikroyapıya sahip olduğu için analiz edildi. Bu çeliğin darbe tepkisini tahmin etmek için benzer bir modelleme prosedürü uygulandı. Bulgular, güvenilir darbe tahminleri için çok ölçekli modelleme yaklaşımının ihtiyacını vurguladı.

Sonuçta, bu tezde belirtilen sonuçlar, ısı değiştiricili plakaların hasarlarının güvenli bir şekilde değerlendirilmesi için, çok ölçekli modelleme yaklaşımına mikroyapının ilavesinin önemine ışık tutmaktadır. Bu analiz, ısı değiştiricili plakaların düşük masraflar ve geliştirilmiş servis performanslarıyla üretilebilir olmasını ortaya çıkarmaktadır. Bununla birlikte, bu çalışma, aynı zamanda kazanılan bilginin biyomedikal ve yapısal malzemelere ilave edilmesinin yeni uygulamaların tasarım prosedürü için çok önemli olduğunu göstermiştir. Bu amaçla, biyomedikal ve yapısal malzemelerin uzun dönem kullanılabilirliği sağlanır. Özellikle bu durum, biyomedikal malzemelerin kullanımında ağır sakatlanmaları ve kemik kırılmalarını önleyerek hasta güvenliğini sağlar. Ayrıca, yapısal malzemelerin balistik ve rulman uygulamalarındaki dayanımı önemli ölçüde artabilir.

ACKNOWLEDGMENTS

First of all, I would like to thank my advisor Dr. Demircan Canadinç for his supervision and extraordinary guidance throughout my PhD studies. I had a great opportunity to work with such a perfect advisor. His continuous trust, encouragement and inspiration made my PhD studies much easier than I expected. He was also a brother to me with giving advice about any issue in daily life. I will always remember him not only as a PhD advisor but also as a great person.

I would like to thank gratefully to my thesis progress committee members; Dr. Murat Sözer and Dr. Özgür Birer for their considerable guidance and valuable comments throughout my PhD thesis. I also would like to express my gratitude to my dissertation committee members; Dr. Demircan Canadinç, Dr. Murat Sözer, Dr. Özgür Birer, Dr. Umud Öztürk, Dr. Ercan Gürses and Dr. Alper Uzun for their participation.

I would like to send my special thanks to Prof. Dr. Ing Hans Jurgen Maier, for letting me visit his research group in Paderborn. I learned a lot from him and his group members; Dr. Thomas Niendorf, Dr. Felix Rubitschek. I also would like to thank my close friends, Dr. Martin Joachim Holzweissig and Dr. Ante Kurtovic, for their support and valuable friendship. I feel lucky to have the chance to be a part of this research group.

I would like to express my gratitude to all Advanced Materials Group (AMG) members by starting one by one. I would like to thank Dr. Sıdıka Mine Toker, my first officemate, for her friendship and support. I would like to thank to Berkay Gümüş, the guy who has a broad knowledge about anything in life, for his friendship and presence. I am thankful to Burak Bal, my exciting basketball and playstation partner, for his friendship and sincerity. I also would like to thank Morad Mirzajanzadeh, Benay Uzer and Cemre Özmenci for their friendship.

I would like to express my sincere gratitude to my cousin Dr. Şükrü Ercan. His presence has always been the source of motivation and happiness to me. He was my life coach for my important decisions and helped me a lot psychologically. I would like to pay tribute to my hearty friend Caner Nazli for his support, advice and friendship. We have spent great years with many memories. I feel very lucky to meet another close friend Dr. Mustafa Uğur Arıdoğan at Koc University. I will miss our discussions in “Takanik” fish restaurant. I also would like to thank my old friend from undergrad, Serkan Balli. I called him whenever I was in trouble during my PhD study. I would like to send special thanks to my friends Berkin

Takalay, Burak Özen, Erdal Aydın, Esra Durmaz and Özgecan Balaban. They were not just my friends but were also great activity partners to me.

Finally, I would like to thank my parents, Şener Önal and Ayten Önal and my grandmother, Nuran Önal. Their guidance and endless love help me to achieve my goals. Their presence makes me always feel safe; their ideas are always taken into account by me. I cannot thank them enough for their unlimited support for my PhD study.

TABLE OF CONTENTS

LIST OF TABLES

LIST OF FIGURES

CHAPTER 1: INTRODUCTION

The metal forming is a widespread manufacturing technique in which the workpiece is transformed into a product for specific use under the action of extensive loads. The final product possesses well defined shape - size, appearance and properties [1]. The metal forming operations are classified into compressive, tensile, combined tensile and compressive forming depending on the amount of stresses attained. The compressive forming consists of rolling, extrusion and die forming; the tensile forming implies stretching while the combined forming involves deep drawing [2].

One of the most commonly used metal forming operations is die forming in which the material is pressed between dies prior to assembly. The pressing time is usually short such that a single stroke or a number of strokes is applied on the workpiece [1]. In terms of the materials' selection, the die is usually a block made of metallic materials (e.g. steel) while the workpiece could be metal or plastic as sheets.

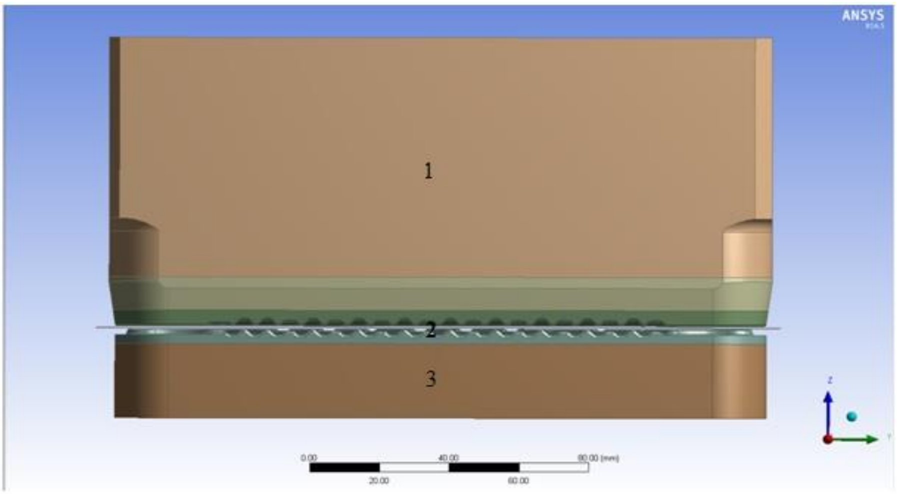

Figure 1. 1 Schematic illustration of a die forming process (1: upper die, 2: workpiece 3: lower die) After [3].

The major concerns involved in die forming are the workpiece material, die conditions, and the workpiece – die interface. One of the important factors for forming operations regarding the workpiece material is the flow stress. The flow stress refers to the required amount of stress for the continuation of plastic deformation at a certain strain. The flow stress increases for most materials during the metal forming operation with increasing plastic strain. Further increase in flow stress may give way to the sudden material failure as it is nearly impossible to deform a material beyond a certain flow stress. The parameters involved in the forming operation, such as strain rate, temperature and microstructure of the workpiece, considerably influence the flow stress. Specifically, these parameters have a major effect on dislocation density in the microstructure. It is known that dislocations are carriers of plastic deformation and play a key role to determine the mechanical properties of the materials. For instance, higher density of dislocations results in material hardening, ascending the strength values. Hence, the accurate prediction of metal flow is crucial, such that accurate material properties should be used as input [1]. These parameters were specifically addressed in recent studies by developing empirical methods [4,5]. In this approach, flow rules under isothermal conditions were found in order to consider thermal and microstructure effects in the forming operation.

In most metal forming processes dies are rigid such that the strains induced in the dies are assumed to be zero. On the other hand, forming process may cause considerable deformations especially at the interface between the die and the workpiece material [1]. A recent study investigated the effects of stress and strain on the die during metal forming with a numerical procedure, aiming to increase the effectiveness of the die [6]. It has been found that accumulated stress on dies had a significant effect on their lifetime. Therefore, a stress relaxation procedure has been introduced with modifying die geometry in order to increase die life [6]. Additionally, die shape (design) is crucial in metal forming processes. It determines the quality of the final product by forming the workpiece directly [7]. Specifically, the high quality is obtained with the elimination of mechanisms leading to material failure such as thermal distortions, excessive deformation as well as springback effects [8].

The interface conditions, specifically friction and heat transfer between the die and the workpiece, greatly influence the material flow as well as the magnitude of loads required to form the workpiece. One should note that the friction coefficients are not constant throughout the metal forming operation. This is mainly due to the temperature alterations at the contact region between the workpiece and the die [1]. Much research has been carried out to analyze the friction phenomenon for both cold and hot metal forming [9-11]. A method has been developed such that shear friction factor was computed utilizing a backward extrusion – type process. In this method, the forging load was multiplied by the thickness in the process which was taken as the friction sensitive parameter. The forging loads multiplied by the thickness vs.

reduction in height of the billet curves were plotted and successfully implemented into the FE simulations to determine the shear friction factor. The power of this method relies on the fact that the shear friction factor can be calculated continuously during cold forming operations [9]. A friction test regarding double backward extrusion process was utilized in a study. Specifically, the punch was allowed to rotate regarding the workpiece and the die was maintained under a certain load. The friction test was conducted at a temperature range of 20 – 270 ^{0} C with an allowed and controlled surface expansion. The friction test results revealed important findings about the lubrication and friction performance under the action of the temperature during metal forming process [10]. For instance, lubricant performance has been shown to reduce gradually when temperature exceeds 30 ^{0} C. This has been found to be due to the frictional heat leading the breakdown of the lubricant film at high temperatures. It has been also found that the friction is inversely proportional to the temperature when the temperature is within 30 – 150 ^{0} C range. However, the friction increases significantly when the temperature range is exceeded.

The aforementioned concerns in the metal forming may lead to significant manufacturing restrictions as the metal forming processes result in improved strength and reduced thickness [12]. In order to reduce manufacturing costs and improve the accuracy of the metal forming process, finite element analysis (FEA) has come into picture in the last years [13-15]. The FEA is defined as a numerical method of piecewise polynomial approximation to solve governing differential equations. Specifically, the differential equations are converted into a form of matrix equations. However, creating these algebraic equations for the whole domain (solid) is nearly impossible, so that the complex solid is discretized [16]. The discretization method has several advantages such that the complex solid is represented precisely, total solution is visualized readily and local effects of loading on the solid are determined [17]. It is noted that the accuracy of the FEA is significantly improved with increasing number of elements. After discretization, the properties of the each element are formulated in order to obtain finite element model. As the modeling step is completed, known loads (i.e. nodal forces and moments) and support structures (i.e. nodal displacements) are applied [18]. Hence, displacements, stresses and strains of the materials subjected to various loading scenarios are computed utilizing FEA. The major advantage of the FEA software techniques is that expensive error and trial processes arising from the real tools can be prevented as this is carried out with the help of analytical tools [12]. However, many parameters are required for the sake of accuracy and microstructural features (i.e slip/twin mechanism) are not considered in the classical FE method [18].

On the other hand, FE simulation of a forming operation is carried out within the limits of geometrical considerations which are significantly affected by sheet metal thickness reductions. The workpiece material should be thoroughly analyzed during forming process especially when the sheet metals are high – strength materials such as stainless steel. This is due to the fact that high strength materials possess high formability leading to significant variation of thicknesses after forming [19]. However, apart from thickness variation parameter, other parameters such as wrinkling and springback can be simulated with the FE techniques.

There are plenty of FEA based studies concerning the thickness reduction (thinning) especially in sheet metal forming processes [20-24]. Major part of these studies focus on aluminum (Al), copper (Cu) and steel materials. For instance, thickness distribution and forming forces for the thin copper sheets (less than 1 mm) were investigated in sheet forming operation by developing a complete parametric toolbox [20]. The parametric toolbox was developed in order to overcome the disadvantages of the sheet metal forming such as the presence of defects and long simulation times [20]. It has been also found that the twisting phenomenon has a significant effect on obtained numerical thickness evolution [20]. However, the obtained results correspond well with the sine rule [21]. Similarly, thinning evolution of aluminum sheets with a thickness of 1 mm and 1.25 mm was computed in forming utilizing FEA. The conventional metal forming may cause localized deformation on the workpiece materials whereas the profile forming leads to higher formability [22]. It has been demonstrated that the thin sheet had a reduced wall after forming operation leading to a larger springback compared to its thick counterpart. Furthermore, thin sheet has a better surface finish in comparison with the thick sheet. This is due to a restriction in material flow with decreasing thickness [22]. A similar recent study on Al sheets that are utilized in aerospace applications shed light on the final thickness distribution in the super plastic forming operation with the help of FEA. Specifically, the strain rate sensitivity was incorporated into the FE codes for the purpose of predicting the superplastic deformation behavior of the workpiece regarding the flow stress. It has been observed that the thickness reduction at the center of the material was more pronounced compared to that of the other regions. It has been also found that the numerical findings on thickness distribution stand in good agreement with the experimental results [23].

In addition to the significant amount of work performed with the FEA, there exist few studies concerning the coupling of crystal plasticity formulations with the FE models. The main advantage of this approach is the ability of dealing with the mechanical problems under complicated loading scenarios. Furthermore, this approach is able to predict plastic flow as well as hardening at both scales (micro/macro) by utilizing constitutive formulation. The applications of this approach at the macroscale include many sheet metal forming problems [25]. For instance, forming simulation of 1 mm thick Al sheets was conducted in order to predict the macroscopic yield surface [26]. It is well known that the macroscopic yield surface has a significant influence on the forming limit diagrams hence the formability of sheet metals [27]. Specifically, a plasticity model [28] incorporating electron backscatter diffraction (EBSD) data, initial texture findings and uniaxial tensile deformation response utilizing crystal plasticity algorithm were successfully implemented into the FE simulations. In a similar approach, the earing profile of Al sheets during deep drawing with different textures was investigated in complex metal forming utilizing FEA [29]. Particularly, the texture information obtained by the EBSD measurements was incorporated into the rate dependent crystal plasticity. It was observed that the computational time significantly decreases with this algorithm as compared to the other works [29]. In relation to this approach, the deformation behavior of the dual phase sheet steel that is used in automotive applications under the action of non – proportional loads was analyzed utilizing FEA in order to predict the springback mechanism and failure [30]. This was carried out in order to shed light on the poor formability of these steels. Particularly, the uniaxial tensile test information, the role of deformation texture and microstructural evolution were successfully incorporated into the crystal plasticity simulations. It has been demonstrated that the accurate prediction of the deformation behavior with crystal plasticity – FEA was possible. [30].

The crystal plasticity coupled with FEA based studies at macroscale in sheet metal forming mainly focus on springback mechanism, texture evolution and material fracture [25]. However, among these studies, few of them concentrate on the thickness distribution of sheet metals or alloys. For instance, the formability properties with an emphasis on thickness distribution of cold – rolled and annealed Al sheet with a thickness of 1 mm in deep drawing was analyzed utilizing FEA [31]. Specifically, the role of anisotropy was incorporated into the FE simulations with the help of fourth – order strain rate potential based on Taylor model. It has been found that thickening of the workpiece was observed at the early stage of deformation whereas the thickening was visible around the edges towards the end of forming process [31]. Similarly, the earing profile of Al alloy sheets was investigated in forming operation utilizing FEA in conjunction with the crystal plasticity algorithm [32]. The improvement of the method compared to others was that initial texture as well as texture evolution was taken into account. It has been demonstrated that the final thickness distribution followed the general plane strain condition [32].

Most of the aforementioned efforts have been carried out in order to predict the failure of the materials, especially under cyclic loading. Specifically, the cracks initiate and propagate with number of cycles leading to the catastrophic failure. The metal forming operation increases the strength values of the sheet materials on one hand but decreases the ductility on the other. In other words, the material fails instead of bend under excessive deformation values including cyclic loads [33]. Specifically, stress states with number of cycles give way to micro – damage and micro – voids leading to the crack initiation. This significantly restricts the service life of the sheet metals [34, 35]. In order to extend the service life of the materials and improve their material design, modeling of crack initiation is of great importance [36]. Thus, the problem of crack initiation has been the major subject in various studies [37 – 39]. The analytical models utilized in these studies simulate elastic – plastic deformation behavior of nonlinear materials. They are superior over FE models, such that these models require less computation time [36]. A crack initiation model was introduced by Merwin and Johnson and it has been made an assumption that the total strains could be computed from the elastic strain fields. The main advantage of the model was to predict the accumulated residual stresses, as well as predicting the amount of displacement of the surface in the forward direction of motion [37]. A similar model developed by Hearle and Johnson predicted the plastic material flow under the action of fatigue loading. Specifically, dislocation sheets were considered in the simulations in order to determine the plastic deformation zones. The interactions between the dislocations were only analyzed at a steady state leading to less computation efforts. This was achieved with reducing significant number of computational increments. The Hearle and Johnson model predicts the forward flow more precisely than that of the Merwin and Johson model. This is due to the fact that the Hearle and Johnson model considers the non – plane strains as well as cyclic hardening response of the materials [38]. For the purpose of eliminating the disadvantages of these models, Jiang and Sehitoglu developed a model considering multiaxial fatigue mechanism including normal and shear stress ranges [39, 40]. This model has more precision over other models in terms of crack initiation as non – proportional loading scenario and non – linear kinematic hardening rule are included [39, 41].

The current study was motivated by the need to investigate the thickness reduction in the plate heat exchangers (PHE’s) during their manufacturing process by incorporating the anisotropy and microstructural effects and to model the crack initiation with Jiang and Sehitoglu model. By this way, undesired mechanical failure of the PHE’s can be prevented at the design stage such that potential fatal failure during service can be eliminated. Plate heat exchangers utilize metal plates for the purpose of transferring heat between the fluids (Figure 1.2). These metal plates are located in pairs and are opposite to each other (Figure 1.3). The side-view of these plates demonstrates a honey comb structure. The plates have corrugations on the top surface as these corrugations lead to flow turbulence and increase the heat transfer efficiency. It is noted that the arrangement of the plates is crucial in the design step such that the mixture of the fluids is circumvented. The major advantages of the PHE’s are as follows: Compactness, high area to volume ratio, design flexibility and ease of operation. The size of the PHE’s is relatively small and consumes low energy. The design flexibility of a plate heat exchanger offers significant cost reduction in terms of operation and maintenance. Furthermore, they can be used in various industrial applications due to their compact form [42].

Figure 1. 2 An example of a steel plate heat exchanger

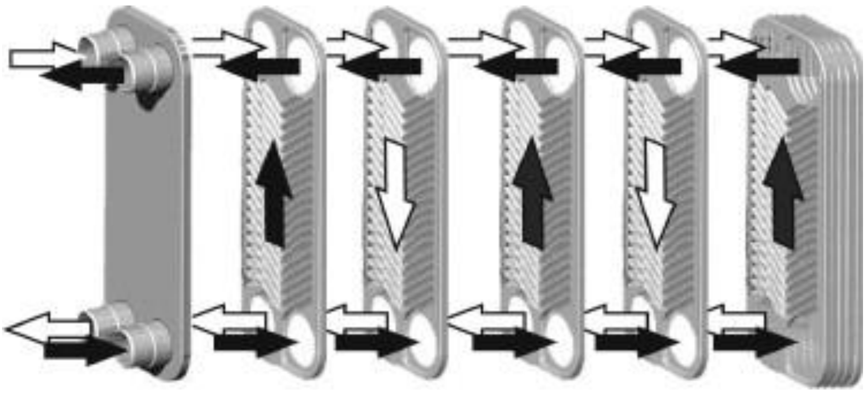

Figure 1. 3 Arrangement of the PHE's during operation (where black arrow refers to the hot water while the white arrow corresponds to the cold water) [43].

The PHE's utilized in the current study consists of stainless steel plates coupled with its copper counterpart in a sandwich structure. The forming operation mainly constitutes complicated deformation on the PHE's. Particularly, the deformation process includes large plastic strains, contact (steel – Cu) and friction between the mating materials. Contact and friction between the mating materials, as well as between the die and materials considerably influence the stress – strain distribution. However, this situation may be more complicated such that determination of the material flow becomes difficult under these conditions. As the stress concentration increases in the interface zone of the two materials, microscopic failure, crack initiation as well as crack propagation leading to catastrophic failure becomes crucial for the PHE's. Furthermore, localized stresses and strains on the die – material and material – material surfaces may give way to significant distortions and asymmetries in the final product. The localized stresses and strains during forming operation are the indication of severe plastic deformation. These problems cause local reduction in thickness throughout the PHE's, bringing about perfect locations for crack initiation sites. This restricts the service life of PHE's and increases the manufacturing costs significantly.

In order to predict thickness reduction and crack initiation sites, a multi – scale approach has been developed by the authors. Specifically, a combined numerical and experimental approach is presented in the study presented herein. For this purpose, a powerful crystal plasticity algorithm called Visco - Plastic Self - Consistent (VPSC) has been performed to determine the appropriate hardening rule for both materials by considering the role of microstructure and anisotropy. It should be noted that VPSC is an efficient simulation tool that can predict the hardening response as well as texture evolution of the materials regarding the experimental results. Once the accurate formulation is established and is successfully correlated with the experimental findings, this crystal plasticity can predict the deformation behavior under the action of any type of loading [44]. It should be noted that accurate prediction of the hardening rule is critical in the simulations as it defines the material plastic flow. In the light of this approach, sheet metal forming analysis was performed with FEA once hardening rule of both materials was successfully implemented into the FEA utilizing crystal plasticity modeling. Specifically, the evolution of stresses and strains as well as their distributions were analyzed leading to monitor the weak sections of the PHE's. In other words, weak spots ideal for crack initiation were predicted as these regions exhibited maximum thickness reduction. The simulation results were compared with the experimental data and it has been observed that the simulation results corresponded well with the experimental data. More importantly, designation of new PHE's as a result of reducing costs and establishment of multi – scale investigated deformation model based on microstructure under various loading types can be made.

Chapter 2 covers the experimental and numerical analysis of thickness reduction and crack initiation in steel plate heat exchangers subjected to the cold forming. Specifically, a multiaxial modeling approach was performed for the purpose of predicting thickness reduction in steel PHE's. The incorporation of the role of anisotropy and microstructural effects were considered by proper coupling of crystal plasticity and FE analysis. The crystal plasticity modeling was utilized to predict the appropriate multi-axial hardening response which was defined as the material flow rule for forming operation. This was successfully incorporated into the FE forming simulations for accurate crack initiation predictions.

The gained crack initiation knowledge in chapter 2 was extended to rail steels in chapter 3. This chapter details the investigation of fatigue performance of the two rail steels (J6 bainitic steel and the head hardened pearlitic steel) under cyclic rolling contact loading. The semi analytical Jiang – Sehitoglu (JS) plasticity model which incorporates both ratchetting and fatigue damage was successfully utilized in order to predict crack initiation under rolling contact.

Unlike JS plasticity model utilized in chapter 3, the author developed a multi-scale model in chapter 4. Specifically, this chapter deals with the application of multiscale modeling approach to the impact response of a biomedical Niobium – Zirconium (Nb-Zr) alloys. The multiscale modeling approach successfully incorporates the microstructural effects as well as the role of anisotropy. In the light of this approach, the macroscopic impact response of the two variants (ultrafine - grained microstructure and coarse – grained microstructure) of the NbZr alloy was explained in detail. This was carried out with the FEA incorporating hardening laws obtained from the crystal plasticity modeling.

The gained knowledge in chapter 4 was successfully improved in chapter 5. This chapter discusses the multi-scale modeling of the impact response of a strain-rate sensitive high-manganese austenitic steel. The effects of texture, geometry and strain rate sensitivity were accounted for by appropriate coupling of crystal plasticity and finite element modeling. In particular, crystal plasticity simulations were carried out to acquire the multi-axial hardening behavior at different strain rates regarding the experimental deformation behavior under the action of uniaxial tensile loads. The equivalent deformation behavior was then implemented into the FE simulations in terms of hardening rule under the action of impact loads.

Finally, the contributions of the work presented in this thesis are summarized in Chapter 6. Specifically, the important contributions to literature and the implications for future work and practical utility of the knowledge gained throughout this PhD work were presented in a concise form.

1.1 References

[1] T. Altan, V.Vazquez, Numerical process simulation for tool and process design in bulk metal forming, CIRP Annals – Manufacturing Technology 45 (1996) 599

[2] K. Lange, Handbook of Metal Forming. McGraw-Hill, Inc. on behalf of the Society of Manufacturing Engineers, 1985

[3] Metal Forming Virtual Simulation Lab, Dayalbagh Educational Institute, Agra

[4] G. Shen, S.L. Semiatin and T. Altan, Investigation of flow stress and microstructure development in nonisothermal forging of Ti-6242, Journal of Materials Processing Technology 36 (1993) 303

[5] G. Shen, S.L. Semiatin, E. Kropp and T. Altan, A technique to compensate for temperature history effects in the simulation of non-isothermal forging processes, Journal of Materials Processing Technology 33 (1992) 125

[6] T. Altan, M. Knoerr, Application of the 2D finite element method to simulation of cold-forging processes, Journal of Materials Processing Technology 35 (1992) 275

[7] N. Kim, K. K. Choi and J. S. Chen, Die shape design optimization of sheet metal stamping process using meshfree method, International Journal of Numerical Methods in Engineering 51 (2001) 1385

[8] B. Lu, H. Ou, H. Long, Die shape optimisation for net-shape accuracy in metal forming using direct search and localised response surface methods, Structural and Multidisciplinary Optimization 44 (2011) 529

[9] G. Shen, A. Vedhanayagam, E. Kropp, and T. Altan, A method for evaluating friction using backward extrusion type forging, Journal of Materials and Processing Technology 33 (1992) 109

[10] N. Bay, O. Wibom and J.A. Nielsen, A new friction and lubrication test for cold forging, CIRP Annals – Manufacturing Technology 44 (1995) 217

[11] A. Buschhausen, K. Weinmann, J.Y. Lee and T. Altan, Evaluation of lubrication and friction in cold forging using double backward-extrusion process, Journal of Materials and Processing Technology 33 (1992) 95

[12] J. Gronostajski, A. Matuszak, A. Niechaiowicz, Z. Zimniak, The system for sheet metal forming design for complex parts, Journal of Materials Processing Technology 157 (2004) 502

[13] Z. Zimniak, Problems of multi – step forming sheet metal process design, Journal of Materials Processing Technology 106 (2000) 152

[14] A. Makinouchi, Sheet metal forming simulation in industry, Journal of Materials Processing Technology 60 (1996) 19

[15] S.K. Panthi, N. Ramakrishnan, K.K. Pathak, J.S. Chouhan, An analysis of springback in sheet metal bending using finite element method (FEM), Journal of Materials Processing Technology 186 (2007) 120

[16]J.E. Akin, Finite element analysis concepts via SolidWorks,Rice University, Houston, US A

[17] J.N.Reddy, An introduction to the finite element method (third edition), (2005) McGraw-Hill.

[18] R.D. Cook, D.S. Malkus, M.E. Plesha, Concepts and applications of finite element analysis, 3rd Edition, Wiley, New York, USA

[19] N. Mole, G. Cafuta, B. Stok, A 3D forming tool optimisation method considering springback and thinning compensation, Journal of Materials Processing Technology 214 (2014) 1673

[20] S. Thibaud, R.B. Hmida, F. Richard, P. Malecot, A fully parametric toolbox for the simulation of single point incremental sheet forming process: Numerical feasibility and experimental validation, Simulation Modelling Practice and Theory 29 (2012) 32

[21] J. Reagan, E. Smith, Metal Spinning, (1993), 80 p., Bruce Publishing, New York,

[22] S.P. Shanmuganatan, V.S. Senthil Kumar, Experimental investigation and finite element modeling on profile forming of conical component using Al 3003(O) alloy, Materials and Design 36 (2012) 564

[23] V.S. Senthil Kumar, D. Viswanathan, S. Natarajan, Theoretical prediction and FEM analysis of superplastic forming of AA7475 aluminum alloy in a hemispherical die, Journal of Materials Processing Technology 173 (2006) 247

[24] M. Firat, B. Kaftanoglu, O. Eser, Sheet metal forming analyses with an emphasis on the springback deformation, Journal of Materials Processing Technology 196 (2008) 135

[25] F. Roters, P. Eisenlohr, L. Hantcherli, D.D. Tjahjanto, T.R. Bieler, D. Raabe, Overview of constitutive laws, kinematics, homogenization and multiscale methods in crystal plasticity finite-element modeling: Theory, experiments, applications, Acta Materialia 58 (2010) 1152

[26] K. Inal, R.K. Mishra, O.Cazacu, Forming simulation of aluminum sheets using an anisotropic yield function coupled with crystal plasticity theory, International Journal of Solids and Structures 47 (2010) 2223

[27] J. Lian, F. Barlat, B. Baudelet, Plastic behavior and stretchability of sheet metals. II. Effect of yield surface shape on sheet forming limit, International Journal of Plasticity, 5 (1989) 131

[28] R.J. Asaro, A. Needleman, Texture development and strain hardening in rate dependent polycrystals, Acta Metallurgica 33 (1985) 923

[29] H. Zhang, X. Dong, Q. Wang, Z. Zeng, An effective semi-implicit integration scheme for rate dependent crystal plasticity using explicit finite element codes, Computational Materials Science 54 (2012) 208

[30] R.K. Verma, P. Biswas, T. Kuwabara, K. Chung, Two stage deformation modeling for DP 780 steel sheet using crystal plasticity, Materials Science & Engineering A 604 (2014) 98

[31] J. Hu, J.J. Jonas, T. Ishikawa, FEM simulation of the forming of textured aluminum sheets, Materials Science and Engineering A 256 (1998) 51

[32] I. Tikhovskiy, D. Raabe, F. Roters, Simulation of earing during deep drawing of an Al – 3% Mg alloy (AA5754) using a texture component crystal plasticity FEM, Journal of Materials Processing Technology 183 (2007) 169

[33] F. Xue, F. Li, J. Li, M. He, Z. Yuana, R. Wanga, Numerical modeling crack propagation of sheet metal forming based on stress state parameters using XFEM method, Computational Materials Science 69 (2013) 311

[34] D. Jha, A. Banerjee, A cohesive model for fatigue failure in complex stress-states, International Journal of Fatigue 36 (2012) 155

[35] A. P. Vassilopoulos, R. Sarfaraz, B. D. Manshadi, T. Keller, A computational tool for the life prediction of GFRP laminates under irregular complex stress states: Influence of the fatigue failure criterion, Computational Materials Science 49 (2010) 483

[36] O. Onal, D. Canadinc, H. Sehitoglu, K. Verzal and Y. Jiang, Investigation of rolling contact crack initiation in bainitic and pearlitic rail steels, Fatigue & Fracture of Engineering Materials & Structures, 35 (2012) 985

[37] J.E. Merwin, K.L. Johnson, An analysis of plastic deformation in rolling contact, Proceedings of the Institution of Mechanical Engineers 177 (1963) 676

[38] A. D. Hearle, K. L. Johnson, Cumulative plastic flow in rolling and sliding line contact, ASME Journal of Applied Mechanics 54 (1987) 1

[39] Y. Jiang, H. Sehitoglu, A model for rolling contact failure, Wear 224 (1999) 38

[40] Y. Jiang, H. Sehitoglu, Modeling of cyclic ratchetting plasticity, Part I: Development of constitutive relations, Journal of Applied Mechanics, 63 (1996) 720

[41] J. W. Ringsberg, Life prediction of rolling contact fatigue crack initiation, International Journal of Fatigue 23 (2001) 575

[42] M.S. Khan, T.S. Khan, M.C. Chyu, Z.H.Ayub, Evaporation heat transfer and pressure drop of ammonia in a mixed configuration chevron plate heat exchanger, International Journal of Refrigeration 41 (2014) 92

[43] A. Michel, A. Kugi, Accurate low-order dynamic model of a compact plate heat exchanger, International Journal of Heat and Mass Transfer 61 (2013) 323

[44**]** D. Canadinc, H. Sehitoglu, H.J Maier, P. Kurath, On the incorporation of length scales associated with pearlitic and bainitic microstructures into a visco-plastic self-consistent model. Materials Science and Engineering A 485 (2008) 258

CHAPTER 2: EXPERIMENTAL AND NUMERICAL EVALUATION OF THICKNESS REDUCTION IN STEEL PLATE HEAT EXCHANGERS

2.1 Introduction

Metal forming covers a variety of processing techniques which transform the workpiece into a product for specific use under the action of extensive loads that induce plastic deformation. The forming conditions, and especially the applied loading, are significantly influenced by various parameters, such as the workpiece material, die conditions, and the workpiece – die interface, since any misadjustment of these parameters may result in an excessive increase of the flow stress, and thereby, catastrophic failure of the workpiece. Even though dies are mostly considered to be rigid, and thus, free of plastic deformation, they indeed suffer severe plastic deformations especially at the die – workpiece interface [1].

The die – workpiece interface parameters, such as heat transfer and friction, play a major role on the material flow in both the workpiece and the die. Specifically, friction coefficient varies during the metal forming process, and considerable temperature changes are observed within the die – workpiece interface [1]. This, in turn, leads to an inhomogeneous distribution of plastic strains and brings about significant restrictions on the metal forming processes that provide improved strength and reduced thickness [2]. In particular, attaining the desired thickness reduction in a relatively short time but in a homogeneous manner as required by the original design is very critical in workpieces operating under the action of thermal and mechanical loads. An example to this case is plate heat exchangers (PHEs) utilized in combi boilers, which are subject to cyclic thermo-mechanical loading. Any process related inhomogeneity in the plate thickness could severely alter the service life of the PHEs, such that zones of reduced thickness constitute ideal locations for crack initiation and cyclic damage. Therefore, prevention and prediction of thickness reduction upon metal forming operations becomes of utmost importance.

In addition to large plastic strains, the forming operation utilized to manufacture PHEs involves contact and friction between the mating materials (PHE material steel and copper (Cu) as the lubricant during the forming), and between the die and materials, which considerably influences the stress – strain distribution during and following the process. As the stress concentration increases at the mating material and workpiece material – die interfaces, microscopic failure, and thus, crack initiation become more prevalent.

Furthermore, localized stresses and strains on the die – material and material – material contact surfaces may give way to significant distortions and asymmetries in the final product, eventually leading to unexpected local reductions of the thickness throughout the PHE. This, in turn, increases the overall manufacturing cost of PHEs since the defected PHEs have to be replaced with flawless ones, increasing the total number of plates manufactured and volume of material used.

In order to reduce manufacturing costs and improve the accuracy of the sheet metal forming processes, finite element analysis (FEA) utilized [3-5]. In general, metal forming simulations utilizing FEA are carried out within the limits of geometrical considerations which are significantly affected by sheet metal thickness reductions [6-10]. For instance, a study on Al sheets [9] shed light on the final thickness distribution in the metal forming operation with the help of FEA. It was reported that the thickness reduction at the center of the material was more pronounced compared to other regions of the workpiece, which was attributed to the limited material flow at the central regions, which were also reported to be more critical in terms of crack nucleation.

In addition to the significant amount of work performed with the FEA, there exist few studies coupling crystal plasticity and FE models to predict thickness reduction in metal forming operations. The main advantage of this approach is its capability to deal with the mechanical problems under complicated loading scenarios. Furthermore, this approach is also capable of predicting plastic flow, as well as hardening, at both microscopic and macroscopic scales. The applications of this approach at the macroscopic scale include various sheet metal forming problems [11]. For instance, forming simulation of 1 mm thick Al sheets were conducted in order to predict the macroscopic yield surface [12]. It is well known that the macroscopic yield surface has a significant influence on the forming limit diagrams, and hence the formability of sheet metals [13]. Specifically, a crystal plasticity model developed in a study was utilized to incorporate initial texture and uniaxial tensile deformation response into the FE simulations, in order to predict both strain hardening and texture evolution throughout deformation [14]. The notable outcome was that sheet necking could be successfully predicted utilizing this model for both isotropic and strongly textured sheet metals.

Similarly, the deformation behavior of the dual phase sheet steel that is used in automotive applications was analyzed under the action of non – proportional loads utilizing

FEA in order to predict the springback mechanism and failure that are responsible for the poor formability of these steels [15]. Particularly, the uniaxial tensile deformation response, the role of deformation texture and microstructural evolution were successfully incorporated into crystal plasticity simulations. Coupling the crystal plasticity with FEA provided a framework that successfully considered hardening and softening mechanisms due to grain rotation during loading, and as a result, accurate prediction of the macroscopic deformation behavior and the associated springback effect was possible [15].

Many of the works coupling crystal plasticity and FEA to predict the macroscopic scale deformation during sheet metal forming operations mainly focused on springback mechanism, texture evolution and material fracture [11]. However, a few studies were also concerned with the thickness distribution in sheet metals or alloys upon sheet forming. For instance, the formability properties were analyzed with an emphasis on thickness distribution of cold-rolled and annealed Al sheet with a thickness of 1 mm upon deep drawing utilizing FEA [16]. Specifically, the role of anisotropy was incorporated into the FE simulations, with the aid of crystal plasticity and it was demonstrated that thickening of the workpiece was observed at the early stages of deformation and it was visible around the edges towards the end of the forming process [16]. Similarly, the earing profile of Al alloy sheets was investigated in forming operation utilizing FEA in conjunction with crystal plasticity algorithm, and demonstrated that the final thickness distribution followed the general plane strain condition [17]. However, all of the aforementioned efforts relied on uniaxial deformation response to define work hardening, and simulations employing a multi-axial hardening rule were not considered.

The current study was undertaken with the motivation of taking the experience and knowledge in this relatively unattended line of research one step further by investigating the thickness reduction in commercial combi PHEs through a combined numerical and experimental approach. Specifically, a multi-scale modeling approach was developed in order to predict the thickness reduction and crack initiation sites on PHE plates upon forming process. A visco-plastic self-consistent (VPSC) crystal plasticity model was employed to determine the appropriate hardening rule for both mating materials by considering the role of microstructure and anisotropy through the incorporation of experimentally measured textures. FE simulations of the metal forming operation were successfully performed, where the roles of both anisotropy and microstructure were taken into account by implementing a multi-axial hardening rule obtained from VPSC simulations into the FE Analysis. The results presented herein demonstrate that reliable predictions of the thickness reduction require appropriate coupling of crystal plasticity and FEA. Thickening was visible around some parts of the edges of the PHE while thickness reduction was more evident around the edges and at the center. The maximum thinning around the edges is due to severe bending deformation [18], however; thinning at the central regions is due to the predominant compressive stresses that are created by severe forming loads exerted by the dies. These regions can be considered as perfect locations for crack initiation leading to damage accumulation, which may result in catastrophic failure of the PHE during forming stage or in service. In order to validate these predicted potential crack initiation sites, the FE thickness distribution results were compared with those of the experimental measurements obtained with a micrometer. The micrometer findings agreed very well with the FE simulation results, which indicates the success of the current multi-scale model utilized to predict the multi-axial hardening rule. Overall, the current approach constitutes an important guideline for the design of new PHEs with reduced manufacturing costs.

2. 2 Experimental Procedure

The PHEs investigated in the current study are initially made of stainless steel plates coupled with their copper (Cu) counterparts stacked together in a sandwich structure. It should be noted that the final PHE consists of only steel plates: Cu acts as a lubricant during metal forming between the die and the steel sheet, and it completely melts during heat treatment at 1150^{o} C for 7-8 hours, and is finally washed away from the PHEs (Figure 2.1).

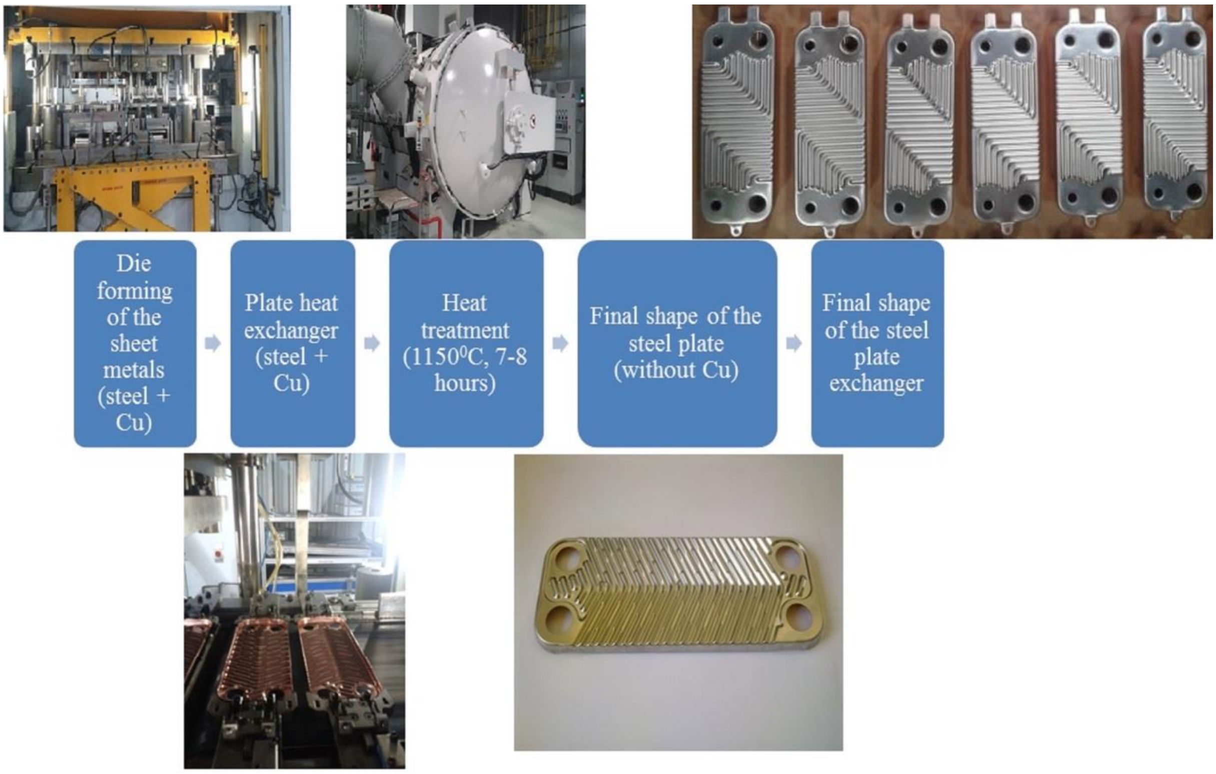

Figure 2. 1 Schematic describing the entire manufacturing process of the steel PHEs [19].

The 316 L stainless steel and Cu were provided by Aperam (France) and BOSCH (Germany), respectively. For the forming of individual sheets, plates were cut as sheets from steel and Cu rolls with dimensions of 195 mm in length, 80 mm in width, and thickness of 0.305 mm. The 316 L stainless steel sheet metal utilized in the study has a chemical composition of 16.3 to 18.7 wt% chromium, 9.90 to 13.15 wt% nickel, 1.90 to 2.60 wt% molybdenum, 2.04 wt% manganese, 0.035 wt% carbon, 1.05 wt% silicium. However, the Cu sheet metal utilized in the study is oxygen – free, has a chemical composition of 99.90 wt% copper and balance phosphate. For forming operation, a hydro servo press with knuckle joint was carried out with a working speed of 28 plates / min (Figure 2.2). The utility of the knuckle joint equipped with the crank shaft brings about an increased press power [20].

The major components of the metal forming operation are male-female dies, blank holder, sheet metals and two pistons that are located at the bottom of the female die. First of all, 14 ton loading was applied with pistons in order to achieve increased contact and reveal initial formed shapes. It should be noted that this step was carried out without blank holder. The second step consisted of application of loads (180 – 250 tons) while the initially formed plates were positioned in the blank holder. This extensive loading is required to prevent springback mechanism while providing sufficient ironing process to the plates. As the blank holder is responsible to break slopes, final shape of the plate heat exchanger was obtained (Figure 2.1). It is noteworthy that no additional processes (milling etc.) were applied to the PHEs after pressing. Final shape of the plate heat exchanger was sliced into three parts in order to simplify the thickness measurements by eliminating the effects of the indented surface. 12 different regions were selected in the steel plate. The thickness reduction with deformation was investigated in these regions with the assistance of a micrometer and a digital caliper. Texture measurements were carried out with Electron Backscatter Diffraction (Acceleration voltage 20 kV, W-Cathode, specimen mounted at 70 degree (tilt)) method and inverse pole figures of both steel and Cu were constructed utilizing the Preferred Orientation Package – Los Alamos (POPLA) software.

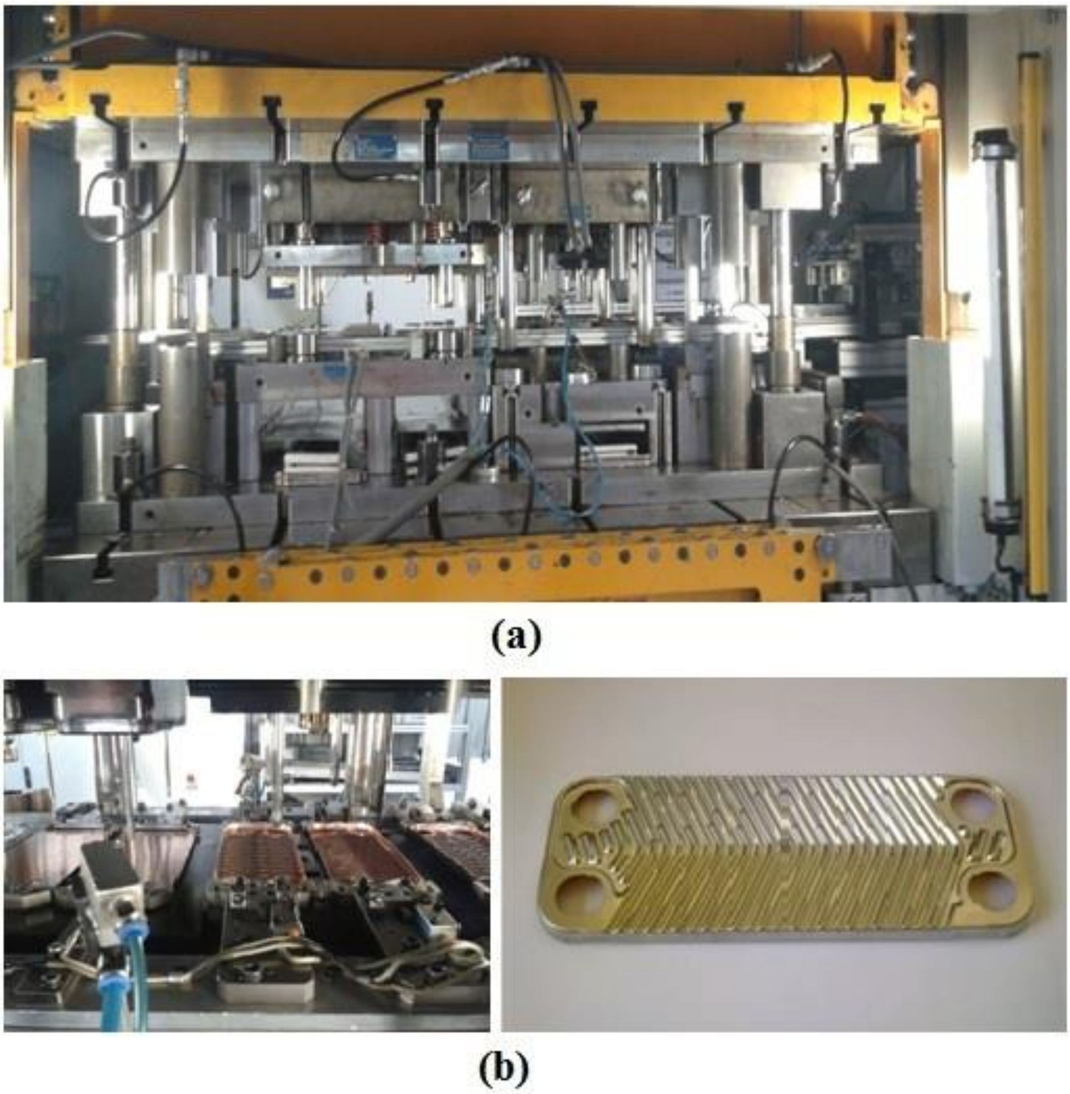

Figure 2. 2 (a) The pressing machine utilized in the metal forming operation. **(b)** Final form of individual steel plates of a PHE upon forming operation [19].

2. 3 Crystal Plasticity Formulation

The VPSC crystal plasticity model was utilized in order to properly incorporate the texture and anisotropy effects into FE simulations. The die forming process investigated in the current work results in multi-axial deformation, such that definition of a flow rule in form of equivalent stress – strain responses of both materials is necessary to properly capture the multi-axial strain hardening during deformation. In the current study, in order to obtain specific flow rules, crystal plasticity modeling was utilized, mainly due to practicality as compared to costly experiments. The major advantage of VPSC crystal plasticity modeling is that it can predict the deformation behavior of the materials at the microscopic scale, i.e. at the slip and twin system levels [21]. Once the VPSC model is established correctly for a material, it can be utilized to predict the deformation behavior of the same initial material under the action of any type of loading [22]. Consequently, prediction of equivalent deformation behaviors of both Cu and steel based on their experimental uniaxial deformation responses becomes possible, which can be considered as more appropriate flow rules to define the strain hardening in FE simulations of the forming process, as discussed before.

With this motivation, the deformation behavior of the steel and Cu sheets were successfully determined with the help of VPSC modeling. For this purpose, initial textures (Figure 2.3) and experimentally determined uniaxial deformation behavior (Figure 2.4) were utilized to model the deformation response at the microscopic level.

The VPSC algorithm utilized in this study accounts for the deformation in the plastic zone. Plastic deformation is observed when one or more slip or twinning systems get activated. For an active slip system (s), the corresponding resolved shear stress (τ_{RSS}^{s}) which dictates plastic deformation is given in the vectorial form of the Schmid tensor (m_i^s) and the applied stress (σ_i) as:

$$\tau_{RSS}^{s} = m_i^s \sigma_i \tag{2.1}$$

The nonlinear shear strain rate in the system s regarding τ_{RSS}^{s} is as follows:

$$\dot{\gamma}^s = \dot{\gamma}_0 \left(\frac{\tau^s_{RSS}}{\tau^s_0} \right)^n = \dot{\gamma}_0 \left(\frac{m^s_i \sigma_i}{\tau^s_0} \right)^n \tag{2.2}$$

where $\dot{\gamma}_0$ refers to reference rate, τ^s_0 defines the threshold stress corresponding to this reference rate, and n represents the inverse of the rate sensitivity index. It should be noted that the superposition of the contributions from all active systems results in the total strain rate in a crystal. This is represented in its pseudolinearized form as shown below [23]:

$$\dot{\varepsilon}_i = \left[\dot{\gamma}_0 \sum_1^s \frac{m^s_i m^s_j}{\tau^s_0} \left(\frac{m^s_k \sigma_k}{\tau^s_0} \right)^{n-1} \right] \sigma_j = M^{c(\text{sec})}_{ij} (\tilde{\sigma}) \sigma_j \tag{2.3}$$

where $M^{c(\text{sec})}_{ij}$ is defined as the secant visco-plastic compliance of the crystal. This term gives the instantaneous relation between strain rate and stress. At the polycrystal level, this relationship is given as [23]:

$$\dot{E}_i = M^{(\text{sec})}_{ij} (\tilde{\Sigma}) \Sigma_j + \dot{\Sigma}^0 \tag{2.4}$$

where $\dot{E}_i$ and Σ correspond to the polycrystal strain rate and applied stress, consecutively.

Including a matrix and inclusions in a continuum, the deviations in strain rate and stress between the inclusion and their overall magnitudes are expressed as:

$$\dot{\tilde{\varepsilon}}_k = \dot{\varepsilon}_k - \dot{E}_k \tag{2.5}$$

$$\tilde{\sigma}_j = \sigma_j - \Sigma_j \tag{2.6}$$

where $\dot{\varepsilon}_k$ and σ_j correspond to the local (single crystal or grain level) strain rate and stress. The stress equilibrium equation can be solved with the help of Eshelby's inhomogeneous inclusion formulation which is as follows [24]:

$$\tilde{\dot{\varepsilon}} = -\tilde{M} : \tilde{\sigma} \tag{2.7}$$

The interaction tensor $\tilde{M}$ is defined as

$$\tilde{M} = n'(I - S)^{-1} : S : M^{(\text{sec})} \tag{2.8}$$

where $M^{(\text{sec})}$ is defined as the secant compliance tensor for the polycrystal aggregate and S refers to the visco-plastic Eshelby tensor [24].

Substitution of equations 2.3 and 2.4 into Equation 2.7 gives the macroscopic secant compliance, $M^{(\text{sec})}$, and the macroscopic strain rate is determined by taking the weighted average of crystal strain rates over all the grains as stated in Equation 2.9:

$$M^{(\text{sec})} = \left\langle M^{c(\text{sec})} : \left(M^{c(\text{sec})} + \tilde{M}\right)^{-1} : \left(M^{(\text{sec})} + \tilde{M}\right)\right\rangle \tag{2.9}$$

When Equations 2.3, 2.7 and 2.9 are iteratively solved, the stress in each grain, the crystal's compliance tensor, and the polycrystal compliance consistent with the applied strain rate $\dot{E}_i$ are obtained. In the study presented herein, the term *n* in Equation 2.2 was selected as 20, which makes the formulation rate insensitive [23]. As for the interaction Equation 2.8, an effective value of $n'=1$ was utilized.

The rate of overall dislocation density can be found as:

$$\dot{\rho} = \sum_n \left\{k_1\sqrt{\rho} - k_2\rho\right\} \left| \, \dot{\gamma}^n \right| \tag{2.10}$$

where k_1 and k_2 represent geometric constants that are associated with the athermal (statistical) storage of the mobile dislocations [24]. The flow stress τ is formulated in the Taylor hardening law as:

$$\tau - \tau_0 = \alpha\mu b\sqrt{\rho} \tag{2.11}$$

where α refers to the dislocation interaction parameter and τ_0 is a reference strength, which defines deformation at the grain level. From Equation 2.11, keeping τ_0 constant, the rate of the flow stress is acquired by taking the time derivative as shown below:

$$\dot{\tau} = \frac{\alpha\mu b\dot{\rho}}{2\sqrt{\rho}} \tag{2.12}$$

The formula obtained by substituting Equation 2.10 into Equation 2.12 is expressed as:

$$\dot{\tau} = \sum_{n} \left\{ k_1 \frac{\alpha \mu b}{2} - k_2 \frac{\alpha \mu b}{2} \sqrt{\rho} \right\} \left| \dot{\gamma}^n \right| \tag{2.13}$$

From Equation 2.11, the following identity is obtained for the purpose of determining square root of the density of dislocations:

$$\sqrt{\rho} = \frac{\tau - \tau_0}{\alpha \mu b} \tag{2.14}$$

Once Equation 2.14 is substituted into Equation 2.13, the rate of flow stress evolution is found as:

$$\dot{\tau} = \sum_{n} \left\{ k_1 \frac{\alpha \mu b}{2} - k_2 \frac{(\tau - \tau_0)}{2} \right\} \left| \dot{\gamma}^n \right| \tag{2.15}$$

It is noteworthy that the term $\left\{ \frac{\alpha \mu b}{2} k_1 - \frac{(\tau - \tau_0)}{2} k_2 \right\}$ in Equation 2.15 represents the linear Voce hardening term (Equation 2.17). Thus, Equation 2.15 can also be written as [24]:

$$\dot{\tau} = \sum_{n} \left\{ \theta_0 \left(\frac{\tau_s - \tau}{\tau_s - \tau_0} \right) \right\} \left| \dot{\gamma}^n \right| \tag{2.16}$$

where θ_0 is the constant strain hardening rate, and τ_s is the saturation stress in the absence of geometric effects, or the threshold stress. The hardening is characterized by a well - known extended Voce law [24] which is defined by the evolution of the threshold stress (τ^s) considering accumulated shear strain (Γ) in each grain of the form:

$$\tau^s = \tau_0 + (\tau_1 + \theta_1 \Gamma) \left(1 - \exp\left(-\frac{\theta_0 \Gamma}{\tau_1} \right) \right) \tag{2.17}$$

where τ_0 represents the reference strength, and τ_1, θ_0 and θ_1 are the Voce hardening parameters [24]. The hardening law defined by Equation 2.17 refers to the onset of plasticity and the saturation of threshold stress at larger strains.

The initial textures of both steel and Cu (Figure 2.3) were incorporated into the VPSC model described by Equations (2.1) - (2.17) to predict the macroscopic deformation response of each material under uniaxial tensile loading (Figure 2.4). The true stress - true inelastic strain data were plotted in order to compare the simulations and experiments. One should note that only plastic deformation regime is modeled in the VPSC simulations. For steel and Cu, 0.5 % and 0.2 % plastic strain spans were considered in the modeling efforts, respectively. These plastic strain spans were selected as failure occurs beyond these values. The current simulation results stand in good agreement with the experimental findings. It should be noted that the initial stress levels are not consistent with those of the experimental curves.

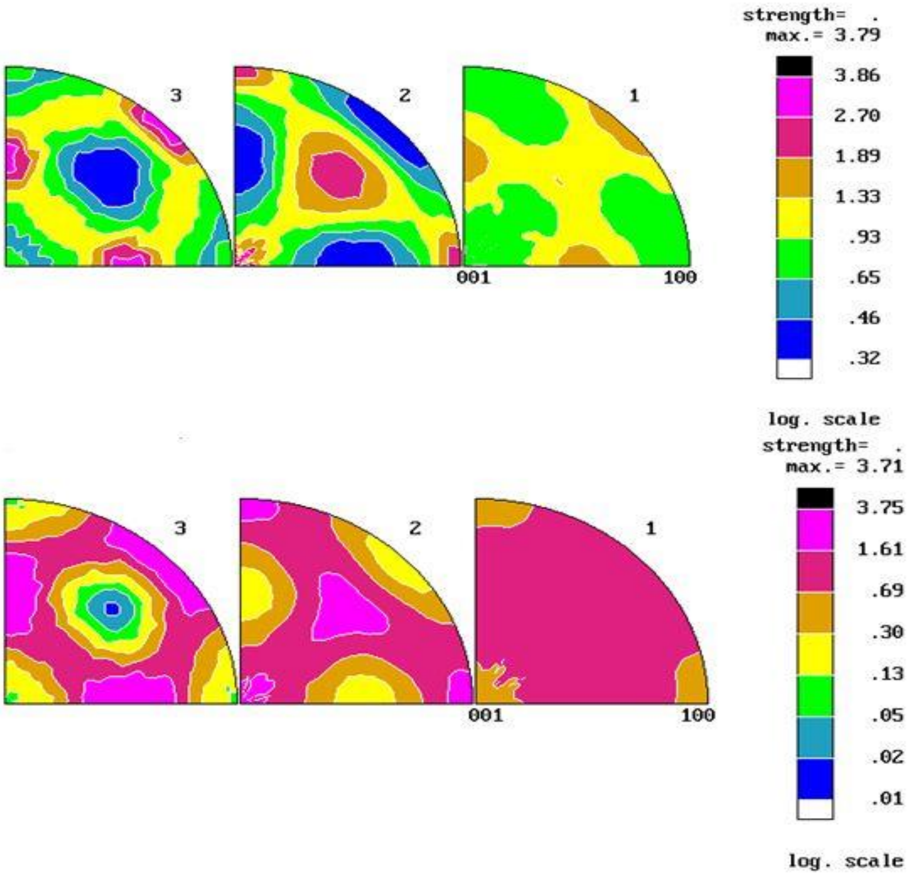

Figure 2. 3 Initial texture of Cu (upper image) and steel (lower image). Inverse pole figures 1, 2, and 3 correspond to normal, transverse, and extrusion directions, respectively [19].

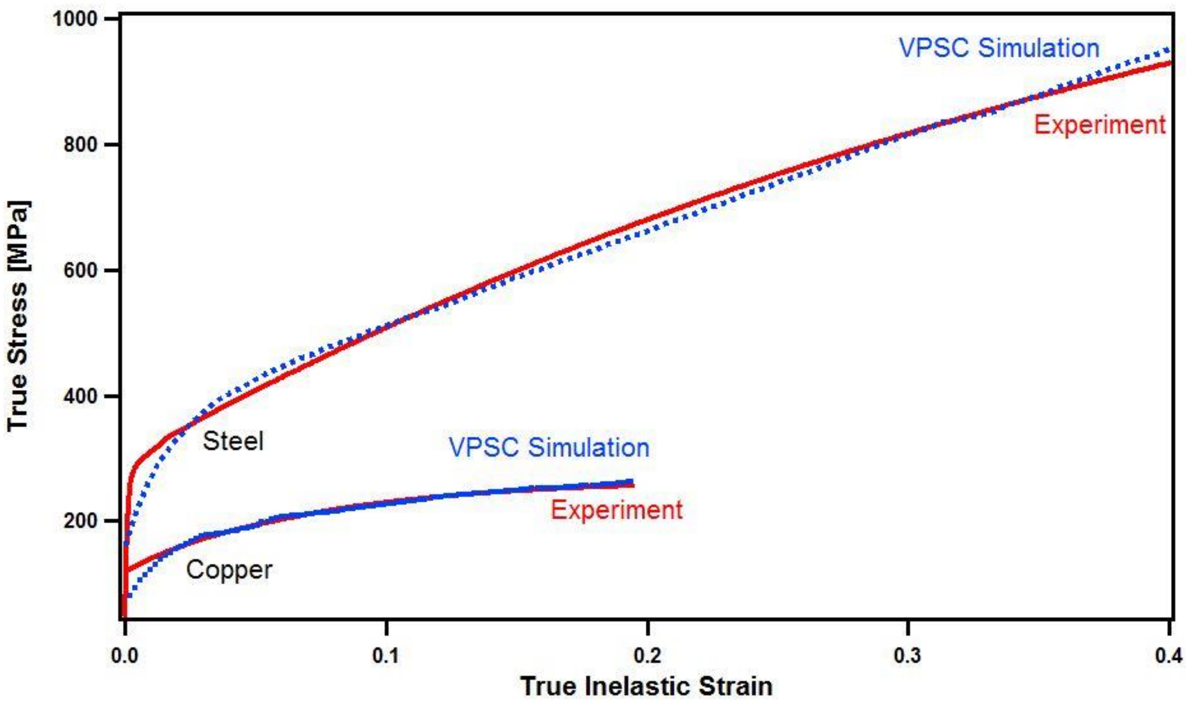

Figure 2. 4 The experimentally observed and predicted uniaxial tensile deformation responses of steel and Cu [19].

2.4 Incorporation of Crystal Plasticity into Finite Element Simulations

Application of very large forces within a very short time period results in a significant amount of deformation leading to considerable difficulties in FE simulations of sheet metal forming, such as unstability in sheet metal flow, stretching and compressing, springback, and plane strain condition. For instance, it was noted that forming operation gives way to material non – linearities arising from dynamic friction, dynamic boundary conditions and complicated contact condition between the die and the sheet metals [25]. This induces turbulent stability and converge problems in the FE simulations [25, 26].

In order to overcome such difficulties, in the current work, FE simulations of the forming operation were performed using ANSYS 15.0 commercial software, where the AUTODYN solver as a part of an explicit dynamics system was utilized in the simulations in terms of the nonlinear dynamic analysis. For the purpose of representing the non – linearity, Lagrangian formulation was adopted. The plastic flow was described by the multi-linear isotropic hardening. A fine mesh was constructed with 100350 nodes and 327303 quadrilateral elements. The meshing of the geometry of the sheet metals was set to

“MultiZone”. In this meshing type, geometry is decomposed into a hex mesh leading to a significant increase in the accuracy and efficiency of the simulations. The orthogonal quality of the mesh was computed as 0.99 out of 1.0. As for the boundary conditions, remote displacements were applied to the bodies of male and female dies and on the bottom blank holder surface. The forming loads were imposed on the top surface of the male die and the bottom surface of the female die. It is noted that all dimensions and constraints were described in the Cartesian coordinate system.

For the purpose of determining an appropriate flow rule for the FE simulations of the metal forming, the VPSC model described in the preceding section was performed in order to predict the equivalent deformation behavior of Cu and steel materials regarding the uniaxial deformation behavior. The prediction of the uniaxial data (Figure 2.4) evidences the successful modeling of the microstructural deformation. Hence, same VPSC model was used in order to determine the equivalent deformation behaviors of both materials in the plastic deformation zone with the help of the hardening parameters. Furthermore, the heterogeneous stress – strain distribution in the sheet metals indicates the need for determining the appropriate flow rule which is based on the equivalent deformation behavior. In order to define the deformation characteristics of the polycrystalline aggregates in the VPSC, determination of the velocity gradient tensor is necessary. Specifically, the ratio of normal and shear stresses in different regions of the plates was obtained from FE forming simulations that utilized the uniaxial tensile deformation response of both steel and Cu as hardening rules. One should note that the velocity gradient tensors of steel and Cu differ due to the material-independent stress distributions obtained in the forming simulations (Fig. 2.5). The first term of symmetric velocity gradient tensor is the ratio of normal and shear stress (2.06 for steel, 1.25 for Cu) and the normalized second term is 1.0. The summation of diagonal components of the corresponding tensor was chosen as zero for crystal plasticity simulations. The division of the first term by two diagonally is to elicit homogeneous deformation [27, 28]. Consequently, the velocity gradient tensors for both materials were calculated as:

$$\dot{U}_{Steel} = \begin{bmatrix} 2.06 & 1.0 & 0 \\ 1.0 & -1.03 & 0 \\ 0 & 0 & -1.03 \end{bmatrix} \quad , \quad \dot{U}_{Copper} = \begin{bmatrix} 1.25 & 1.0 & 0 \\ 1.0 & -0.625 & 0 \\ 0 & 0 & -0.625 \end{bmatrix}$$

The VPSC simulation results regarding the equivalent stress – strain responses for both materials are represented in Figure 2.6. The results stand in good agreement with respect to each other as steel exhibits higher strength than Cu. It is noteworthy that relatively large strains were taken into account in order to determine the equivalent deformation behavior (Fig. 2.6) while the strain values were smaller in the simulations regarding the experimental uniaxial stress – strain state. Particularly, the onset of necking and damage limit the required strain values in order to model the experimental uniaxial deformation behavior. Therefore, only plastic strains were taken into account in the VPSC simulations. Hence, the corresponding flow rules for both materials were determined for relatively large strains regarding the equivalent stress – strain state (Figure 2.6).

Table 2.1 Voce hardening parameters utilized in the VPSC simulations.

Material	τ_0 [MPa]	τ_1 [MPa]	θ_0 [MPa]	θ_1 [MPa]
Steel	97.2	137	2750	234
Copper	41.2	71	1470	96

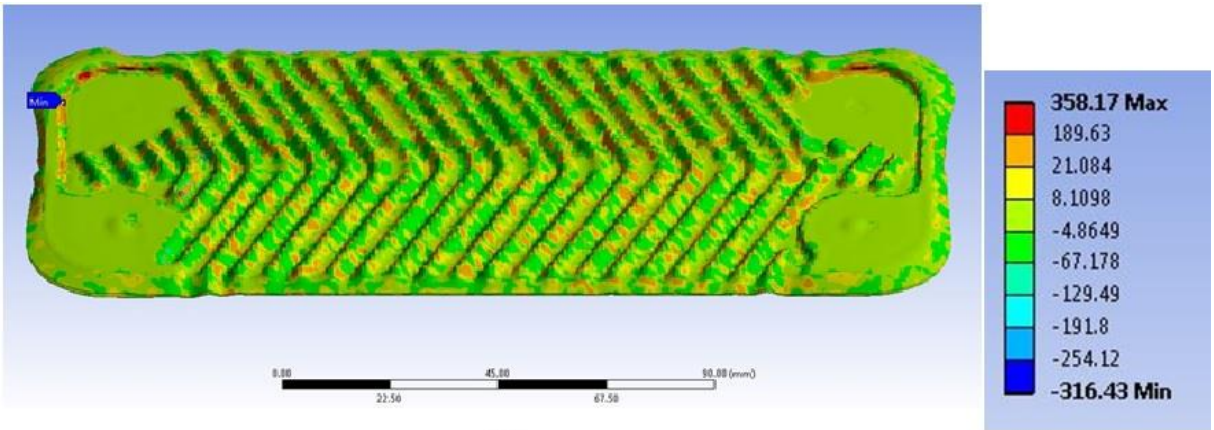

(a)

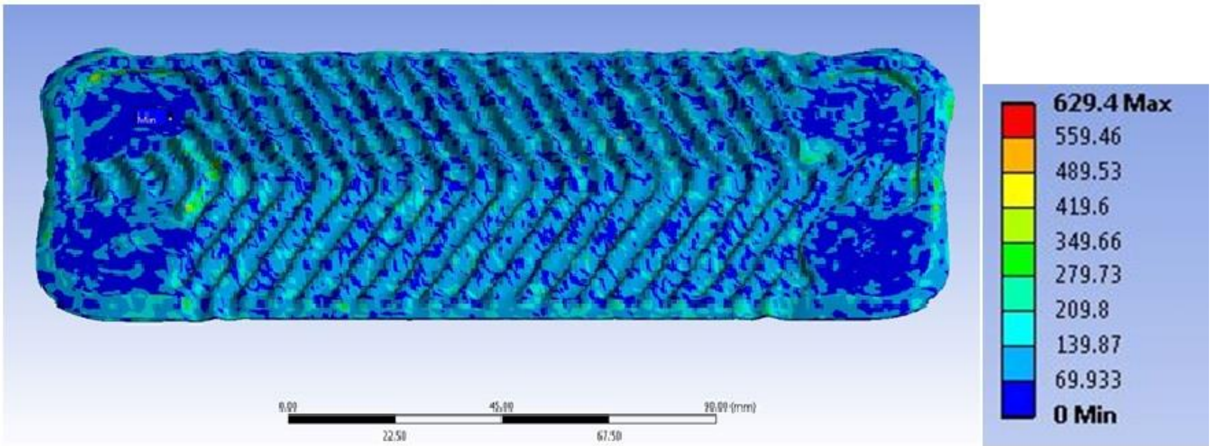

(b)

Figure 2. 5 (a) Heteregeneous normal stress distribution on steel plate**. (b)** Heteregeneous equivalent stress distribution on steel plate [19].

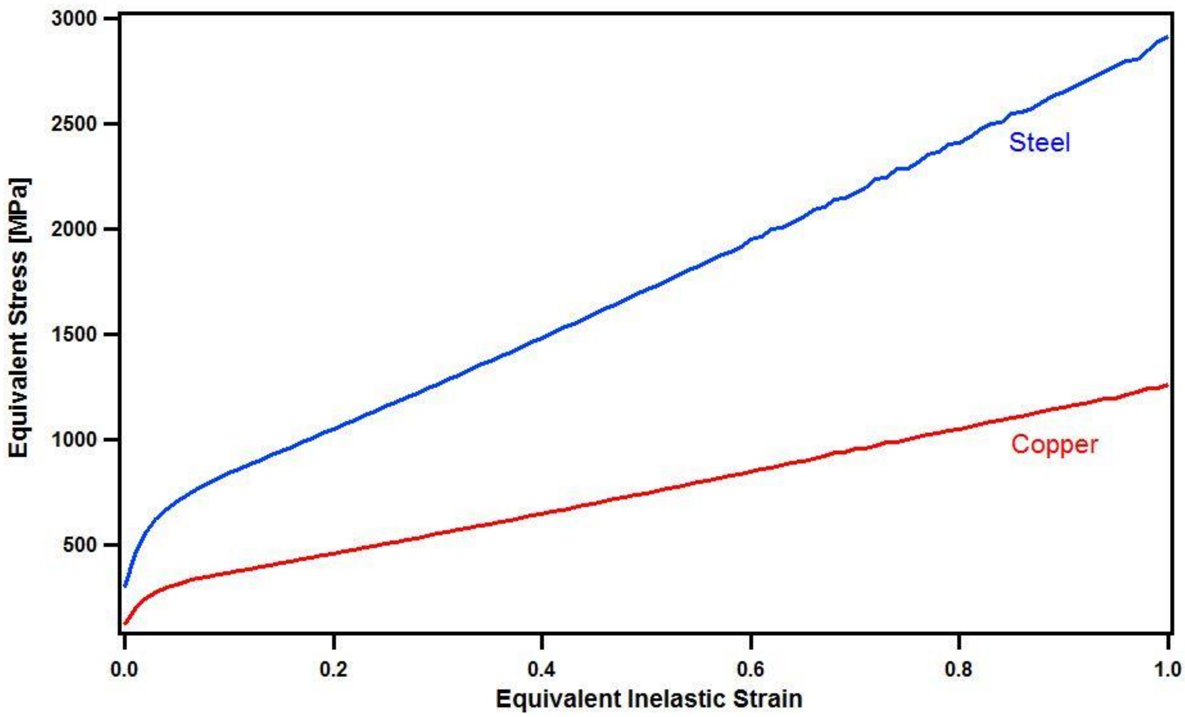

Figure 2. 6 Predicted equivalent stress – equivalent strain responses of steel and Cu representing multi-axial stress state [19].

2.5 Simulation Results and Discussion

The current multi-scale modeling approach has demonstrated that the appropriate treatment of microstructure plays a key role in order to predict the thickness distribution in metal forming operation precisely. In particular, the FE forming simulation results have demonstrated that incorporating the material flow rule at the microstructure level into the macroscopic deformation (FE) model brings about accurate predictions (Table 2.2), which emphasizes the fact that incorporation of a multi-axial deformation state is necessary for the sake of realistic simulations in the case of forming operations featuring combined loading. In particular, the stress - strain distribution under the action of forming loads was observed to be significantly heterogeneous in the current work (Figure 2.5), and multi-axial treatment of the hardening behavior utilizing a flow rule based on an equivalent stress – strain response turned out to be necessary for successful predictions [27,28]. For this purpose, VPSC was utilized in the current work to predict the equivalent stress – states of both steel and Cu based on their uniaxial stress – strain responses and initial textures. In particular, the power of VPSC to predict the equivalent deformation response of both steel and Cu gave way to consider microstructural differences between the two materials in forming simulations. The VPSC model employed in the current work utilizes the experimentally measured texture to determine each grain's crystallographic orientation. By this way, stress – strain states applied onto steel and Cu polycrystalline materials can be transferred onto all grains [21, 23]. On the other hand, a closer look at the initial texture of two materials indicates that the difference is not considerable before deformation (Figure 2.3). It is also noted that materials have different strength values based on characteristics of their microstructures as observed in the equivalent deformation responses (Fig. 2.6).

Another important discussion point arises from deformation and thickness distribution of PHEs during forming: it is obvious that steel plate takes exact shape of dies upon 250 ton loading and permenant shape change due to severe plastic deformation is clearly observed (Fig. 2.7.a and Fig. 2.7.b). It is apparent that strength levels increase significantly after forming process due to plastic deformation as a result of strain hardening mechanism [29]. It should be kept in mind that holes on the surface are responsible for hot/cold fluid flow and are created after forming process. In the FE simulations, 12 different regions were selected in the deformed steel plate in order to investigate thickness reduction as this phenomenon is a significant criterion for the design process of sheet metals. It is evident that thickness varies throughout the PHE ranging from 0.29 mm to 0.32 mm (Table 2.2) as the undeformed sheet steel has a homogeneous thickness of 0.3 mm. Despite the fact that the utilized die has a regularly and homogeneously distributed pattern, the thickness distribution does not follow a regular pattern. This is the consequence of severe plastic deformation causing unexpected stress-strain localizations, which may indeed give way to crack initiation sites. This has been demonstrated before [30] such that unevenly distributed thickness distribution in the workpiece may cause localized stress concentration leading to considerable damage accumulation. As more thickness reduction increases the number of crack nucleation sites, the critical regions are those marked by numbers 3, 8, 10 and 12 in Fig. 2.7. a and Fig. 2.7.b. The edges of the steel plate (marked by 3, 8, 10) undergo maximum thinning. This is due to the bending which is a predominant deformation mechanism in these regions. This mechanism is known to be strongly associated with thinning phenomenon [18]. Furthermore, undesired distortions and asymmetries observed in the FE simulations (Fig. 2.7.b) are also perfect crack locations.

A comparison of the current findings with its previous counterpart demonstrates that current results align very well with the literature. For instance, thickening is concentrated around some parts of the edges of the workpiece (no.1 and no.11 in Fig. 2.7.a) as in the case of cold rolled and annealed Al sheets [16]. Furthermore, thickness reduction at the center of the plate is more apparent (no. 8 in Fig. 2.7.a) which corresponds well with previous studies on Al sheets [9]. In terms of crack formation, failure is likely to occur at the regions a little far away from the center in the case of steel sheets having complex phase [31]. Considering the current methodology, the combined experimental – computational approach has been utilized previously by the authors [27, 28], the obtained results have been highly promising.

The current study demonstrated that incorporation of microstructural effects and anisotropy of steel and Cu provided reliable predictions of thickness reduction prediction in PHEs utilizing multi-scale modeling approach. Specifically, the multi-scale modeling effort presented herein consisted of two steps: (i) crystal plasticity simulations, where flow rule of both materials was predicted based on their experimentally determined uniaxial deformation response; and (ii) FE modeling, where die forming operation was simulated utilizing the material hardening rule obtained from crystal plasticity simulations. The current approach successfully predicted both the final thickness distribution and the potential crack initiation sites on the steel plate. Furthermore, the numerically predicted results stood in good agreement with the experimental results.

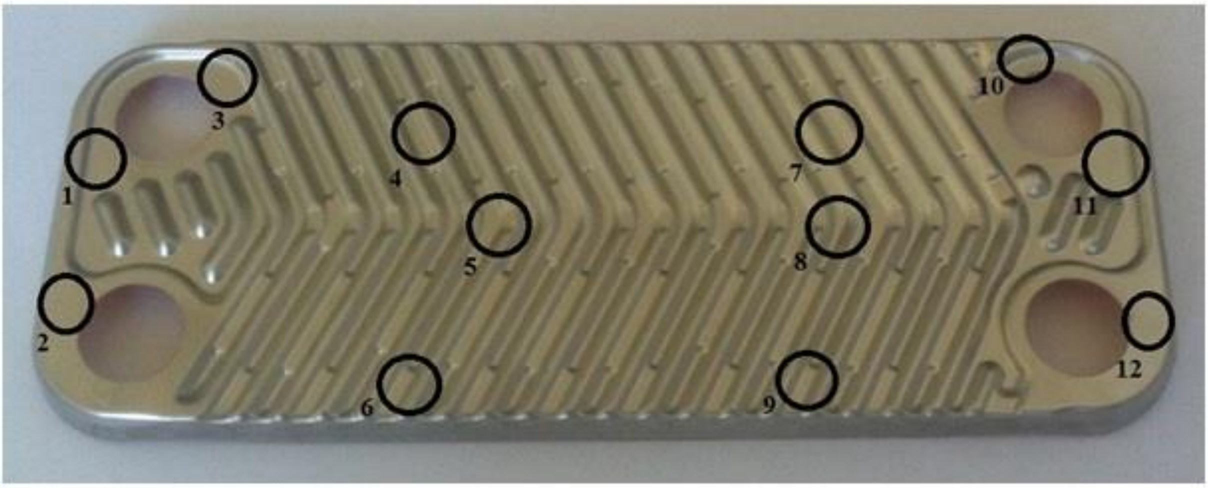

(a)

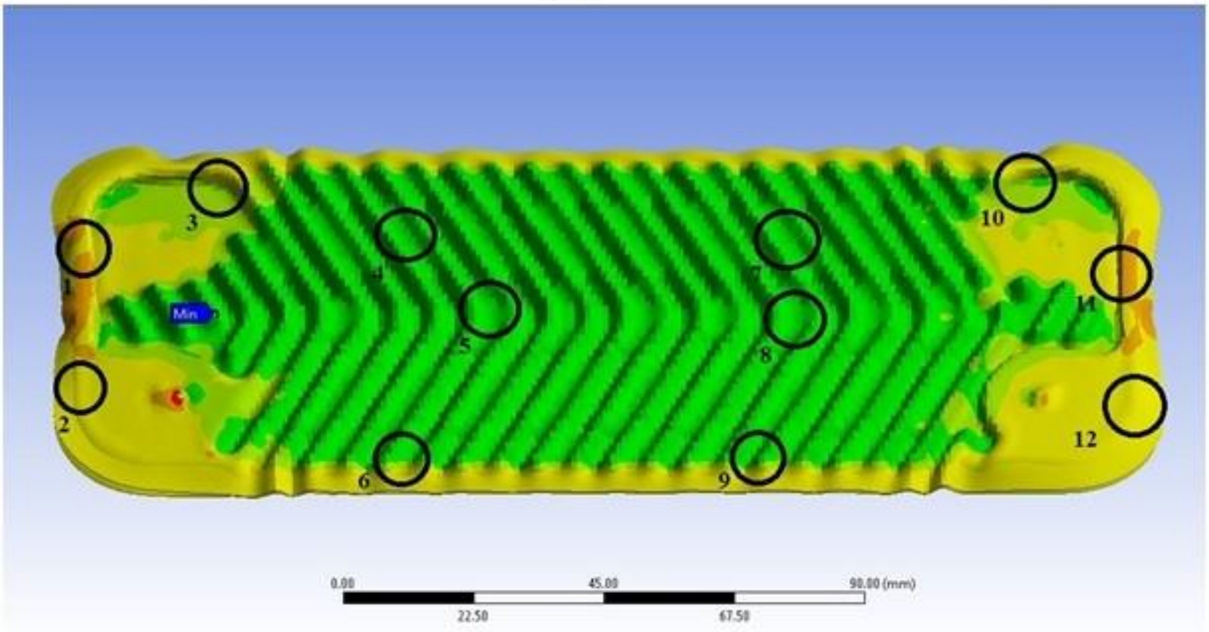

(b)

Figure 2. 7 (a) Experimentally determined thickness distribution within a single steel plate. **(b)** Computationally predicted thickness distribution within a single steel plate. The measured and predicted thicknesses of the zones indicated with cirles are tabulated in Table 2.2 [19].

Table 2.2 A comparison between the experimental and simulation results in terms of thickness distribution. The numbers correspond to the encircled zones in Figure 2.7 [19](Accuracy = +/- 0.002 mm).

No	Experimentally Measured Thickness (mm)	Simulated Thickness (mm)
1	0.322	0.320-0.310
2	0.301	0.310-0.300
3	0.292	0.300-0.290
4	0.304	0.300-0.290
5	0.323	0.300-0.290
6	0.309	0.300-0.290
7	0.304	0.300-0.290
8	0.287	0.300-0.290
9	0.301	0.300-0.290
10	0.286	0.310-0.300
11	0.313	0.320-0.310
12	0.288	0.310-0.300

2.6 Conclusions

In the current study, a multi-scale modeling approach was presented that incorporates strain hardening and anisotropy into the macroscopic scale finite element (FE) simulations with the aid of crystal plasticity while simulating an industrial die forming operations in order to predict thickness distribution in plate heat exchangers (PHEs) utilized in combi boilers. The effects of microstructure and anisotropy upon forming loads were taken into consideration by implementing an appropriate multi-axial material hardening rule acquired from crystal plasticity simulations into the FE analysis. In particular, the equivalent deformation responses of steel and Cu were obtained from crystal plasticity simulations based on experimentally determined uniaxial stress – strain states and initial textures. The corresponding equivalent stress – strain behaviors were adopted as material flow rules for defining the strain hardening of both steel and Cu throughout the FE forming simulations. The results presented herein elucidate the success of the current multi-scale modeling approach in predicting the deformation and thickness reduction during the die forming of steel and Cu sheets. Furthermore, the current findings also evidence that failure of PHEs can be prevented during forming process by determining the crack initiation sites, based on the thickness reduction predictions since the simulated thickness distribution results stand in good agreement with those of the experimentally measured ones. Overall, the current findings constitute a step forward and an important guideline for the design of new PHEs with improved service performance and lower cost.

This knowledge gained in this study was further extended to the crack initiation analysis of two rail steels (bainitic and pearlitic rail steels) under rolling contact loading, where fatigue performances of these steels were investigated with the help of Jiang-Sehitoglu plasticity model.

2.7 References

[1] T. Altan, V.Vazquez, Numerical process simulation for tool and process design in bulk metal forming, CIRP Annals – Manufacturing Technology 45 (1996) 599

[2] J. Gronostajski, A.Matuszak, A.Niechaiowicz, Z.Zimniak, The system for sheet metal forming design for complex parts, Journal of Materials Processing Technology 157 (2004) 502

[3] Z.Zimniak, Problems of multi – step forming sheet metal process design, Journal of Materials Processing Technology 106 (2000) 152

[4] A. Makinouchi, Sheet metal forming simulation in industry, Journal of Materials Processing Technology 60 (1996) 19

[5] S.K. Panthi, N. Ramakrishnan, K.K. Pathak, J.S. Chouhan, An analysis of springback in sheet metal bending using finite element method (FEM), Journal of Materials Processing Technology 186 (2007) 120

[6] S. Thibaud, R.B. Hmida, F. Richard, P. Malecot, A fully parametric toolbox for the simulation of single point incremental sheet forming process: Numerical feasibility and experimental validation, Simulation Modeling Practice and Theory 29 (2012) 32

[7] J. Reagan, E. Smith, Metal Spinning, Bruce Publishing, New York, 1993

[8] Shanmuganatan S.P., Senthil Kumar V.S., Experimental investigation and finite element modeling on profile forming of conical component using Al 3003(O) alloy, Materials and Design 36 (2012) 564

[9] V.S. Senthil Kumar, D.Viswanathan, S. Natarajan, Theoretical prediction and FEM analysis of superplastic forming of AA7475 aluminum alloy in a hemispherical die, Journal of Materials Processing Technology 173 (2006) 247

[10] M. Firat, B. Kaftanoglu, O. Eser, Sheet metal forming analyses with an emphasis on the springback deformation, Journal of Materials Processing Technology 196 (2008) 135

[11] F. Roters, P. Eisenlohr, L. Hantcherli, D.D. Tjahjanto, T.R. Bieler, D. Raabe, Overview of constitutive laws, kinematics, homogenization and multiscale methods in crystal plasticity finite-element modeling: Theory, experiments, applications, Acta Materialia 58 (2010) 1152

[12] K. Inal, R.K. Mishra, O. Cazacu, Forming simulation of aluminum sheets using an anisotropic yield function coupled with crystal plasticity theory, International Journal of Solids and Structures 47 (2010) 2223

[13] J. Lian, F. Barlat, B. Baudelet, Plastic behaviour and stretchability of sheet metals II. Effect of yield surface shape on sheet forming limit, International Journal of Plasticity 5 (1989) 131

[14] R.J. Asaro, A. Needleman, Texture development and strain hardening in rate dependent polycrystals, Acta Metallurgica 33 (1985) 923.

[15] R.K. Verma, P. Biswas, T. Kuwabara, K. Chung, Two stage deformation modeling for DP 780 steel sheet using crystal plasticity, Materials Science and Engineering A 604 (2014) 98

[16] J. Hu, J.J. Jonas, T. Ishikawa, FEM simulation of the forming of textured aluminum sheets, Materials Science and Engineering A 256 (1998) 51

[17] I. Tikhovskiy, D. Raabe, F. Roters, Simulation of earing during deep drawing of an Al – 3% Mg alloy (AA5754) using a texture component crystal plasticity FEM, Journal of Materials Processing Technology 183 (2007) 169

[18] B. Longue, M. Dingle, J.L. Duncan, Side-wall thickness in draw die forming, Journal of Materials Processing Technology 182 (2007) 191

[19] O.Onal, B. Bal, D. Canadinc, E. Akdari, Experimental and numerical evaluation of thickness reduction in steel plate heat exchangers, Submitted to Journal of Materials Processing Technology

[20] K. Osakada, K. Mori, T. Altan, P. Groche, Mechanical servo press technology for metal forming, CIRP Annals - Manufacturing Technology 60 (2011) 651

[21] D. Canadinc, E. Biyikli, T. Niendorf, H.J. Maier, Experimental and numerical investigation of the role of grain boundary misorientation angle on the dislocation–grain boundary interactions, Advanced Engineering Materials 13 (2011) 281

[22] D. Canadinc, H. Sehitoglu, H.J. Maier, P. Kurath, On the incorporation of length scales associated with pearlitic and bainitic microstructures into a visco-plastic self-consistent model, Materials Science and Engineering A 485 (2008) 258

[23] R.A. Lebensohn, C.N. Tomé, A self-consistent anisotropic approach for the simulation of plastic deformation and texture development of polycrystals: Application to zirconium alloys, Acta Metallurgica et Materialia 41 (1993) 2611

[24] U.F. Kocks, C.N. Tomé, H.R. Wenk, Texture and anisotropy, Cambridge University Press, New York, 1998

[25] H. Liu, J.L. Yuan, J. Jin, Visualization simulations for a cold press die, Journal of Materials Processing Technology 129 (2002) 321

[26] Z.Q. Feng, C. Vallee, D. Fortune, F. Peyraut, The 3e hyperelastic model applied to the modeling of 3D impact problems, Finite Elements in Analysis and Design 43 (2006) 51

[27] O. Onal, B. Bal, S.M. Toker, M. Mirzajanzadeh, D. Canadinc, H.J. Maier, Microstructure-based modeling of the impact response of a biomedical niobium–zirconium alloy, Journal of Materials Research 29 (2014) 1123

[28] O. Onal, C. Ozmenci, D. Canadinc, Multi-scale modeling of the impact response of a strain-rate sensitive high-manganese austenitic steel, Frontiers in Materials 1 (2014) 16

[29] J. LI, C. LI, T. Zhou, Thickness distribution and mechanical property of sheet metal incremental forming based on numerical simulation, Transactions of Nonferrous Metals Society of China 22 (2012) 54

[30] R. Padmanabhan, M.C. Oliveira, J.L. Alves, L.F. Menezes, Influence of process parameters on the deep drawing of stainless steel, Finite Elements in Analysis and Design 43 (2007) 1062

[31] C.L. Xie, E. Nakamachi, Investigations of the formability of BCC steel sheets by using crystalline plasticity finite element analysis, Materials and Design 23 (2002) 59

CHAPTER 3: ROLLING CONTACT FATIGUE OF RAIL STEELS

3.1 Introduction

The railroad industry seeks new materials to make improvements in the infrastructure of the rail production. This is also needed in order to reduce costs thus increase the railroad transportation efficiency. The concerns are related to the rail itself and materials that are used in rail manufacture [1]. Prolonging rail life is possible with increasing the fatigue and wear resistance. Steels are commonly used rail materials with higher hardness which gives way to higher wear resistance. Since wear significantly helps to increase crack initiation sites in the material as better wear resistance reduces the (potential) crack formation.

Crack initiation on the rail surface plays a commanding role in catastrophic failure. Specifically, cracks initiate and branches into the entire rail thus leading to failure under fatigue loading. Additionally, the rail material is subjected to the accumulated strains due to the action of cyclic loads. This is also a major contribution to the crack formation which is entitled as ratchetting.

Reducing maintenance costs and eliminating catastrophic failure become more difficult as the loads and traffic on the rails have significantly increased [2]. Therefore, this problem is complex in terms of engineering as it includes many parameters regarding the fatigue life of the rail. These are listed as the magnitudes of normal and shear forces, the rail itself, the strain rates, stresses that occur within the rail material, resistance to wear as well as environmental factors (i.e corrosion). The service life of the rail is governed by these parameters under rolling contact fatigue (RCF). This loading gives way to crack initiation, leads to crack propagation under repeated cycles thus catastrophic failure at the end [1, 2]. The crack initiation in rail materials - particularly steels - has been the focus of many studies in the recent years. The accurate prediction of crack formation is significant in terms of enhancing rail design and extending service life. Accordingly, the study presented herein focuses on crack initiation modeling of the specific rail steels.

Cyclic rolling loading brings about a complicated stress state in the material leading to fatigue and ratcheting damage. Many engineering and research based models have come along in order to predict the service life under RCF [3-13]. In engineering models, some aspects of the stress states i.e residual stresses/strains are not considered [3]. The engineering models have exhibited good approaches to the problems and have been the subject of many studies [4-9]. The Lundberg – Palmgren (LP) was the first engineering model to predict RCF and it anticipates the crack initiation sites below the material surfaces [9]. The maximum orthogonal shear stress, which is the major element of the shear stress helps to initiate cracks in the material [9]. The disadvantages of the LP model are that only normal forces were taken into account and the locations of the cracks were determined imprecisely [14].

In order to overcome the drawbacks of the LP model, the Ioannides – SKF model was introduced [7]. The fatigue limit parameter was redefined as a threshold and recalculated in the Ioannides – SKF model [4]. This modification significantly helps to improve the crack initiation predictions of the LP model [14]. However, the traction coefficient (traction force to weight ratio) as well as direction were absent in the Ioannides – SKF model [4]. Tallian proposed a statistical model in which traction coefficient and some material properties (i.e fatigue limiting stress, surface defect distribution) were incorporated [4, 5]. The depth – dependent orthogonal shear stress field was used in this model and Paris Law was taken into account [14]. The Tallian model is superior to Ioannides – SKF and LP model but it has notable drawbacks. These are the absence of crack initiation prediction [14], inaccurate prediction of crack growth mechanism, and incapability of predicting the defect distribution. The inaccurate prediction of the defect distribution gives way to shortfalls in crack size estimation with the increasing deformation [15]. Kudish and Burris developed a model in order to predict crack initiation up to catastrophic failure. They addressed the drawbacks of Tallian's model [15] and made improvements by incorporating friction coefficient, fracture toughness and initial crack location to the Paris Law [14, 15].

Apart from engineering models, research – based counterparts consist of details of the stress state i.e strain amplitudes under rolling contact [3, 14]. One of the distinguishing features of the research based models is that they are utilized with the material fracture models. In addition to this, the limitations of the research based models for RCF predictions are given as considerable computational costs and inconsistent simulation results when large loads are in action [3]. The Merwin – Johnson and Hearle – Johnson developed semi analytical models incorporating the deformation behaviors of the materials into the fatigue predictions [10, 11]. These analytical models are able to predict the non - linear plastic deformation behavior under repeated contact cycles as finite element methods are time consuming. The Merwin – Johnson model made an assumption that elastic strain fields are utilized to find the total strains in the material with the help of kinematic strain levels [11].

The superiority of the model is that it can predict the residual stress accumulation below the material surface. Additionally, the surface displacement in the motion direction as well as the resistance to rolling deformation was predicted. The Hearle and Johnson proposed a model in that the plastic zones were determined regarding the dislocation motions in order to predict the plastic flow under rolling contact. The dislocation interactions at the specific locations of these plastic zones were investigated. The cost in terms of computational times reduced due to a major drop – off in the simulation steps as this investigation was carried out at a steady state. The Hearle - Johnson model is advantageous over Merwin – Johnson, this is evidenced by the fact that the cyclic response and strains are not considered in the Merwin – Johnson model. This means that Merwin – Johnson model is inaccurate to predict flow in the rolling direction [10].

Jiang and Sehitoglu developed a model in order to overcome the drawbacks of the engineering and research based models. This model consists of multiaxial fatigue damage parameter that is associated with the normal and shear stresses [3, 12]. The Jiang – Sehitoglu model has many advantages such as consideration of ratcheting damage and rate, non proportional loading and non – linear kinematic hardening rule for crack initiation modeling [3, 16]. The non – linear kinematic hardening rule which is dependent on the Armstrong – Frederick law is significant in terms of ratcheting damage in that the backstress tensor is decoupled into many parts [16].

Jiang and Sehitoglu [12] previously focused on the residual stresses and ratcheting regarding the shear strain. These are dependent on a procedure called stress – strain relaxation and a stress invariant assumption. The stress invariant assumption includes the introduction of non – zero residual stresses/strains with increasing number of cycles. Particularly, the first value of the stress for each number of cycles is considered as the stress value arising from the previous cycle. This corresponds well with the Finite Element simulations. The damage parameters were found following many fatigue experiments. The fatigue damage parameter includes the normal and shear stresses acting on the critical plane. The Jiang – Sehitoglu model considerably enhanced the predictions of the ratchetting rate decay and shear strain accumulation under rolling contact loading as compared to the previous models [13, 17, 18].

In the work presented herein, the stress states of the two rail steels (the head hardened pearlitic and the J6 bainitic steel) under rolling contact loading were investigated with the

Jiang – Sehitoglu (JS) plasticity model [3, 12, 13]. The JS fatigue model successfully computed the ratchetting and fatigue damage with the help of deformation history as well as number of fatigue cycles to crack initiation. The experimental results show that the bainitic steel has higher yield strength than the pearlitic counterpart meaning that it withstands higher loads at low shear tractions as strength is significant. As the shear forces ascend, the ductility plays a key role and the bainitic steel becomes less ductile than the pearlitic steel does. This indicates that the performances of these steels become similar at high shear forces. One of the considerable result shows that when the ratio of normal/tangential loads is in the range of 0.2 – 0.5, the crack initiation does not lead to the failure. Another important finding is that the crack initiation is dictated by the fatigue damage at low shear forces whereas it is controlled by the ratchetting damage as the shear forces ascend. Consequently, the obtained results give way to the usage of the pearlitic and bainitic steels in railheads but the fatigue crack initiation phenomenon under rolling contact condition remains a major concern.

3.2 Approach

A plasticity model was used to compute the ratchetting strain for each cycle to predict the crack initiation. The fatigue life was determined depending on the deformation behavior by the multiaxial fatigue damage model. These two models are presented in detail in the following section.

3.2.1 Plasticity Model

Jiang and Sehitoglu (JS) [12] proposed a plasticity model based on kinematic hardening which is capable of predicting the accumulated ratchetting throughout the proportional and non – proportional loading [12] (Figure 3.1).

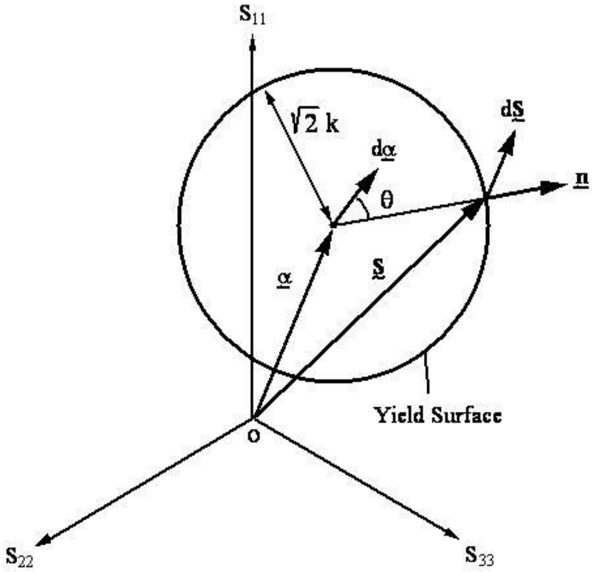

Figure 3. 1 The yield surface representation and stress associated tensors in the JS model [19].

The JS model is based on the Von Mises yield criteria which is as follows:

$$f = \left(\underline{\underline{S}} - \underline{\underline{\alpha}}\right) : \left(\underline{\underline{S}} - \underline{\underline{\alpha}}\right) - 2k^2 = 0 \tag{3.1}$$

where S represents the stress tensor in the deviatoric stress state, α denotes the deviatoric backstress which is the centre of the yield surface, k stands for shear yield strength. The plastic strain increment tensor is shown below:

$$d\underline{\underline{\varepsilon}}^p = \frac{1}{h} \langle d\underline{\underline{S}} : \underline{\underline{n}} \rangle \underline{\underline{n}} \tag{3.2}$$

where h represents the plastic modulus, n denotes the unit normal to the yield surface, < > stands for MacCauley operation as this gives only positive and is mathematically as follows:

$$\langle x \rangle = \frac{x + |x|}{2} \tag{3.3}$$

where x is defined as a constant. The backstress is described below:

$$\underline{\underline{\alpha}} = \sum_{i=1}^{M} \underline{\underline{\alpha}}^{(i)} \tag{3.4}$$

The kinematic hardening rule that is utilized in the JS plasticity model is as follows:

$$d\underline{\underline{\alpha}}^{(i)} = c^{(i)} r^{(i)} \left[\underline{\underline{n}} - \left(\frac{\left| \underline{\underline{\alpha}}^{(i)} \right|}{r^{(i)}} \right)^{\chi^{(i)}+1} \underline{\underline{L}}^{(i)} \right] \sqrt{d\underline{\underline{\varepsilon}}^{p} : d\underline{\underline{\varepsilon}}^{p}} \tag{3.5}$$

where $c^{(i)}$, $r^{(i)}$ and $\chi^{(i)}$ are given as the material constants, $|\alpha^{(i)}|$ represents the backstress tensor magnitude, $L^{(i)}$ is defined as the unit normal in the backstress direction. The $c^{(i)}$ and $r^{(i)}$ can be found from the uniaxial tensile experiments while the $\chi^{(i)}$ is calculated from the experimental ratchetting data [18].

It is noteworthy that the material constants $c^{(i)}$ and $r^{(i)}$ determine the plastic deformation under the action of proportional loads. The $\chi^{(i)}$ is concerned with the non – proportional loading and was assumed to be large enough. Therefore, the plastic modulus could be considered as a step function regarding the plastic strain [18]. The approach presented herein to predict the ratchetting under the action of cyclic loads agrees well with the previous findings for various materials [12, 13].

3.2.2 Semi – Analytical Stress Analysis

The Hertzian contact is utilized in order to model the wheel – rail contact. It is assumed that the normal pressure is proportional to the shear loading at every point (Figure 3.2). This is evidenced by the Q/P ratio as Q refers to shear force while P represents the normal force.

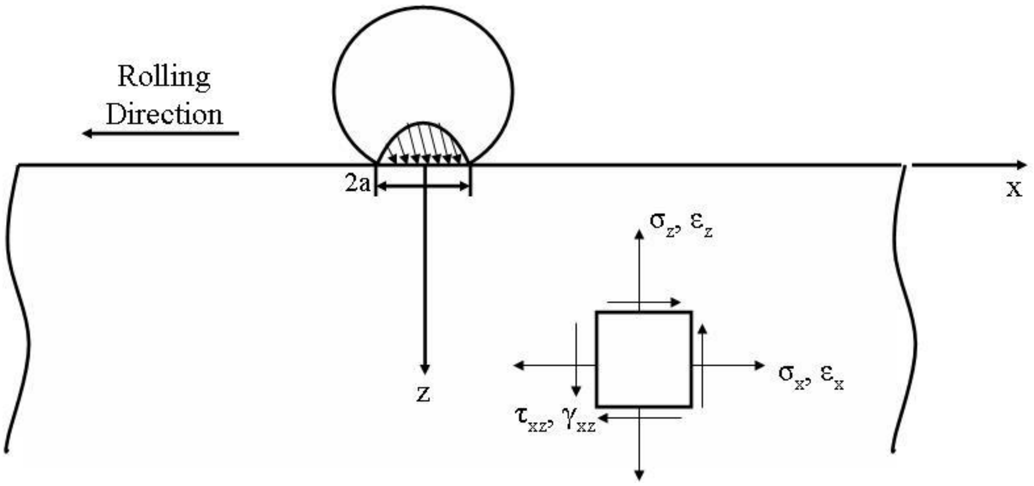

Figure 3. 2 Coordinate system utilized in the rolling contact simulations [19].

The stress in the whole body during number of cycles is assumed to be equal to the non plastic stress field. This field is determined from Smith and Liu's analysis for line contact loading scenario [20]. The stress and strain values become non – zero after each cycle but the geometry restricts these stresses and strains to become zero [11]. For this purpose, a relaxation technique is applied to make the residual stresses and strains zero. Once the residual stresses and strains are found, the surface displacement (Figure 3.3.a) or surface flow (Figure 3.3.b) can be calculated according to the formula given below:

$$\delta = \int_0^\infty (\gamma_{xz})_r \, dz \tag{3.6}$$

where δ defines the surface displacement, $(\gamma_{xz})_r$ represents the ratchetting strain at a certain depth. The surface displacement ascends with the number of cycles.

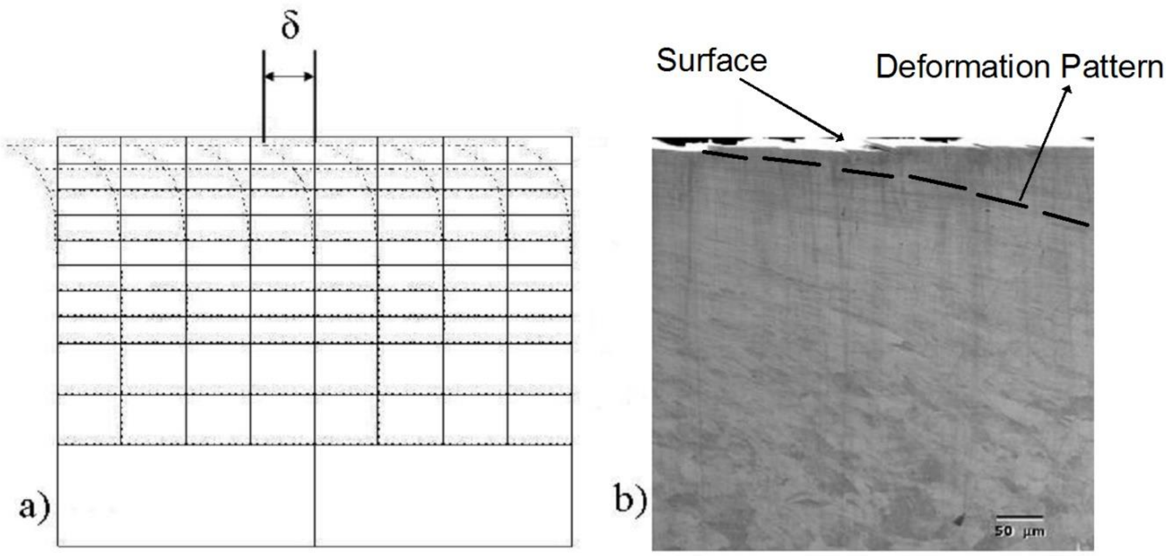

Figure 3. 3 (a) A Schematic showing the surface displacement δ due to ratchetting **(b)** The specimen surface indicating surface displacement when ratchetting experiment is complete (The disks on disk tests were carried out in order to obtain experimental results at the University of Sheffield, UK) [19].

3.2.3 Fatigue Model

A multiaxial fatigue model is utilized to predict crack initiation under the action of cyclic rolling contact loads. There have been many fatigue parameters so far to predict the critical plane: normal and shear stress ranges, maximum normal and shear stresses, normal and shear strain ranges, normal plastic strain range and maximum normal strain [21]. Nevertheless, these parameters are unable to predict the critical plane (failure plane) as demonstrated by the rolling contact experiments. The Jiang and Sehitoglu developed a model considering multiaxial fatigue parameter that is applicable to many problems under non – proportional loading [3, 22]. The fatigue parameter (FP) is as follows:

$$FP = \frac{\Delta\varepsilon}{2}\sigma_{\max} + J\Delta\gamma\Delta\tau \qquad (3.7)$$

where Δε defines the normal strain range, $\sigma_{\max}$ represents the maximum normal stress, $\Delta\gamma$ stands for the shear strain range, $\Delta\tau$ refers to the shear stress range and J is a constant. The critical plane is chosen as the one that makes the fatigue parameter maximum. The material dependent constant J is significant in terms of selecting shear stresses or normal stresses based on the fatigue parameter. The formula regarding the relation between fatigue parameter and fatigue life is defined as:

$$(FP - FP_0)^m N_f = C \tag{3.8}$$

where N_f refers to the fatigue life regarding the multiaxial fatigue parameter FP, the initial value of FP is FP_0, m and C are fatigue constants.

3.2.4 Damage Model

Every rolling cycle brings about damage to the rail material. This damage is classified into two types in the current study: the ratchetting and fatigue damage. Accordingly, these damage types change with the material depth so the damage parameter is dependent on the different depth planes. The crack initiation is dictated by the maximum damage that the plane imposes.

The crack initiation due to ratchetting is certain as shear strain accumulation reaches a threshold value. Nevertheless, rolling contact loading produces normal stresses which are associated with the material shear ductility. The material shear ductility ascends when the compressive stress plays a role, descends with decreasing tensile stress. By the way, the tensile and compressive stresses together significantly influence the shear ratchetting strain hence the ratcheting damage. This damage is expressed as:

$$\frac{dD_r}{dN} = \frac{\left| d\gamma_r / dN \right|}{\gamma_{cri}} \tag{3.9}$$

where γ_r represents the accumulated ratchetting strain, γ_{cri} defines the material failure strain determined from torsion experiments. The critical shear strain normalizes the accumulated shear strains with every cycle. The crack initiation under rolling contact occurs when the critical shear strain and accumulated ratcheting strain are in same value. However, the crack initiation is expected to occur once the ratcheting damage parameter equals unity under the light of ratchetting damage.

It is noteworthy that the obtained critical shear strain values could change in orders of magnitudes depending on the experiments for instance disk on disk or pure torsion tests [23]. Besides, pure torsion experiments were utilized to determine the γ_{cri} under rolling contact as validated by the previous works. The fatigue is effective in addition to the ratchetting as the fatigue damage parameter is as follows:

$$\frac{dD_f}{dN} = \frac{1}{N_f} = \frac{(FP)^m}{C} \tag{3.10}$$

where N_f represents the fatigue life referring to the multiaxial fatigue parameter (*FP*), *m* and *C* are denoted as the material constants. The *FP* must be larger than FP_0 in order to enable fatigue damage as indicated by Eq. (3.10). One should indicate that the FP_0 parameter is not included in Eq. (3.10) but FP_0 has been taken into account to compute fatigue damage in the material as the *FP* calculation necessitates the utility of Eq. (3.8). The damage due to the fatigue is considered to accumulate in a linear way and the obtained damage with every cycle is calculated up to the failure. The crack initiation occurs as the fatigue damage parameter reaches unity as long as only fatigue damage is introduced. Consequently, these two damage parameters can be summed in order to predict the crack initiation:

$$D = D_r + D_f \tag{3.11}$$

where D represents the accumulated total damage. The crack initiation occurs in the material as the total damage reaches unity [3]. This superposition technique regarding the fatigue and ratchetting damage previously showed that it is in good agreement with the study on rail steels under the action of cyclic loads [3]. Nevertheless, in some cases, ratchetting and fatigue damage compete each other in terms of the total damage [24]. The approach (superposition of fatigue and ratchetting damage) presented herein is based on the specific rail steels and it has been previously demonstrated that it corresponds well with the works carried out on the railroads.

3.3 Experimental Procedures and Simulation Results

3.3.1 Experimental Techniques

The chemical composition of the bainitic steel utilized in the current work is 0.26% C, 2.0% Mn, 1.81% Si and 1.93% Cr while the pearlitic steel has a composition of 0.91% Mn, 0.66% Si, 0.47% Cr and 0.79% C. Both rail steels possess body centered cubic (bcc) crystal structure at room temperature. The series of mechanical experiments were conducted on these rail steels to determine the deformation behaviors under monotonic and cyclic loadings specifically tension, compression and torsion. The specimens utilized in the experiments were obtained from rail heads. In other words, the loading axis of these specimens coincided with the rolling direction of the rails during mechanical tests leading to the realistic scenario. The monotonic torsion experiments were conducted in order to determine the plastic deformation behavior of the rail steels i.e shear yield strength. The uniaxial tension and compression tests were carried out with the purpose of finding the plasticity model constants. The tension – compression as well as torsion fatigue experiments were performed in order to determine the fatigue model parameters.

All mechanical experiments were utilized on servo hydraulic test machines under the light of digital controllers. The geometry of each specimen changed based on the loading type and appropriate digital extensometers were used in order to determine strain values accurately. The specimen utilized for uniaxial tension compression cyclic experiments had a diameter of 7 mm and a height of 15 mm with a cylindrical gauge section. On the other hand, the specimens used for torsion tests had an inner diameter of 11.2 mm and outer diameter of 14 mm with a 30 mm gauge length. The tubular specimens were selected instead of solid specimens as shear gradient is present throughout the cross – section. For the purpose of eliminating buckling and keeping the shear gradient at negligible levels, the tube wall thickness was designated as 1.4 mm. It should be kept in mind that all test findings in the current work were reproducible by the other researchers.

3.3.2 Cyclic Deformation Response and Determination of Plasticity Model Constants

The pearlitic steel is an important rail material and its mechanical properties are quietly same as 1080 steel. However, the bainitic steel has a precipitate – like microstructure (Fig. 3.4.a) while the pearlitic steel possesses lamellar structure (Fig. 3.4.b).

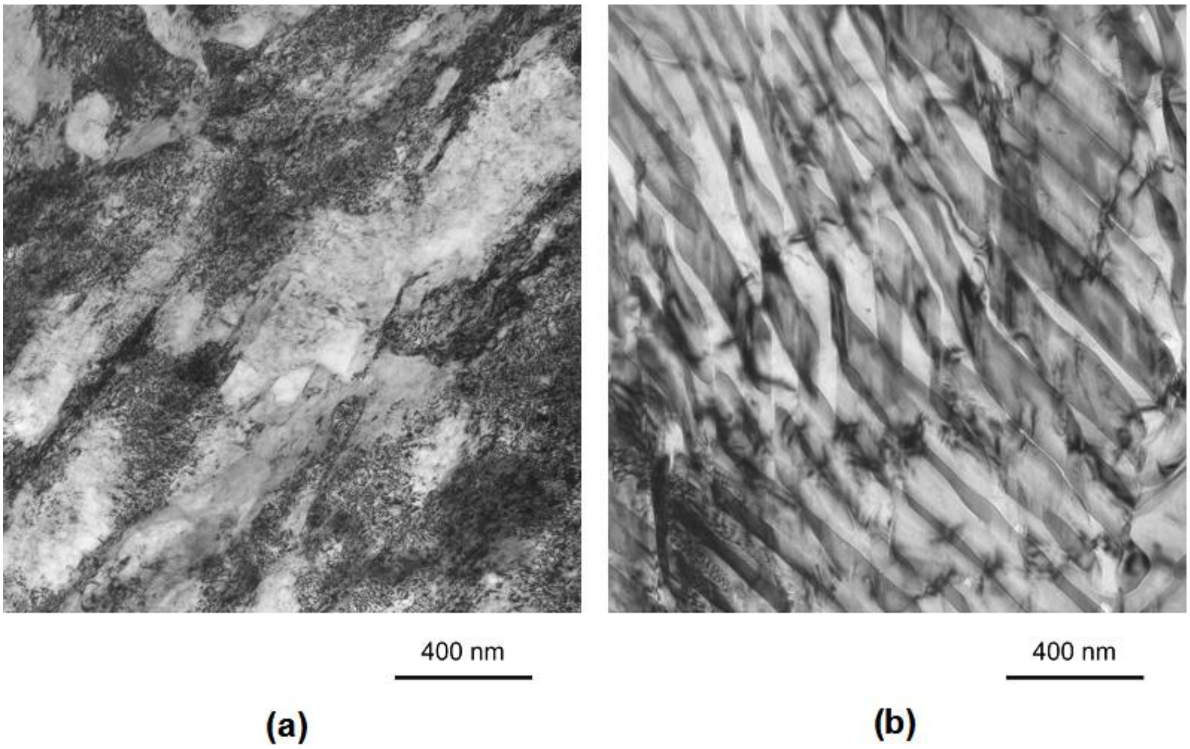

Figure 3. 4 The initial microstructures of Bainitic Steel **(a)** and Pearlitic Steel **(b)** captured by TEM [19].

The microstructures of these rail steels are obtained from individual cooling techniques during manufacturing process. It is well known that the wear resistance of the material ascends with ascending hardness. Hence, the bainitic steel is considered to be used as a rail material as it reduces railroad costs and it has more hardness than the pearlitic steel does [25, 26].

The deformation behavior of the pearlitic and bainitic steels is observed under reversed shear stress (Fig. 3.5.a and Fig. 3.5.b). The shear stress and shear strain plot of these steels up to fracture under pure torsion is presented (Fig. 3.5.c).

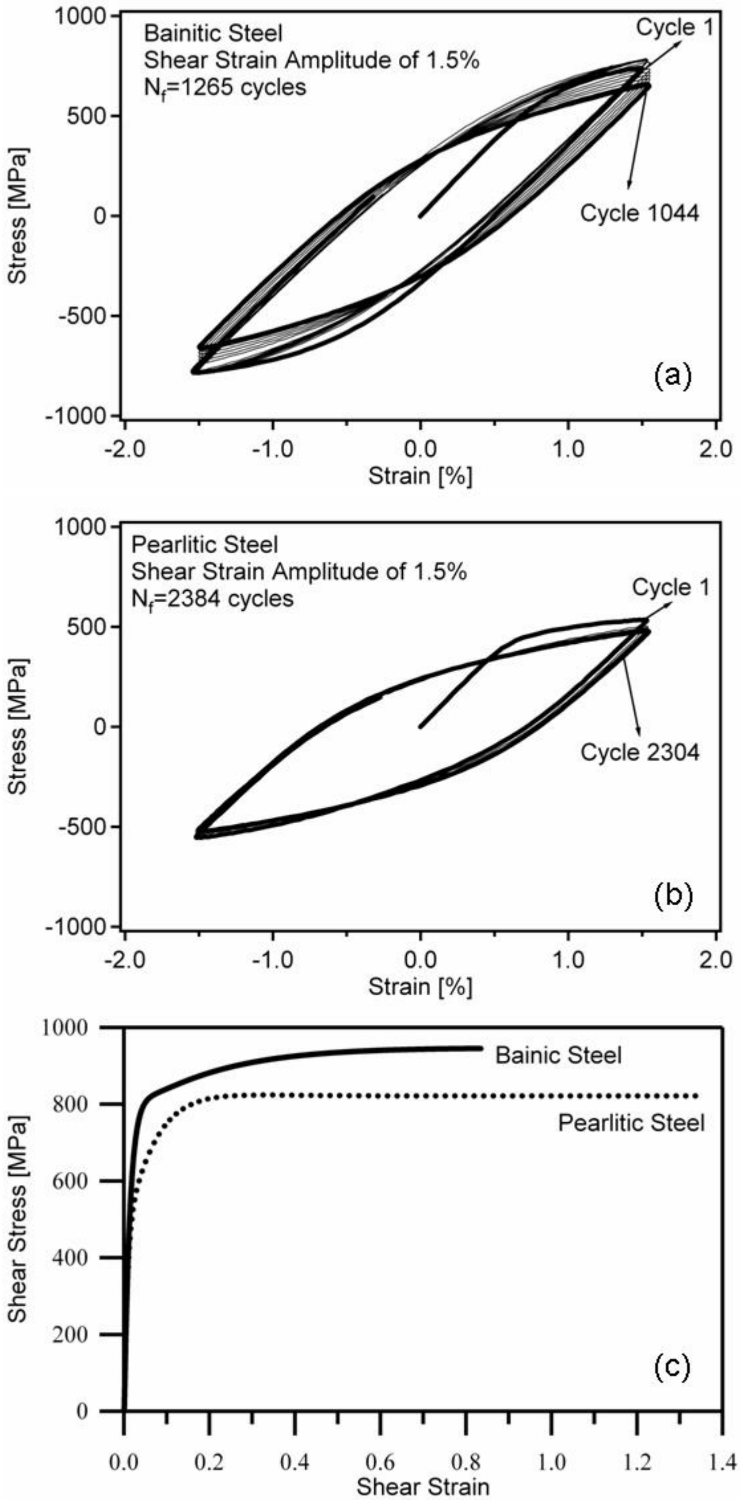

Figure 3. 5 Shear stress – Shear strain plot of the rail steels up to failure under pure torsion ((a) and (b) plot belongs to the behavior under the action of fatigue loads) [19].

The $\chi^{(i)}$ constant set is obtained from cyclic tensile – compressive ratchetting tests (Fig. 3.6 and Fig. 3.7). This approach is applied for the purpose of determining a value in order to establish compatibility of ratchetting rates between simulations and experiments. Different values of $\chi^{(i)}$ were utilized in the simulations. The simulation results then were compared with the experimental ones as it is observed for the bainitic steel in Figure 3.8.

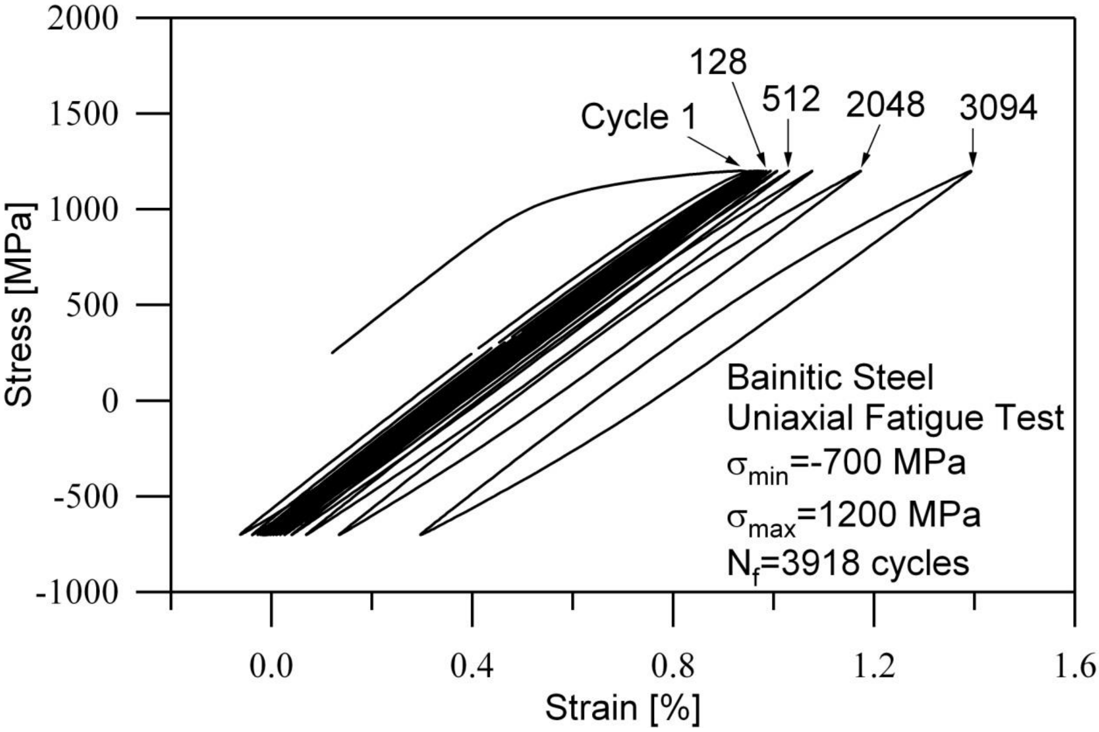

Figure 3. 6 Experimental ratchetting behavior of the bainitic steel under uniaxial fatigue loading ranging from -700 MPa to 1200 MPa [19].

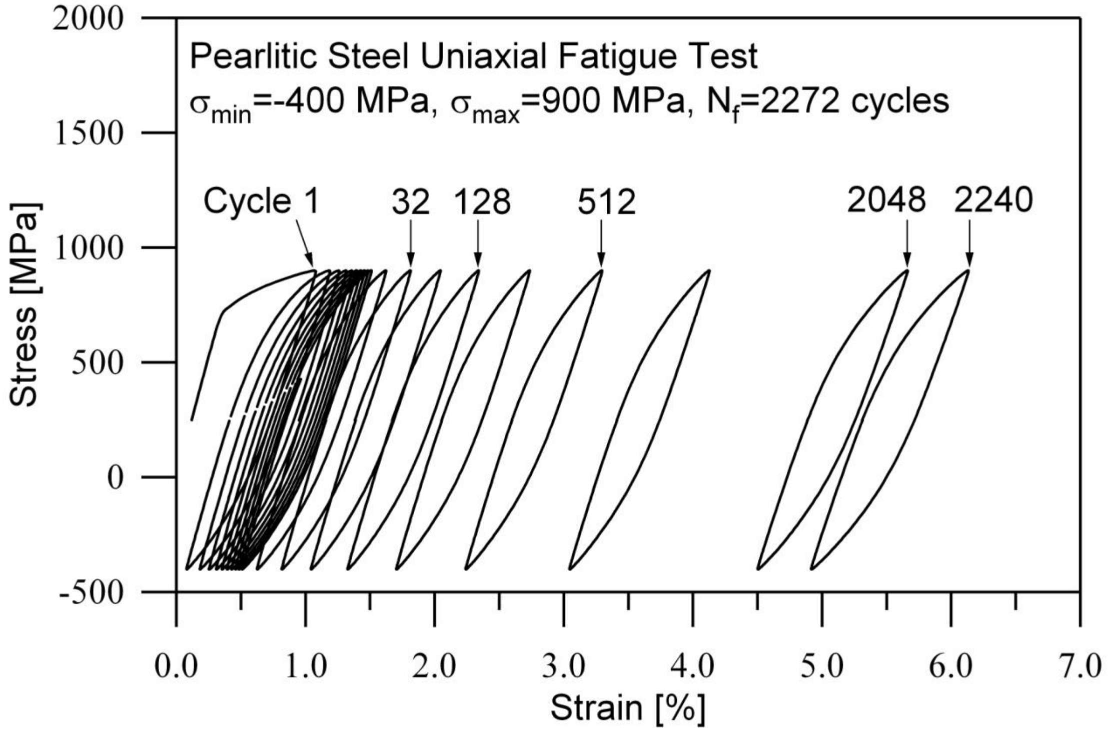

Figure 3. 7 Experimental ratchetting behavior of the pearlitic steel under uniaxial fatigue loading ranging from - 400 MPa to 900 MPa [19].

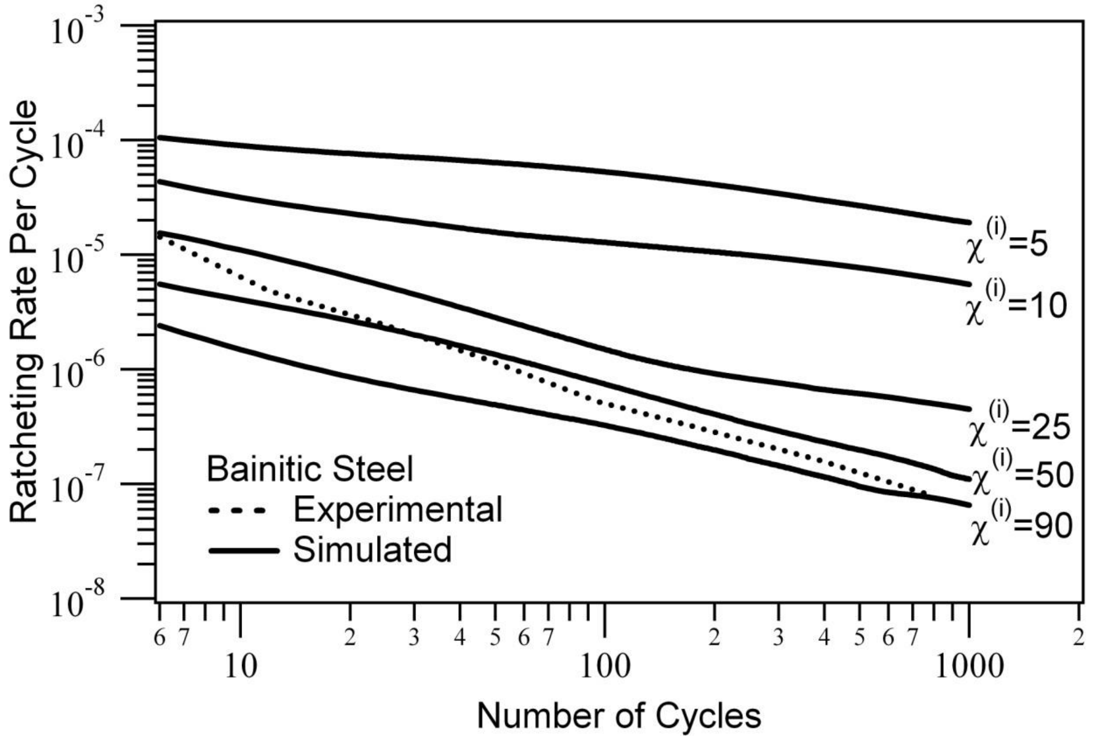

Figure 3. 8 Experimental ratchetting findings vs. simulation results for several $\chi^{(i)}$ values of the bainitic steel under uniaxial cyclic loading ranging from -500 MPa to 1200 MPa [19].

The $\chi^{(i)}$ constant sets that best predict the ratchetting behavior were explained in the following paragraphs [18]. Depending on the comparison of experimental findings and simulation ratchetting results, the $\chi^{(i)}$ was selected as 50.0 for the bainitic steel (Table 3.1). This value enables good predictions after 30 cycles as evidenced by Fig. 3.8. However, the observed deviation was considered to have less effect on the total shear strain accumulation arising from ratchetting under fatigue cycles more then 10^{6}. This is illustrated in the Fig. 3.6 that shows the experimental ratchetting behavior of the bainitic steel, indicating that considerable shear strain accumulation is observed after 512th cycle.

Bainitic Steel	
$c^{(i)}$	$c^{(1)}$=42721.1; $c^{(2)}$=17737.9; $c^{(3)}$=9567.7; $c^{(4)}$=1849.7; $c^{(5)}$=722.5; $c^{(6)}$=305.5; $c^{(7)}$=174.0; $c^{(8)}$=142.5; $c^{(9)}$=94.1; $c^{(10)}$=69.1; $c^{(11)}$=45.4; $c^{(12)}$=30.9; $c^{(13)}$=20.8; $c^{(14)}$=17.3; $c^{(15)}$=14.4; $c^{(16)}$=12.0; $c^{(17)}$=9.9; $c^{(18)}$=8.3; $c^{(19)}$=5.6; $c^{(20)}$=3.6.
$r^{(i)}$	$r^{(1)}$=20.1; $r^{(2)}$=29.4; $r^{(3)}$=53.3; $r^{(4)}$=237.1; $r^{(5)}$=143.3; $r^{(6)}$=127.1; $r^{(7)}$=37.7; $r^{(8)}$=20.9; $r^{(9)}$=61.3; $r^{(10)}$=36.1; $r^{(11)}$=13.3; $r^{(12)}$=4.5; $r^{(13)}$=11.6; $r^{(14)}$=12.7; $r^{(15)}$=16.3; $r^{(16)}$=19.6; $r^{(17)}$=22.3; $r^{(18)}$=36.1; $r^{(19)}$=49.6; $r^{(20)}$=30.8.
$\chi^{(i)}$	$\chi^{(1)}= \chi^{(2)}=\ldots\ldots= \chi^{(20)}=50.0$.
Fatigue Parameters	J=0.32; FP_0=2.75; m=2.5; C=10^6.

Table 3. 1 Material constants for bainitic steel utilized in the JS plasticity model and fatigue damage model [19].

The same procedure was applied to the pearlitic steel and $\chi^{(i)}$ was chosen as 14.0 (Table 2). Considerable shear strain accumulation in the pearlitic steel arising from ratchetting was observed after 30th cycle. However, more ratchetting tests are required in order to obtain a more appropriate value for $\chi^{(i)}$ as this is highly concerned with the non – proportional loading scenario. The $r^{(i)}$ constant was obtained from the uniaxial tension – compression experiments by preselecting $c^{(i)}$ constants while the $\chi^{(i)}$ constant determination is complete. This procedure is prosecuted with the determination of $c^{(i)}$ by preselecting $r^{(i)}$ constants [18].

Pearlitic Steel	
$c^{(i)}$	$c^{(1)}$=1166.4; $c^{(2)}$=480.3; $c^{(3)}$=340.2; $c^{(4)}$=247.4; $c^{(5)}$=181.4; $c^{(6)}$=133.9;

	$c^{(7)}$=98.4; $c^{(8)}$=73.6; $c^{(9)}$=54.8; $c^{(10)}$=41.0; $c^{(11)}$=30.6; $c^{(12)}$=22.9; $c^{(13)}$=17.2; $c^{(14)}$=12.9; $c^{(15)}$=9.6; $c^{(16)}$=7.2; $c^{(17)}$=5.4; $c^{(18)}$=4.1; $c^{(19)}$=3.0; $c^{(20)}$=2.3.
$r^{(i)}$	$r^{(1)}$=115.9; $r^{(2)}$=89.9; $r^{(3)}$=60.5; $r^{(4)}$=55.5; $r^{(5)}$=44.9; $r^{(6)}$=35.2; $r^{(7)}$=33.1; $r^{(8)}$=40.6; $r^{(9)}$=54.9; $r^{(10)}$=69.8; $r^{(11)}$=79.6; $r^{(12)}$=78.0; $r^{(13)}$=63.6; $r^{(14)}$=40.2; $r^{(15)}$=18.5; $r^{(16)}$=5.6; $r^{(17)}$=1.0; $r^{(18)}$=8.8*10^{-2}; $r^{(19)}$=3.3*10^{-3}; $r^{(20)}$=3.8*10^{-5}.
$\chi^{(i)}$	$\chi^{(1)}= \chi^{(2)}=\ldots\ldots= \chi^{(20)}$=14.0.
Fatigue Parameters	J=0.32; FP_0=0.5; m=2.5; C=1.5*10^6.

Table 3.2 Material constants for pearlitic steel utilized in the JS plasticity model and fatigue damage model [19].

The J, FP_0, m and C constants that are implemented into the fatigue model were determined from the uniaxial tension – compression tests as well as torsional cyclic loading of the cylindrical and tubular specimens [3]. The best parameters for bainitic and pearlitic steels which successfully fit the fatigue curve to the experimental one are observed (Figs. 3.9 and 3.10, Tables 3.1 and 3.2).

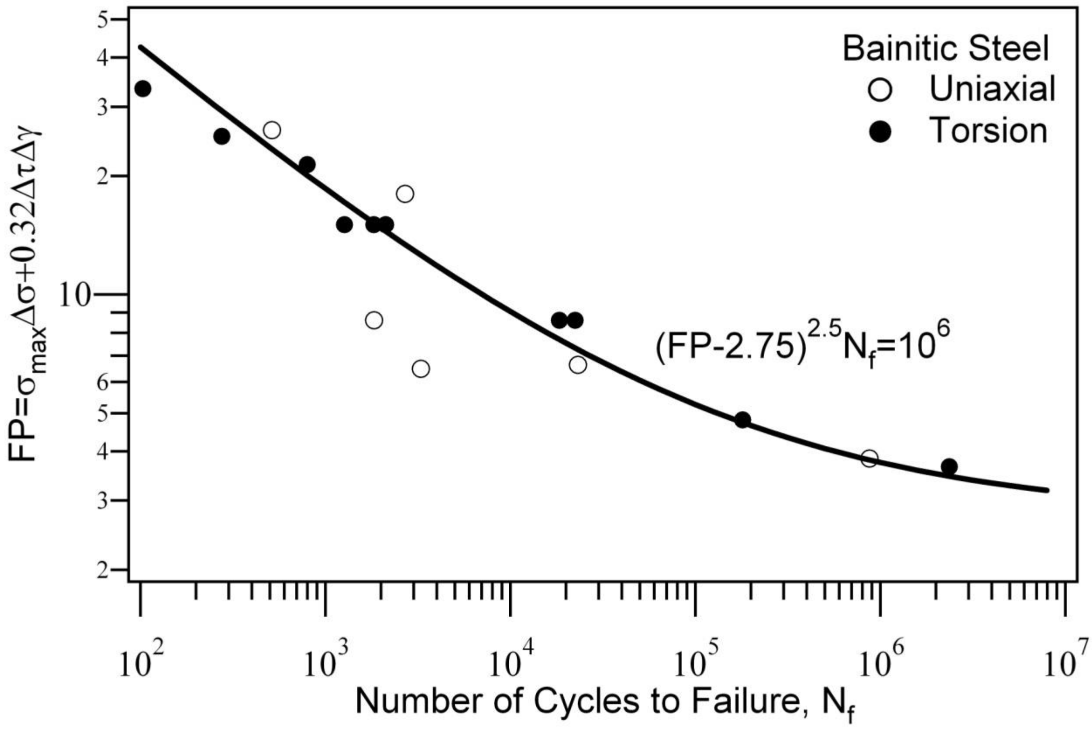

Figure 3. 9 Fatigue results for uniaxial and torsional tests on bainitic rail steel [19].

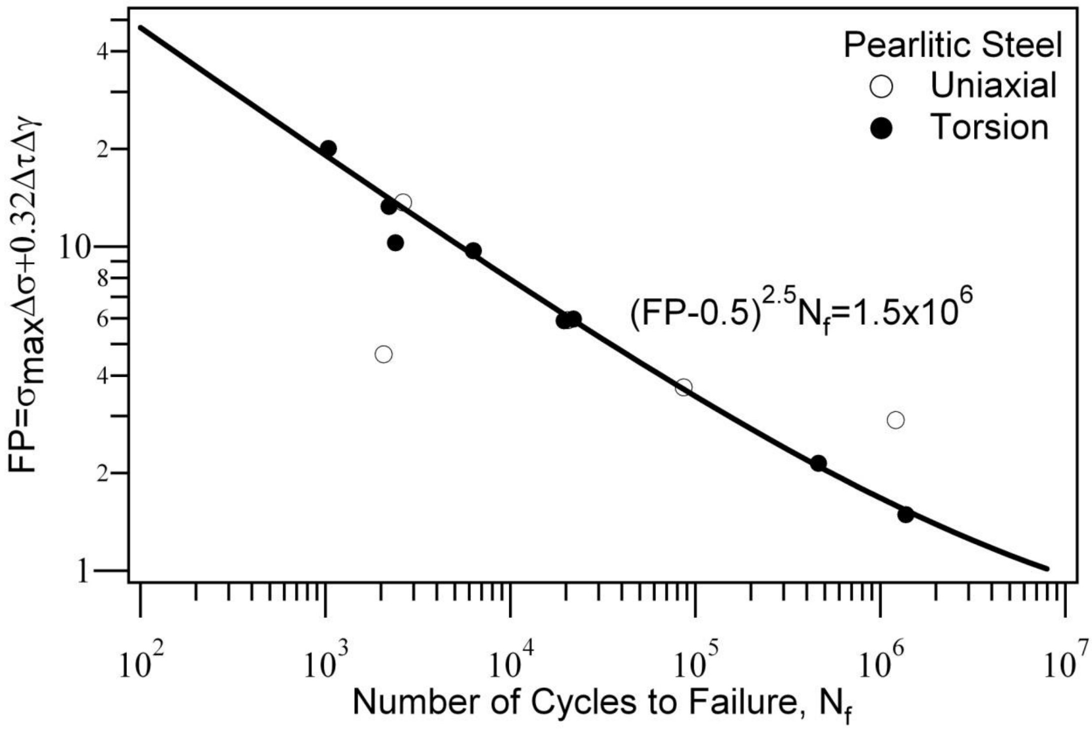

Figure 3. 10 Fatigue results for uniaxial and torsional tests on pearlitic rail steel [19].

3.3.3 Rolling Contact Simulations

The surface displacements under normal load (p_0 = 900 MPa) and various tangential loads were computed for both steels with the JS model (Fig. 3.11). The plastic shakedown is observed in the bainitic steel while constant surface displacement is present in the pearlitic steel after an initial transient period. However, crack initiation life prediction can be made due to the applied normal and shear loads once the crack initiation data is computed for both rail steels (Fig. 3.12 and Fig. 3.13). At this point, the authors took advantage of crack initiation map which is defined as a diagram displaying the shear and normal loads to the fatigue failure with the number of cycles. The contact simulations were performed up to only 10^3 or 10^4 cycles due to computational restrictions. It should be noted that the number of cycles more than 10^3 or 10^4 are usually desirable in the fatigue crack initiation maps. However, when the damage vs. number of cycles is plotted logarithmically, the resultant curve is observed to be almost linear after an initial transient region meaning that 10^3 cycles are sufficient. The total damage can then be found for higher number of cycles by extrapolation method.

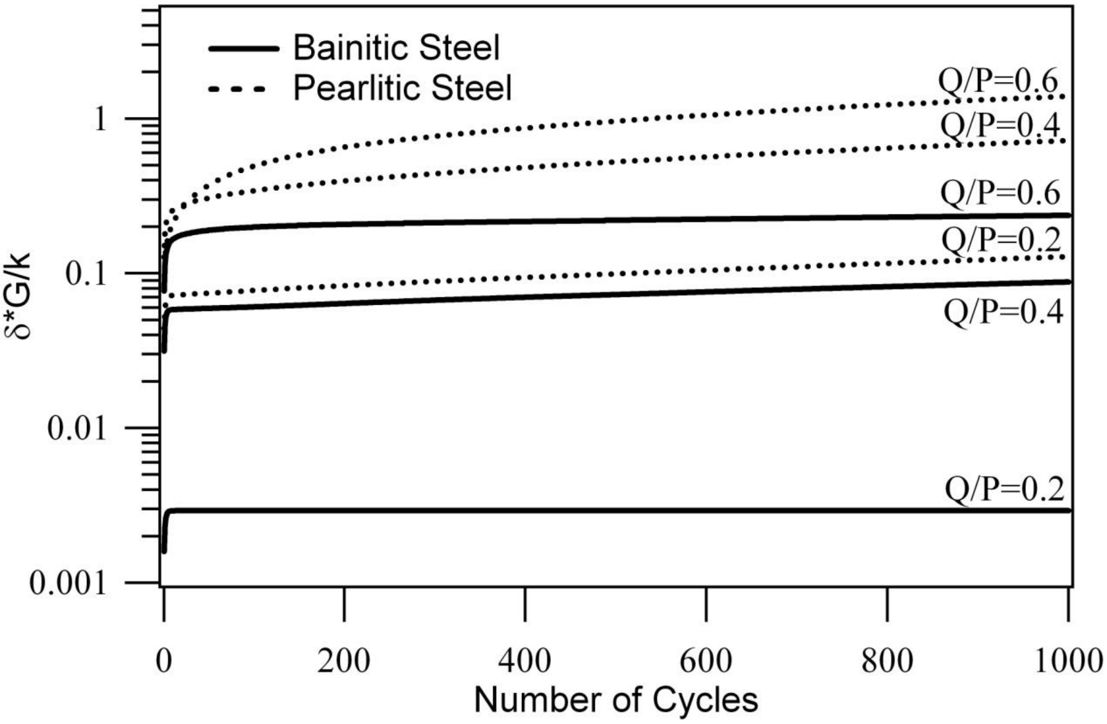

Figure 3. 11 Surface displacements of the bainitic and pearlitic steel arising from ratchetting under the action of normal load of 900 MPa [19]. (Q : Shear force, P : Normal force)

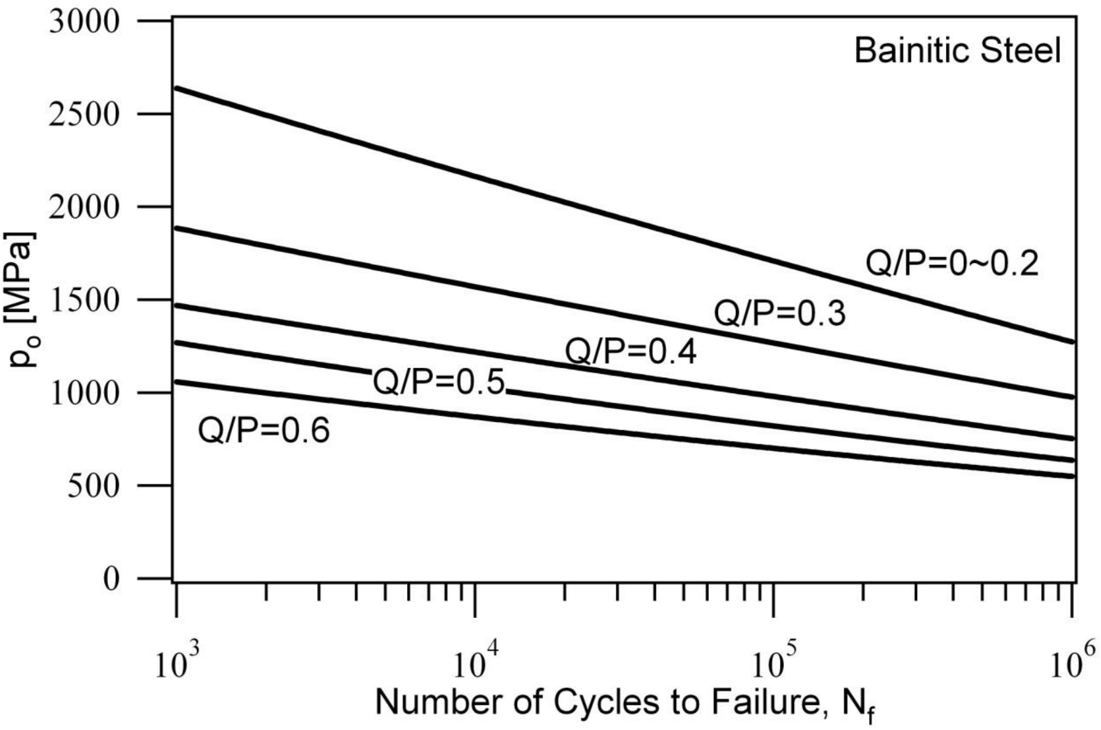

Figure 3. 12 The crack initiation life for bainitic steel under the action of normal and shear loads [19].

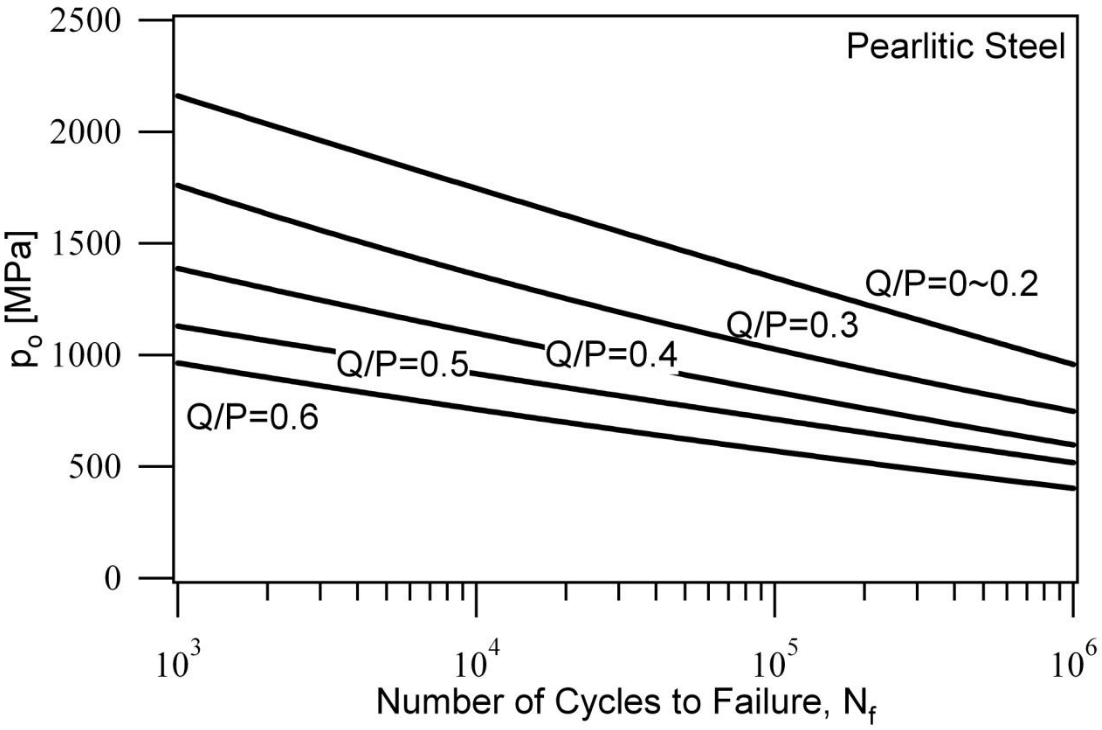

Figure 3. 13 The crack initiation life for pearlitic steel under the action of normal and shear loads [19].

The crack initiation life was determined for various loading scenarios up to the failure above 10^4 and 10^6 cycles in the current work (Fig. 3.14). It is inferred from the contact simulations that the load curves change gradually as Q/P ratio is smaller than 0.2 or bigger than 0.5. For the rest of Q/P values, the crack initiation data remains in the transient region.

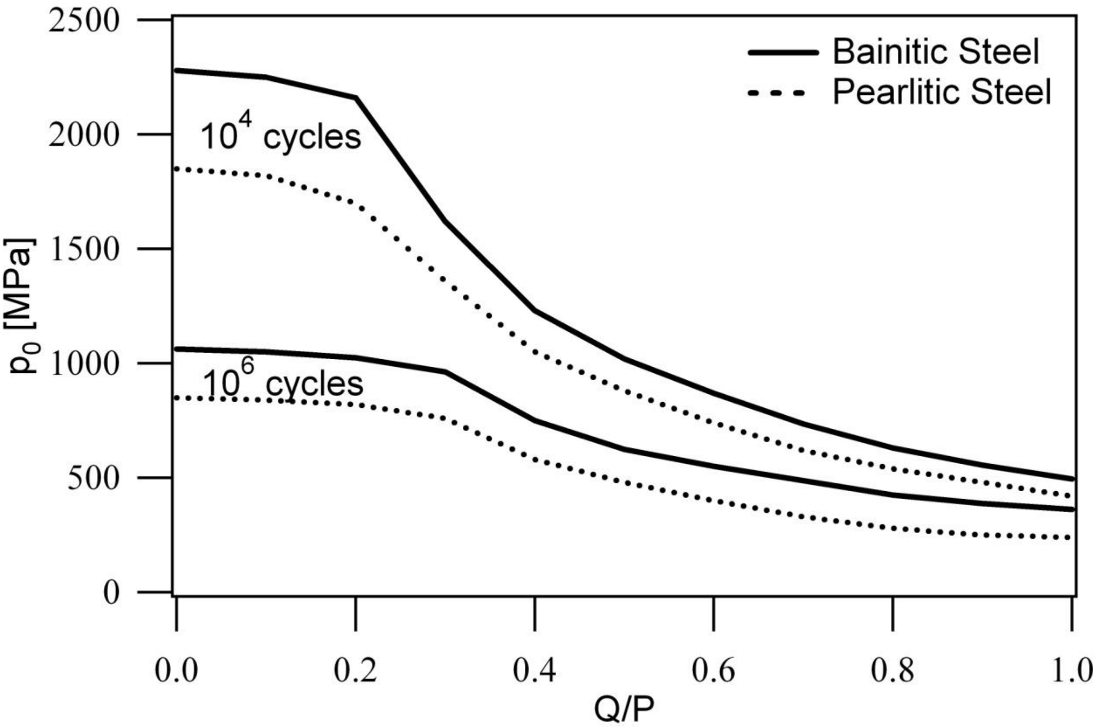

Figure 3. 14 A fatigue crack initiation map that displays the loading conditions of pearlitic and bainitic steel up to the failure [19].

3.4 Discussion

The $\chi^{(i)}$ constants that are used in the JS plasticity model dictate the ratchetting rate decay. It was observed from ratchetting experiments that bainitic steel displays higher ratchetting rate decay when compared to the pearlitic counterparts. This is demonstrated by the $\chi^{(i)}$ values (Tables 1 and 2). However, the surface displacement of the bainitic steel is lower than that of the pearlitic steel as it is defined as an integral summation of the ratchetting strain. Therefore, ratchetting arrest is observed in the bainitic steel (Fig. 3.11). On the other hand, ratchetting rate decay is lower in the pearlitic rail steel and ratchetting is present with more loading. As a result, the pearlitic steel has higher surface displacement than the bainitic steel does and the reason lies on the ratchetting rate decay as well as the lower yield stress.

The damage parameter is described as the summation of accumulated ratchetting and fatigue damage. The fatigue parameter is subjected to the range of normal stress/strain as well as the shear stress/strain. The maximum stress is observed at the contact points as evidenced by the Smith – Liu stress distributions. In our case, the fatigue damage reaches maximum value at the surface and begins to descend while the critical plane becomes embedded.

Ratchetting damage accumulation is another consequence of the cyclic loading. The ratchetting damage is dependent on the ratchetting strain as clearly observed by the equation 3.9. Furthermore, the loading scenario can change the depth where maximum ratchetting damage and ratchetting strain build up. The maximum ratchetting damage is observed subsurface as Q / P ratio is smaller than 0.2. However, the maximum ratchetting damage is found on the surface while the Q / P ratio exceeds 0.3.

It is important to mention that the ratchetting damage and fatigue damage occur on different planes. Specifically, ratchetting damage occurs on maximum shear strain plane while fatigue damage is observed on the plane which maximizes the fatigue parameter. However, the authors do not know the integration of these damage mechanisms as they occur at discrete planes. The authors developed an approach that considered the fatigue and ratchetting damage separately and added their effects to the cumulative damage. This method has been conducted previously [13]. However, further work is required in order to determine the material plane more accurately.

As the total damage consists of ratchetting and fatigue damage, the depth where maximum damage is observed, is associated with the shear force. The maximum fatigue damage occurs on the surface while the maximum ratchetting damage is observed to be subsurface as the Q / P ratio is smaller than 0.2. Once the ratchetting and fatigue damage are summed on separate planes, the maximum total damage is observed to be present subsurface. However, while the Q / P ratio exceeds 0.2, the total damage accumulation ascends and the critical load descends. As the Q / P ratio is in the interval of 0.3 and 0.4, the maximum ratchetting damage is considered to be on the surface. When the maximum ratchetting damage and maximum fatigue damage coincide on the surface, a significant increase is observed in the total damage leading to drop – offs in the critical loads (Fig. 3.14). As the Q / P ratio exceeds, the maximum fatigue and ratchetting damage are observed to be on the surface and further ratio increase gives way to significant drop – offs in the critical load.

The pearlitic and bainitic steels considerably differ when compared in the fatigue crack initiation maps. As Q / P ratio < 0.2 – 0.3, the bainitic steel is preferable over pearlitic steel in terms of withstanding critical loads. As this ratio ascends, the difference between two rail steels descends rapidly. It is demonstrated in Fig. 3.5.c that the bainitic steel has higher yield stress value but the pearlitic steel is more ductile. However, the strength becomes importance as fatigue damage plays a major role under the action of normal loads while Q/P ratio has small values. In this scenario, the bainitic steel is preferred over pearlitic steel as it is capable of resisting higher critical load. On the other hand, while the Q / P ratio ascends, an increase in shear forces begins to be higher than that of the normal forces. In this way, the ratchetting damage plays a key role and the ductility property prevails. Specifically, as Q / P ratio gradually increases from 0.2 to 0.4, surface flow increases drastically (Fig. 3.11). This requires the material ductility and the bainitic steels' insufficient ductility becomes a drawback in terms of withstanding the critical loads. These loads bring about crack initiation when the number of cycles reaches 10^{6}.

It should be noted that the current findings correspond very well with the literature. For instance, the current work reveals the two failure mechanisms in the specific rail steels: fatigue damage and ratchetting damage. The former is subjected to the repeated cyclic loading whereas the latter is subjected to the directional shear strain accumulation. These mechanisms were previously studied in the 1070 steel [13]. Furthermore, the experimental findings and simulated ratchetting rate decay of these two rail steels as well as the maximum damage prediction when Q / P ratio is 0.5 stands in good agreement with the work of Jiang and Sehitoglu [3]. It has been also demonstrated that the rolling contact failure occurs in both steels as p_0 / k ratio is larger than 4.0 [3]. As the Q / P ratio is between 0.2 – 0.5, the cracks arising from fatigue loading do not cause rolling contact failure.

The previous study by Sawley and Kristan demonstrated the usage of bainitic steel over pearlitic steel under rolling contact loading [27]. The bainitic steel undergoes less ratchetting damage when compared to the pearlitic steel as it has higher yield strength as well as more toughness. However, the bainitic rail steel is able to tolerate larger sized cracks when compared to the pearlitic steel as it has higher fracture toughness. This is the another advantage of bainitic steel over pearlitic steel [27].

The important finding in the current study in that fatigue damage dictates the crack initiation when the shear tractions are low and ratchetting damage is the dominant failure mechanism as the shear tractions increase. Another considerable result is that bainitic steel is preferred over pearlitic steel when the shear tractions are low but both rail steels' performances under rolling contact loading approach each other at higher shear tractions.

3.5 Conclusions

The deformation behaviors of pearlitic and bainitic rail steels were analyzed with the help of JS semi analytical plasticity model under cyclic rolling contact loading. The crack initiation life for both rail steels was predicted for different shear and normal loading scenarios including multiaxial ratchetting and fatigue failure mechanisms. In particular, as the Q / P < 0.2, maximum fatigue damage is observed to be below surface but the maximum ratchetting damage occurs subsurface. While this ratio exceeds 0.3, maximum ratchetting is observed to be on the surface. However, the crack initiation is not critical while the Q / P is between 0.2 – 0.5 in the fatigue crack initiation map. As the Q / P = 0.3, the maximum fatigue damage and maximum ratchetting damage coincide on the surface leading to a significant decrease in the fatigue crack initiation map. Furthermore, high shear tractions give way to a considerable decrease in fatigue lives as compared to pure rolling scenario.

The crack initiation is dictated by the fatigue damage at low tangential to normal loads whereas it is controlled by the ratchetting damage as the shear tractions increase. When ratchetting damage and fatigue damage coincide on the surface, significant contribution to the cumulative damage occurs. This results in catastrophic fatigue failure for bainitic and pearlitic rail steels which is clearly observed by a drop – off in the critical load in the fatigue crack initiation maps. The bainitic steel is able to withstand higher critical loads when compared to the pearlitic steel under the action of rolling contact loads as the shear tractions are small. As the shear tractions increase, higher ratchetting damage is observed in the bainitic steel due to lack of ductility. This results in proximity in these rail steels' performances.

Next chapter details the extension of the multi-scale modeling approach presented in Chapter 2 to a potential biomedical implant material, namely the niobium-zirconium (Nb-Zr) alloy. Specifically, the impact response of the Nb-Zr alloy was investigated in detail by incorporating the role of fine microstructural effects.

3.6 References

[1] D. Canadinc, H.Sehitoglu, K. Verzal, Analysis of crack growth under rolling contact fatigue. International Journal of Fatigue 30 (2008) 1678

[2] G. Donzella, M. Faccoli, A. Ghidini, A. Mazzu, R. Roberti, The competitive role of wear and RCF in a rail steel, Engineering Fracture Mechanics 72 (2005) 287

[3] Y. Jiang and H. Sehitoglu, A model for rolling contact failure, Wear 224 **(**1999) 38

[4] T. E Tallian, Simplified contact fatigue life prediction model: Part I, Review of published models, *ASME* Journal of Tribology 114 (1992) 207

[5] T. E. Tallian, Rolling bearing life prediction, Corrections for material and operating Conditions: Part I. General model and basic life. Part II. The correction factors,
ASME Journal of Tribology 110 (1998) 2

[6] T. E. Tallian, Simplified contact fatigue life prediction model: Part II. New model, ASME Journal of Tribology 114 (1992) 214

[7] E. Ioannides, T. A. Harris, A new fatigue life model for rolling bearings, ASME Journal of Tribology 107 (1985) 367

[8] H. Schlicht, E. Schreiber, and O. Zwirlein, Fatigue and failure mechanism of bearings, Proceedings, Institution of Mechanical Engineers London C 285 (1986) 85

[9] G. Lundberg, A. Palmgren, Acta Polytechnica, Mechanical Engineering Series 1, 1947 No 3

[10] A. D. Hearle, K. L. Johnson, Cumulative plastic flow in rolling and sliding line contact, ASME Journal of Applied Mechanics 54 (1987) 1

[11] J. E. Merwin, K. L. Johnson, An analysis of plastic deformation in rolling contact, Proceedings of the Institution of Mechanical Engineers London 177 (1963) 676

[12] Y. Jiang, H. Sehitoglu, Modeling of cyclic ratchetting plasticity, Part I: Development of constitutive relations, Journal of Applied Mechanics 63 (1996) 720

[13] Y. Jiang, H. Sehitoglu, Rolling contact stress analysis with the application of a new plasticity model, Wear 191 (1996) 35

[14] F. Sadeghi, B. Jalalahahmadi, T. Slack, N. Raje, N. Arakere, A review of rolling contact fatigue, Journal of Tribology 131 (2009) 1

[15] I. I. Kudish, K. W. Burris, Modern state of experimentation and modeling in contact fatigue phenomenon: Part 2–Analysis of the existing statistical mathematical models of bearing and gear fatigue life. New statistical model of contact fatigue, Tribology Transactions 43 (2000) 293

[16] J. W. Ringsberg, Life prediction of rolling contact fatigue crack initiation, International Journal of Fatigue 23 (2001) 575

[17] J. W. Ringsberg, Cyclic ratchetting and failure of a pearlitic rail steel, Fatigue and Fracture of Engineering Materials and Structures 23 (2000) 747

[18] Y. Jiang, H. Sehitoglu, Modeling of cyclic ratchetting plasticity. Part II: Comparison of model simulations with experiments, ASMA Journal of Applied Mechanics, 63 (1996) 726

[19] O.Onal, D.Canadinc, H.Sehitoglu, K.Verzal, Y.Jiang, Investigation of rolling contact crack initiation in bainitic and pearlitic rail steels, Fatigue and Fracture of Engineering and Material Structures 35 (2012) 985

[20] J. O. Smith, C. K. Liu, Stresses due to tangential and normal loads on an elastic solid with application to some contact stress problems, Journal of Applied Mechanics 20 (1953) 157

[21] D. F. Socie, G. B. Marquis, Multiaxial Fatigue. SAE, Warrendale PA, 2000

[22] H. Sehitoglu, Y. Jiang, Fatigue and stress analyses in rolling contact, Technical Report, Materials Engineering– Mechanical Behavior, College of Engineering, University of Illinois at Urbana-Champaign 1992

[23] P. Clayton, X. Su, Surface initiated fatigue of pearlitic and bainitic steels under water lubricated rolling/sliding contact, Wear 200 (1996) 63

[24] W. R. Tyfour, J. H. Beynon, A. Kapoor, Deterioration of rolling contact fatigue life of pearlitic rail steel due to dry-wet rolling-sliding line contact, Wear 197 (1996) 255

[25] K. M. Lee, A. A. Polycarpou, Wear of conventional pearlitic and improved bainitic steels, Wear 259 (2005) 391

[26] D. Canadinc, H. Sehitoglu, H. J. Maier, P. Kurath, On the incorporation of length scales associated with pearlitic and bainitic microstructures into a visco-plastic self-consistent model, Materials Science and Engineering A 485 (2008) 258

[27] K. Sawley, J. Kristan, Development of bainitic rail steels with potential resistance to rolling contact fatigue, Fatigue and Fracture of Engineering Materials and Structures 26 (2003) 1019

CHAPTER 4: MULTIAXIAL MODELING OF THE IMPACT RESPONSE OF NIOBIUM – ZIRCONIUM (NbZr) ALLOYS

4.1 Introduction

The developments in materials science have triggered the medical field as the number of medical products has sharply increased. The metallic materials especially nickel – titanium shape memory alloys are utilized in various treatments [1-3] specifically the tooth implant screws as well as some dental implants [3, 4]. The advantages of the metallic materials are biocompatibility, formability and high strength [1 – 4]. The latter also provides sufficient resistance against impact deformation during working.

There are few studies studies reported concerning the implant failure (fracture) under fatigue loading [4-6]. This is due to unsuccessful treatment, also may bring about infection as well as many other consequences. The importance of these consequences is well understood by investigating the occurrence of the implant fracture. Therefore, establishing the knowledge between the fracture and impact behavior of implant materials plays a key role in terms of implant design.

Niobium – zirconium (NbZr) alloys are good candidates as implant materials and their importance has been the major focus of recent studies [7 – 9]. These alloys have attracted many researchers in the biomedical field due to their excellent corrosion resistance as well as biocompatibility [7 – 9]. Previous studies have shown that high strength and superior fatigue resistance can be attained in these alloys while the ultrafine – grained (UFG) microstructure is achieved [10 – 13]. Among other biomaterials, UFG NbZr alloys prevail to be used in implants due to their good mechanical properties and biocompatibility.

It is well known that human body has chemically aggressive environment. Thus, contact between implant material and body fluids becomes a vital issue. For instance, implant materials must be resistant against the corrosion in the human body. On the other hand, the mechanical properties especially good fatigue resistance and fracture toughness are considerable in order to enable better biocompatibility as implant materials are in service under harsh loading conditions [14 – 17]. A typical example for these loading conditions is impact as falling or jumping actions which cause severe injuries in the body, especially hip or knee joint fractures as well as dental implant fractures [18 – 22, 4– 6]. However, the fracture behavior is imposed by the impact strength so that impact testing is required in order to enable the safety and appropriate mechanical performance of the implant material. Thus, the purpose of the current work is to analyze the impact response of UFG NbZr and to generate knowledge about its potential use as a biomedical implant.

The microstructural features including grain size, grain boundaries and precipitates as well as ductile to brittle transition temperature (DBTT) significantly influences the impact performance [23 – 25]. The grain refinement, the existence of delaminations and precipitates dramatically decreases the DBTT [24, 25] as these features have a tendency to ascend the energy levels for the crack propagation. The texture which is defined as the non – random distribution of grain boundary misorientation angles substantially affects the impact response of the UFG materials. High – angle grain boundaries (HAGBs) act as barriers in order to hinder dislocation motion leading to a decrease in crack propagation rates. This also reduces DBTT values and increases fracture toughness [24 – 28]. Another consequence of texture (also defined as the degree of anisotropy) is that it influences the relative slip mechanism in each grain [29]. The effect of anisotropy relies on changing the overall deformation response that is based on the applied load. Specifically, anisotropy is influenced by the loading direction. For instance, the material fails in a ductile manner in one loading direction while brittle failure can occur in another direction. This is explained by the different slip mechanisms for each case [30, 31].

It is noteworthy that bone has a high degree of anisotropy so that the importance of anisotropy prevails in terms of implant design by replacing bone tissue [32, 33]. Therefore, mimicking bone tissue is crucial such that the implant material should have similar mechanical properties as well as similar anisotropy to that of the bone. Successful implant design requires the understanding of relationship between impact and anisotropy as impact loading is critical especially for dental and orthopedic implants [18 – 22]. A previous study evidenced the dependence of impact response on the anisotropy in the UFG NbZr alloys [13]. In particular, the energy absorption values due to impact vary depending on the different orientations of the UFG NbZr variants with respect to the extrusion direction (ED). For instance, the variant possesses a ductile behavior when it is oriented perpendicular to the ED while a brittle behavior is observed when it is oriented at a 26^{0} angle to the ED. However, the variant oriented along the ED was found to have the highest impact energy absorption that is triggered by the microstructural elements i.e delaminations [13].

In the current work, authors aimed to consider the anisotropy phenomenon for the successful implant design. By this way, possible mechanical failure can be eliminated and the effects of consequences can be significantly reduced if failure occurs. However, the current work presents an approach which benefits from the combination of experimental and numerical procedures. Specifically, coarse – grained (CG) and UFG NbZr alloys were experimentally analyzed to investigate the anisotropy effects by comparing their microstructures according to their uniaxial tensile stress / strain and impact responses. The role of anisotropy was determined with the crystal plasticity simulations and was successfully incorporated into the finite element (FE) impact simulations. The current results show that texture and the corresponding anisotropy have considerable effects on the impact response. However, the appropriate coupling of crystal plasticity and finite element simulations shed light on the accurate predictions of the impact response. The approach utilized in the current work can be a roadmap for successful design of orthopedic and dental implants.

4.2 Experimental Procedures and Results

The chemical composition of the NbZr alloy utilized in the current study is 2.33 wt.% Zr, 0.29 wt.% Ta, 76 ppm H_2, 44 ppm O_2, 63 ppm C, 5 ppm Fe and balance Nb. The NbZr alloy was attained in CG microstructure as a hot rolled plate with a thickness of 30 mm. The UFG microstructure was obtained from a specific technique called equal channel angular pressing (ECAP) [10 – 12]. The extracted specimens for both UFG and CG case were dog – bone – shaped type with a gauge section of 8 mm x 3 mm x 1.5 mm. However, the focus was given to the UFG NbZr samples extracted from the extruded billets [10 – 12, 30 – 31]. The uniaxial tensile experiments were performed under the action of monotonic loads with the help of a servo – hydraulic loading frame at room temperature. The strain rate was selected as 5×10^{-4} s^{-1} which is relatively minimum for the purpose of eliminating strain rate effects. The stress – strain responses of CG and UFG NbZr alloys at room temperature are illustrated (Figure 4.1).

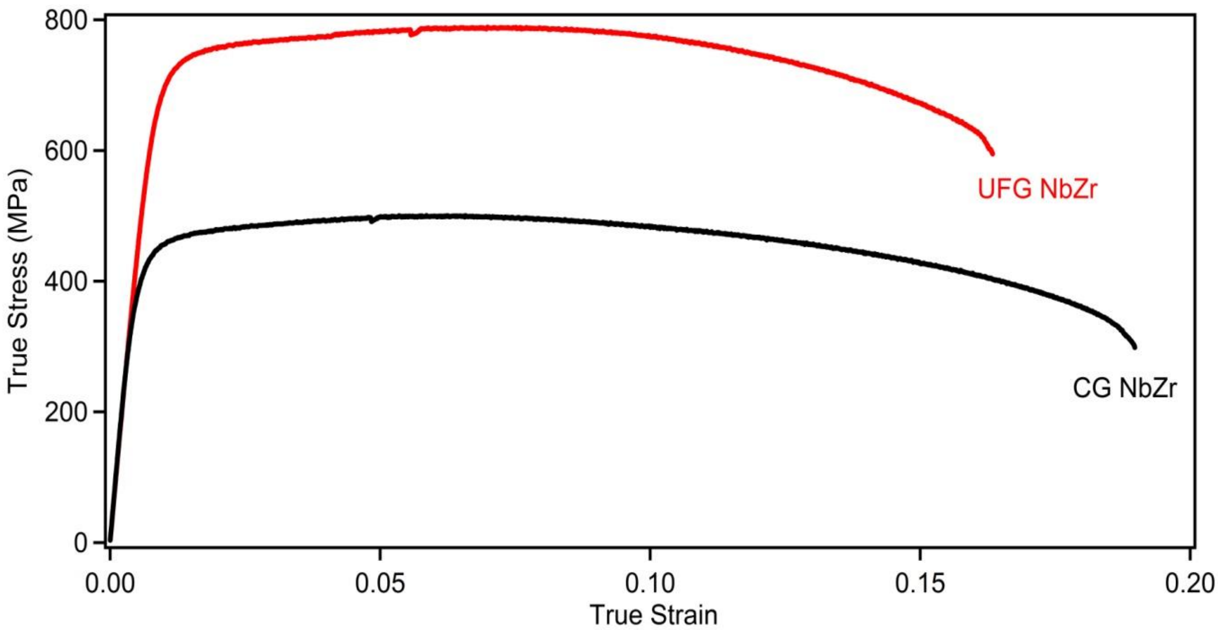

Figure 4. 1 The uniaxial stress – strain responses of UFG and CG NbZr alloys at room temperature [34].

It is shown in Fig. 4.1 that UFG NbZr alloy has more strength values compared to the CG NbZr alloy. This is due to the severe plastic deformation leading to grain refinement in the UFG alloys obtained during ECAP [10 – 12]. The major advantage of the UFG materials is that the ductility remains constant while the strength increases sharply such that excellent combination of strength – ductility is achieved.

The extracted impact samples for both the CG and UFG NbZr alloys had dimensions of 2.8 mm x 25 mm x 4 mm with a 60 ^{o} notch angle and 0.1 mm notch depth [32]. The impact specimens were subjected to mechanical polishing down to a 4000 grit size. This procedure was applied to eliminate the effects of machined surfaces. It is illustrated in that the impact experiments were carried out at 50 ^{0}C, 0 ^{0}C, -50 ^{0}C, -100 ^{0}C and -150 ^{0}C temperatures. The impact velocity was determined as 3.8 m/s and the impact energy was calculated as 50 J (Figure 4.2). As the temperature is down to – 100 ^{0}C, ductile to brittle transition behavior is observed in the UFG and CG NbZr alloys. In particular, UFG NbZr alloys absorb higher energy compared to its CG counterpart that is evidenced by the more apparent ductile to brittle transition region shown in Fig. 4.3 This indicates that UFG NbZr is more sensitive to variations in temperature.

Figure 4. 2 The test machine utilized in NbZr impact deformation.

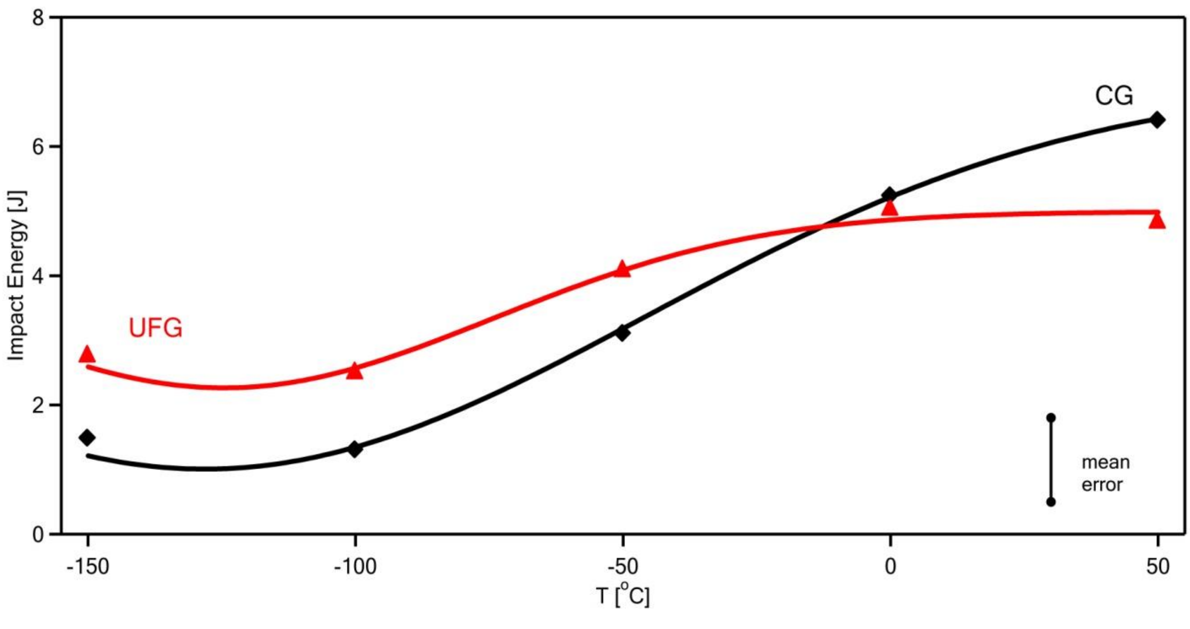

Figure 4. 3 Impact energy vs. Temperature plot for UFG and CG NbZr alloys [34].

In the current study, the impact response of NbZr alloy was analyzed at a temperature of 50 ^{0}C. This temperature value is chosen as it presents the ideal conditions for implants (i.e storage, sterilization). The recorded force vs. time data for CG and UFG alloys at a temperature of 50 ^{0}C is displayed in Fig 4.3. The UFG NbZr absorbs more energy compared to its CG counterpart up to crack propagation starting point. However, the CG NbZr is more ductile (Figure 4.1) and absorbs more energy during the entire impact test (Figure 4.4).

To validate the experimental findings, microstructural analysis was conducted utilizing scanning electron microscope focusing on the fracture surfaces of CG and UFG NbZr alloys after impact test. It is inferred from the SEM results that larger plastic strains are observed in the UFG NbZr. This is due to more slip activity leading to more distorted fracture surface when compared to the CG NbZr as demonstrated in Fig. 4.5. It is also observed in Fig. 4.5 that the elongated grains are in the same direction with the crack growth. Moreover, crack propagation occurs throughout the grain boundaries (Figure 4.5).

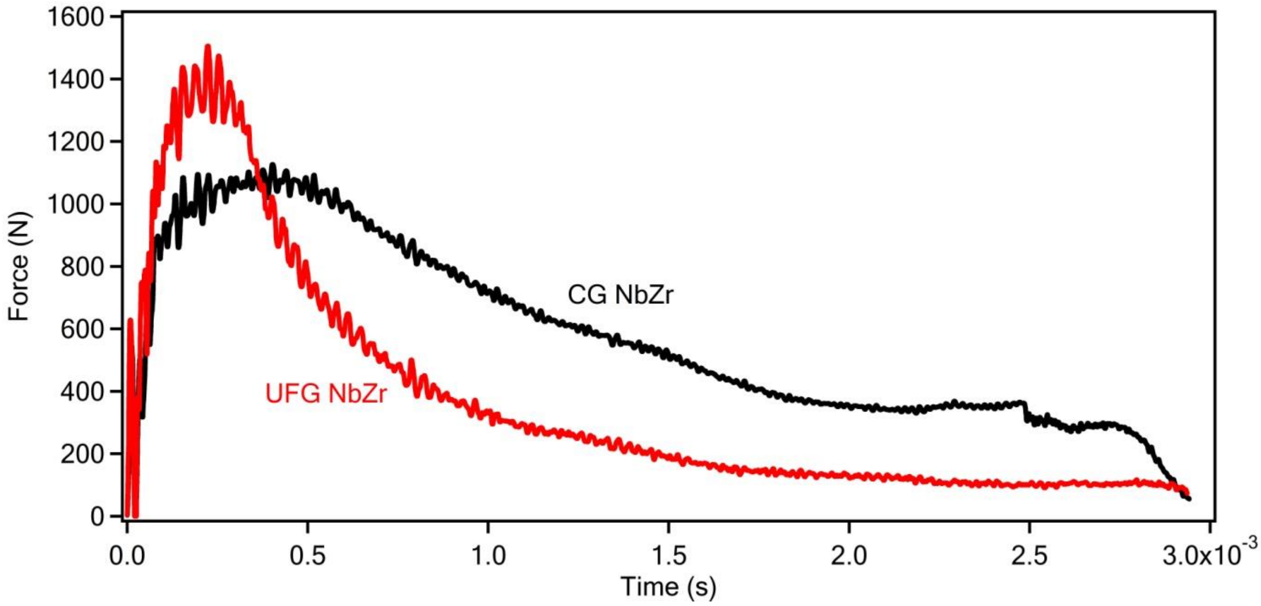

Figure 4. 4 Force vs. Time data for CG and UFG NbZr alloys [34].

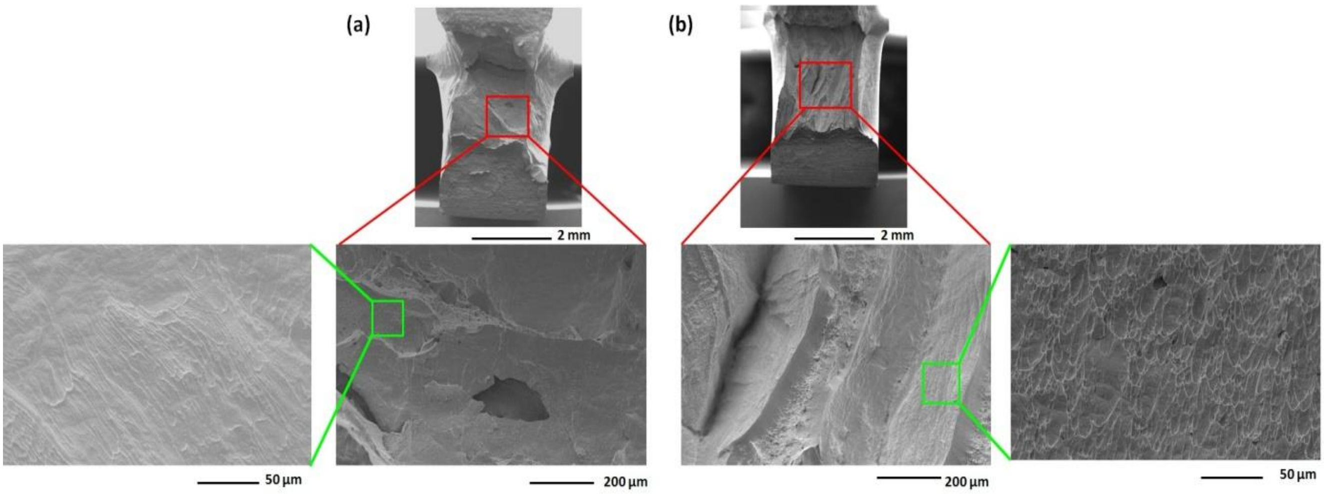

Figure 4. 5 Corresponding fracture surfaces of CG **(a)** and UFG **(b)** NbZr alloys after impact test with a temperature of 50 ^{0}C [34].

4.3 Modeling the Impact Response of NbZr

The material utilized in the current study exhibits excellent corrosion resistance and has good mechanical properties. It is considered as a promising material for dental and orthopedic applications. The modeling in the current work mainly consisted of two step FE impact simulations. In the first step, the impact response of the CG and UFG NbZr alloys was analyzed with FE simulations using the experimental tensile stress / strain data. In the second step, the impact responses of both NbZr variants were examined with the incorporation of microstructure into FE simulations utilizing a crystal plasticity code. It is noted that ANSYS ® 14.5 software and LS – DYNA ® solver were utilized for the FE simulations. The following subsection specifically discusses the two – step approach.

4.3.1 Finite Element Simulations of Experimental Impact Response

The major difficulty of FE impact simulations relies on the fact that forces are applied on the materials over a short time period [35, 36]. It is known that predicting large deformations within a short time period is more difficult than those of a longer time period. This is due to the nature of impact deformation such that there exists insufficient time period in order to stabilize displacements. However, impact loading considerably influences the materials' behavior in comparison with that under normal loading scenario [37]. To give an example, steel is ductile at medium strain rates whereas it becomes brittle when the strain rates are high. Such high deformations over short time period cause non – linearities in the material. These non – linearities are concerned with boundary condition, friction and contact surfaces. This leads to convergence problems and significant loss of time in the FE simulations [38].

The FE impact simulations were performed under the consideration of ANSYS ® 14.5 and LS- DYNA solver was utilized for the non – linear explicit dynamic analysis. The material plastic flow was represented with the multilinear isotropic hardening law. A fine mesh was selected with 8667 nodes and 6760 elements. The mesh type was " MultiZone" as the key property of this mesh is that small hex meshes are created on the geometry. By this way, simulation efficiency as well as simulation accuracy significantly increase. The element size was reduced to 0.1 mm in the notch region. The mesh quality was computed as 0.98 where 1.0 is the maximum value. The contact regions were considered to be frictional: the static friction coefficient was determined as 0.2 while the dynamic friction coefficient was chosen as 0.09 [38]. The boundary conditions were set as follows: A nodal displacement was applied from the top notch surface, the right/left sides and bottom surface consisted of fixed supports (Fig. 4.6). It should be noted that Cartesian coordinate frame was utilized for all dimensions and constraints.

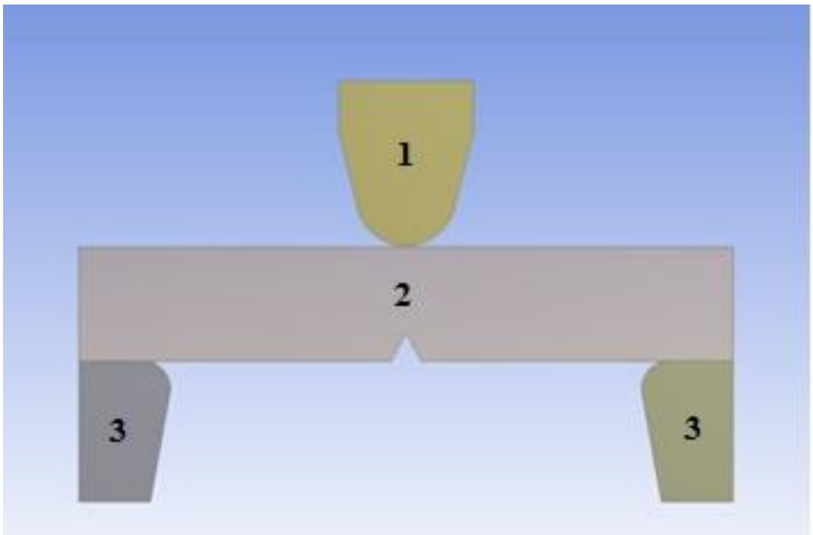

Figure 4. 6 FE simulation of experimental impact response (1 : impact hammer, 2 : impact sample , 3 : fixed supports).

The uniaxial experimental data (Figure 4.1) and experimental displacement vs. time data (Figure 4.7) were successfully implemented into the FE impact simulations for both NbZr variants in order to determine their impact response. The FE force vs. time output was compared with the experimental force vs. time data for both UFG and CG NbZr alloys (Figure 4.8). However, the FE impact simulations were performed up to the fracture point. This is due to the fact that the experimental displacement vs. time data belongs to the impact hammer. It was also assumed that the specimen does not displace after fracture point. However, a failure criterion has to be defined in order to predict further deformation of the specimen yet this is left for further studies.

The FE impact simulation and experimental force vs. time results significantly differ for both NbZr variants as evidenced in fig. 4.8. This indicates that the incorporation of experimental uniaxial test data (Figure 4.1) into the FE simulations is insufficient to determine the mechanical behavior under the action of impact loads. More simulations were conducted with finer meshes but variation in results was negligible.

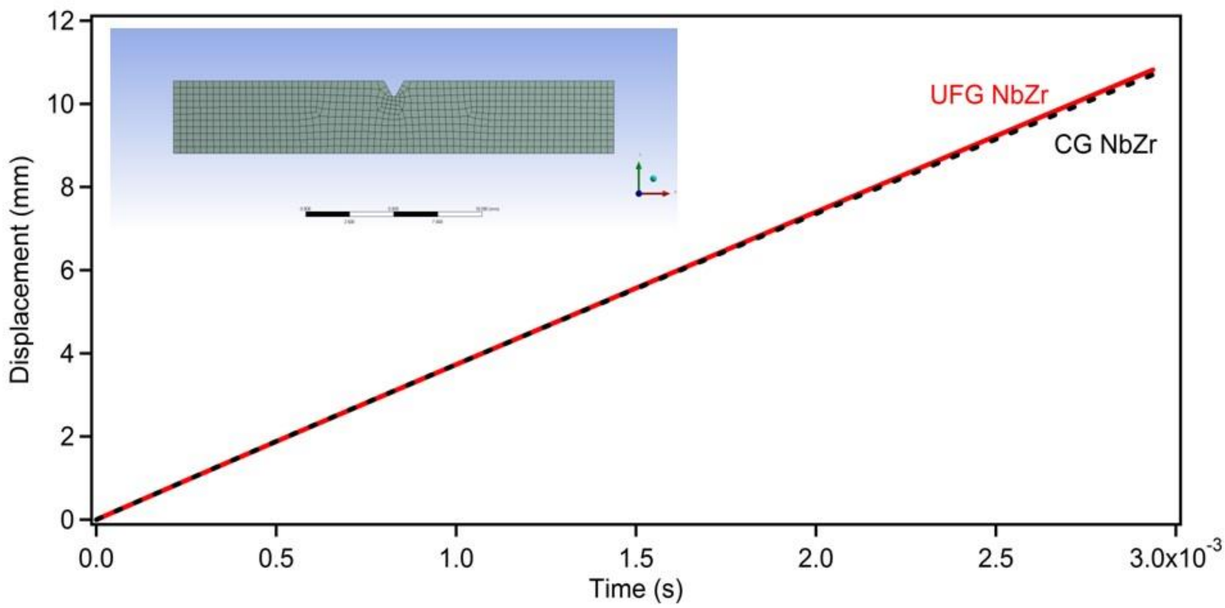

Figure 4. 7 The displacement vs. time plot used in FE impact simulations for UFG and CG NbZr alloys. The inset is the representation of the meshed impact geometry [34].

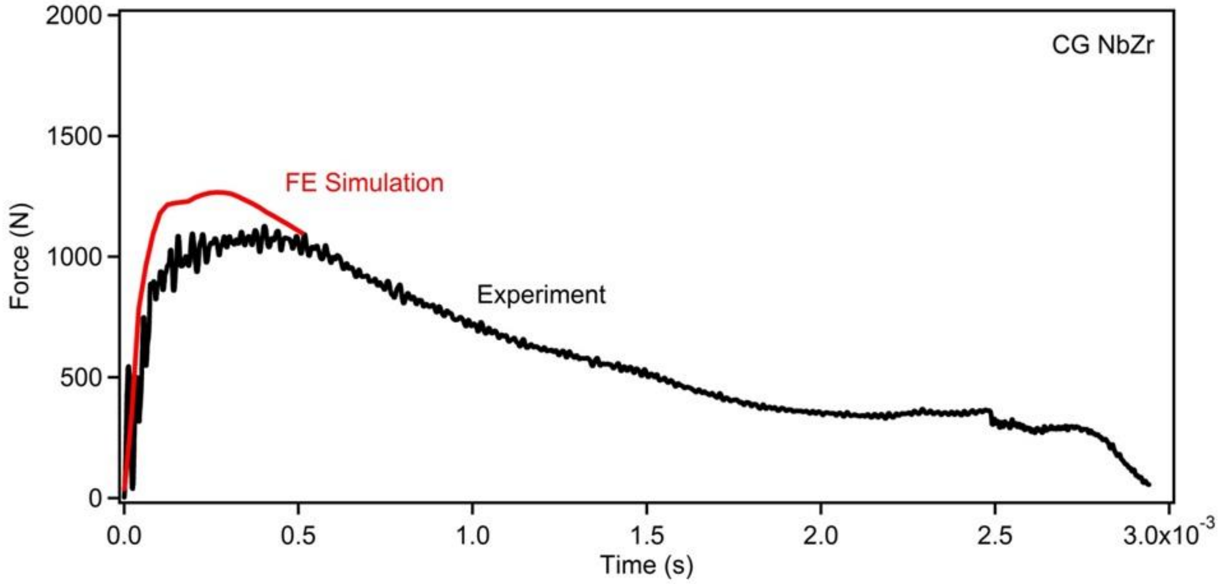

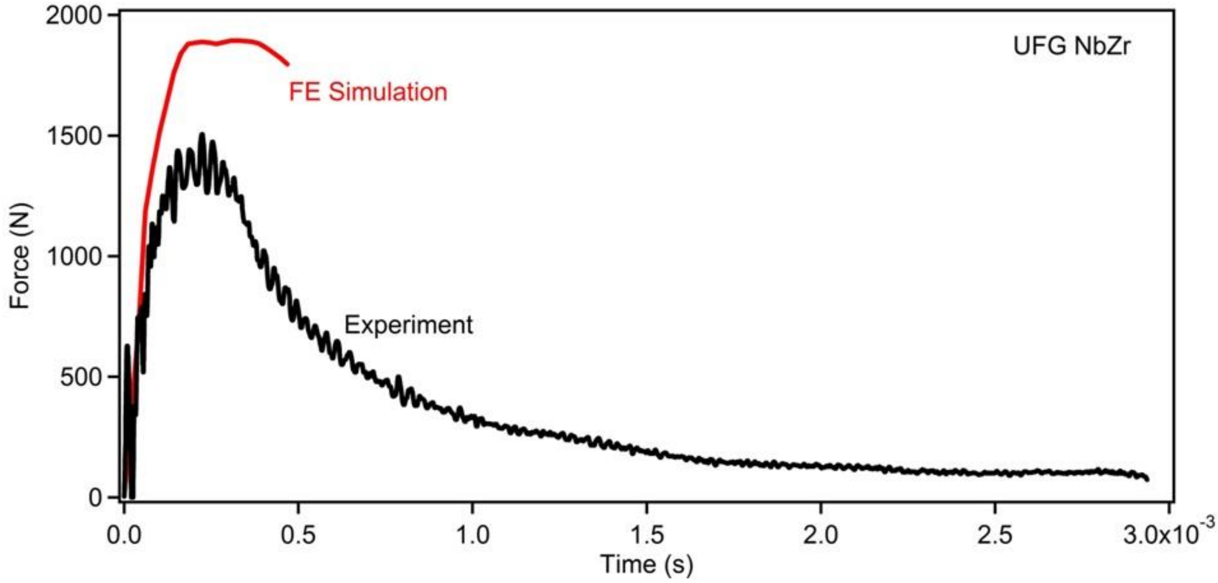

Figure 4. 8 The FE and experimental force vs. time comparison of NbZr variants after impact test [34].

The stress and strain fields of a material after a typical impact loading are demonstrated in fig. 4.9. A multiaxial stress state is observed around notch region. However, considerable differences are obvious when normal and equivalent stress distributions are compared (Figure 4.9). The aim of this analysis is to demonstrate the shortfall of the FE simulations to predict the multiaxial stress state utilizing uniaxial tensile deformation data. This approach may be suitable for materials exhibiting isotropy but it fails to be used in materials possessing high degree of anisotropy such as UFG NbZr [11 – 13]. However, mechanical behavior is predicted accurately under impact loading when microstructure and degree of anisotropy are both considered. Therefore, a new approach was presented by the authors to consider the microstructure. A crystal plasticity code called visco-plastic self-consistent (VPSC) was utilized to compute the equivalent stress/strain data for both UFG and CG NbZr. These data concerning the materials' plastic flow were successfully incorporated into the FE simulations. The approach presented herein is discussed in more detail in the following subsection.

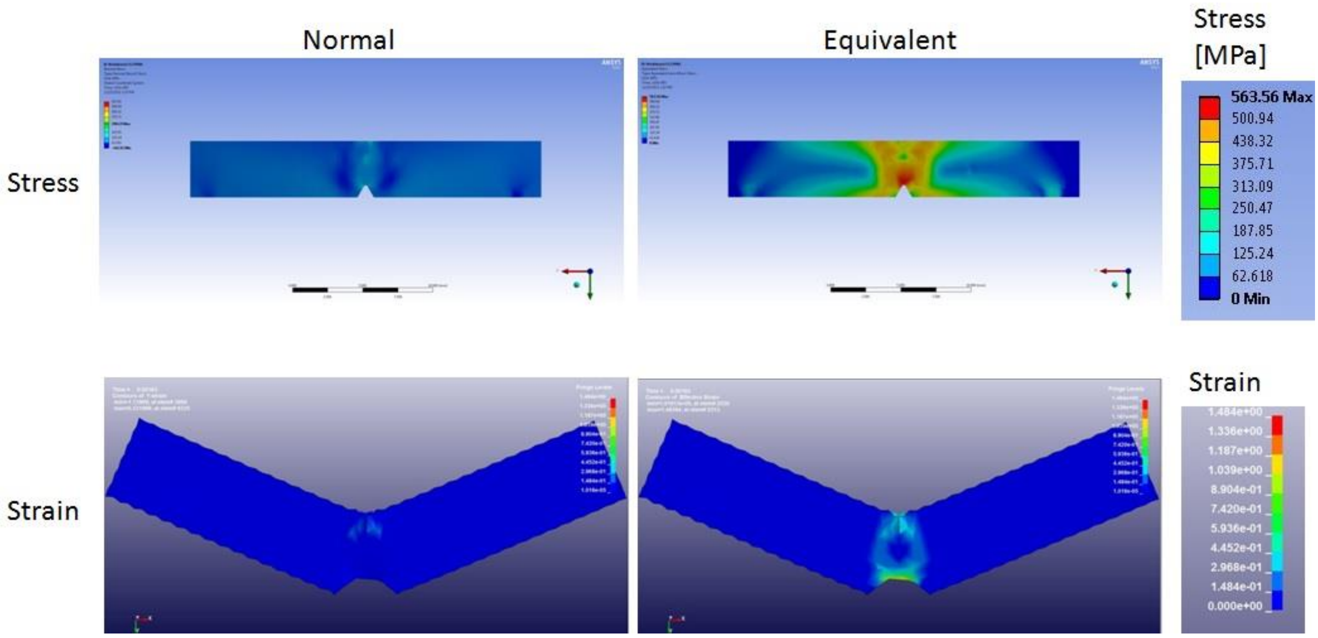

Figure 4. 9 The representation of typical normal and equivalent stresses / strains after impact loading [34].

4.3.2 Visco-plastic self-consistent modeling of the experimental deformation response

A crystal plasticity formulation called VPSC was utilized to incorporate texture and anisotropy effects into the FE simulations. Thereby, it is obvious to specify a flow rule for impact analysis regarding the equivalent deformation response instead of its uniaxial counterpart. Although such a flow rule can be obtained from the experimental techniques, crystal plasticity modeling can be a more effective approach. As the VPSC predicts the macroscopic deformation response, the power of this tool relies on predicting the deformation response at the microscale considering slip systems as well as slip - twin interactions [39]. In the light of accurate formulation, VPSC should perform well for the purpose of predicting the deformation behavior under various loading scenarios [40]. By this way, an approach is summarized as follows: Microscopic deformation response of NbZr alloy can be predicted under the consideration of experimental uniaxial deformation behavior. Specifically, equivalent deformation response is accurately determined as this leads to the appropriate material plastic flow rule required for the impact simulations.

The deformation behavior of NbZr variants under impact loading was predicted utilizing VPSC with the help of initial textures (Figure 4.10) as well as experimental uniaxial tensile deformation responses. The detail VPSC procedure was explained previously (Chapter 2).

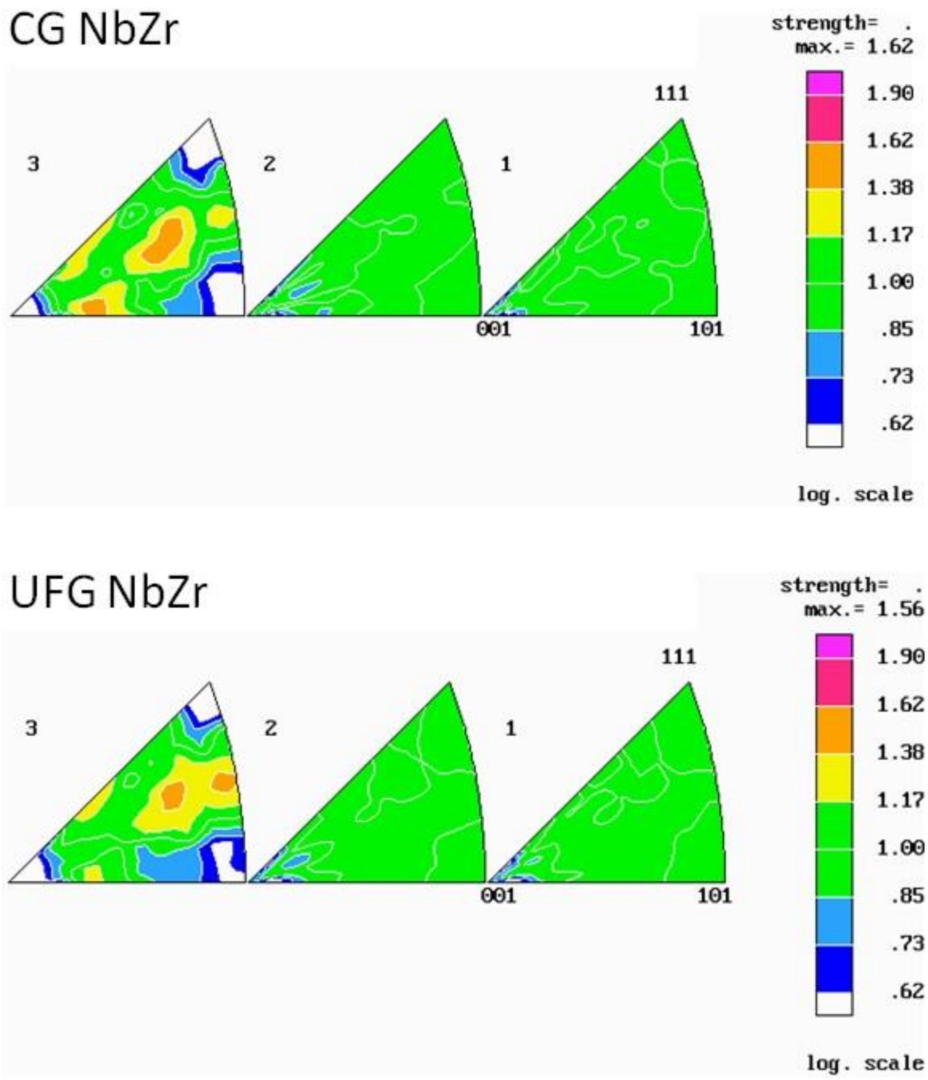

Figure 4. 10 The inverse pole figure representation of CG and UFG NbZr alloys [34]. Numbers 1, 2 and 3 demonstrate normal, transverse and extrusion directions, consecutively [11].

The initial textures of the CG and UFG NbZr alloys were used as an input while the macroscopic deformation behavior for both variants was obtained as an output for VPSC simulations (Figure 4.11).

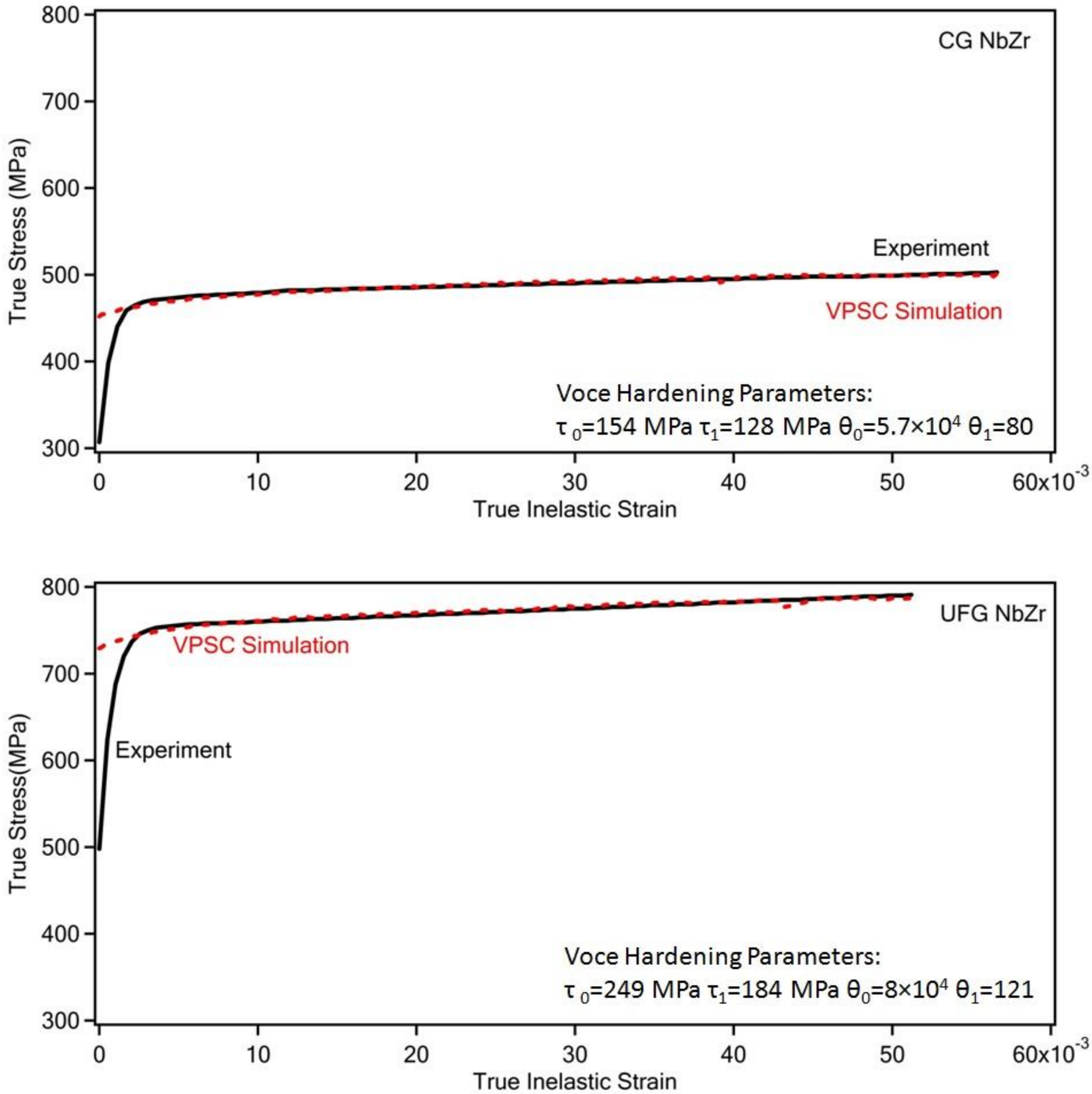

Figure 4. 11 VPSC modeling of the deformation for both UFG and CG NbZr alloys incorporating experimental uniaxial tensile data [34].

It should be mentioned at this point that the same experimental data (Figure 4.1) was used in order to model the micro deformation response of both NbZr variants. As VPSC models the plastic deformation, the true stress – true inelastic strain curves were plotted for the purpose of comparing the simulations and experiments. In order to model the deformation response for CG and UFG NbZr alloys, the plastic strain span was set to 5 - 6%. Nevertheless, The VPSC cannot model the deformations accurately beyond these plastic strain values as necking and failure occur simultaneously. It was observed that the initial simulation findings stand in good agreement with the experimental data. The notable difference between the simulations and the experiments is the stress levels before the onset of the plastic deformation. This is due to the dislocation – grain boundary interactions and grain boundary misorientation angle distribution. However, these microstructural features were not incorporated into the VPSC simulation as further work is required [39].

4.3.3. Incorporating the role of microstructure into the finite element model utilizing crystal plasticity

The powerful crystal modeling tool VPSC was utilized to determine the equivalent deformation response of CG and UFG NbZr alloys regarding the uniaxial stress – strain response in order to establish hardening rule for the impact simulations. In particular, it is demonstrated in Fig. 4.11 that the deformation behavior of the materials was modeled at the microstructural level. Therefore, the same VPSC model with same hardening parameters was performed in order to determine the equivalent deformation response of the CG and UFG NbZr. The stress - strain distribution (Figure 4.9) indicates the need of two key features that should be importantly considered during the impact simulations. These are specifically the flow rule due to the equivalent deformation response and the heterogeneous stress – strain distribution in the impact sample. The flow rule can be established utilizing VPSC modeling while the heterogeneous stress – strain distribution is concerned with the geometry.

In the light of our approach, three different zones were extracted from the FE mesh of the CG and UFG NbZr samples (Figure 4.12). In other words, three different zones imply three different flow rules. Thereby, the VPSC predicts the equivalent stress – strain states of each specific zone for both NbZr variants as illustrated in Fig. 4.13.

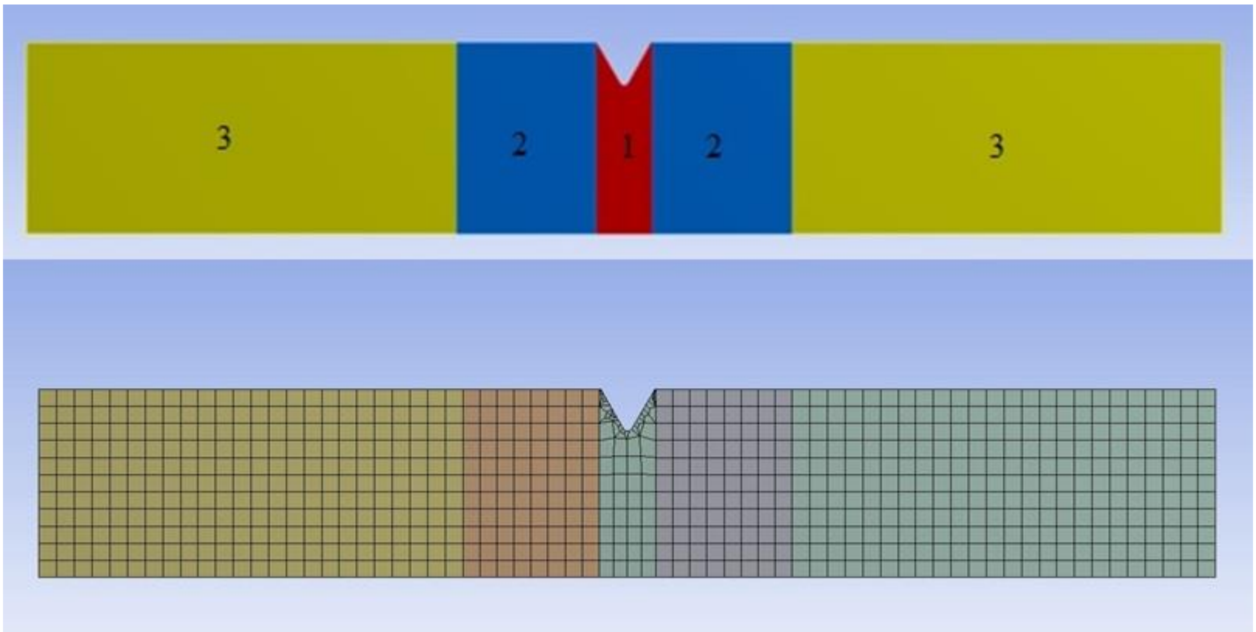

Figure 4. 12 The FE mesh division of the impact sample (upper image) and the corresponding mesh applied for the FE divided impact sample [34].

The hardening parameters utilized previously for the purpose of predicting the experimental uniaxial behavior, were also used in the simulations of these three zones. Specifically, variation in flow rule of these zones is dependent on the different velocity gradient tensors. The different strain distributions significantly influence the deformation behavior of the polycrystalline materials thus the velocity gradient tensors. These tensors for each zone are expressed as:

$$\dot{U}_1 = \begin{bmatrix} 4.2 & 1.0 & 0 \\ 1.0 & -2.1 & 0 \\ 0 & 0 & -2.1 \end{bmatrix}, \dot{U}_2 = \begin{bmatrix} 3.0 & 1.0 & 0 \\ 1.0 & -1.5 & 0 \\ 0 & 0 & -1.5 \end{bmatrix} \text{ and } \dot{U}_3 = \begin{bmatrix} 0.3 & 1 & 0 \\ 1 & -0.15 & 0 \\ 0 & 0 & -0.15 \end{bmatrix}$$

where $\dot{U}_1$ represents zone 1, $\dot{U}_2$ defines zone 2 and $\dot{U}_3$ denotes zone 3.

The VPSC simulation findings exhibit the equivalent deformation responses for each zone for both materials incorporating the velocity gradient tensors (Figure 4.13). These results correspond well with each other as the UFG NbZr possesses the higher strength. It is noted that zone 1 has the highest stress concentration in comparison with zone 2 and 3, while zone 3 has the lowest stress concentration (Figure 4.13). This is consistent with the findings in Fig. 4.9 as the highest stress levels are observed in zone 1 due to notch and lowest stress levels are present in zone 3 stemming from the smallest stress concentration factor. It should be mentioned that large strains were utilized in order to plot the equivalent stress – strain graphs (Figure 4.13) but small strains were considered for its uniaxial counterpart.

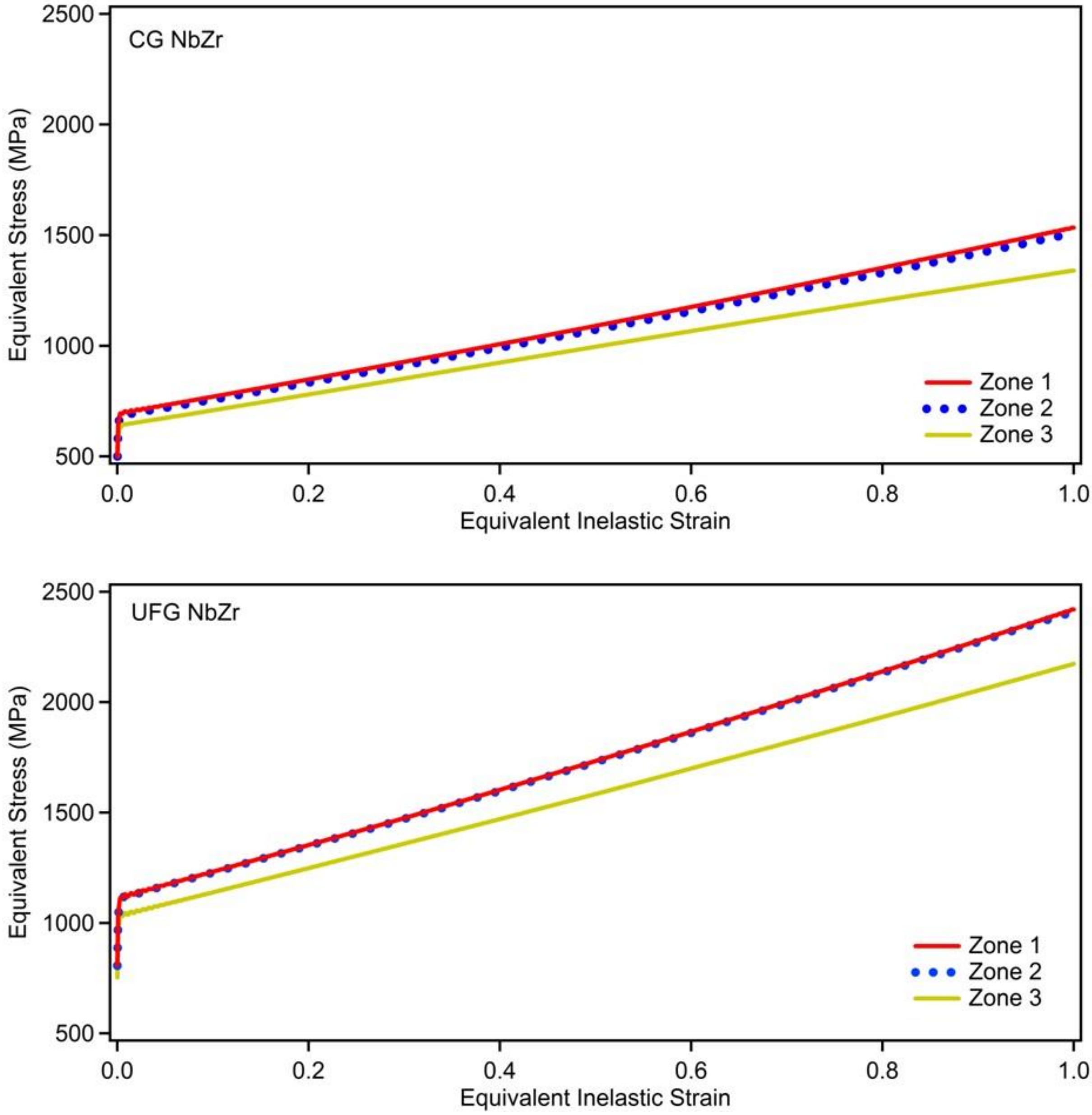

Figure 4. 13 Equivalent stress vs. equivalent strain response for each zone for CG and UFG NbZr materials [34].

In the case of experimental deformation behavior modeling, necking and failure mechanisms significantly limit reaching up to high strains. Furthermore, impact samples undergo larger strains as this is observed particularly in the zones 1 and 2 (Figure 4.8). In other words, flow rule regarding the equivalent deformation responses for each zone was established for large strains (Figure 4.13).

As the equivalent stress – strain responses of both materials obtained from VPSC utilizing flow rule and initial textures, the FE simulation results reveal important findings (Figure 4.13).

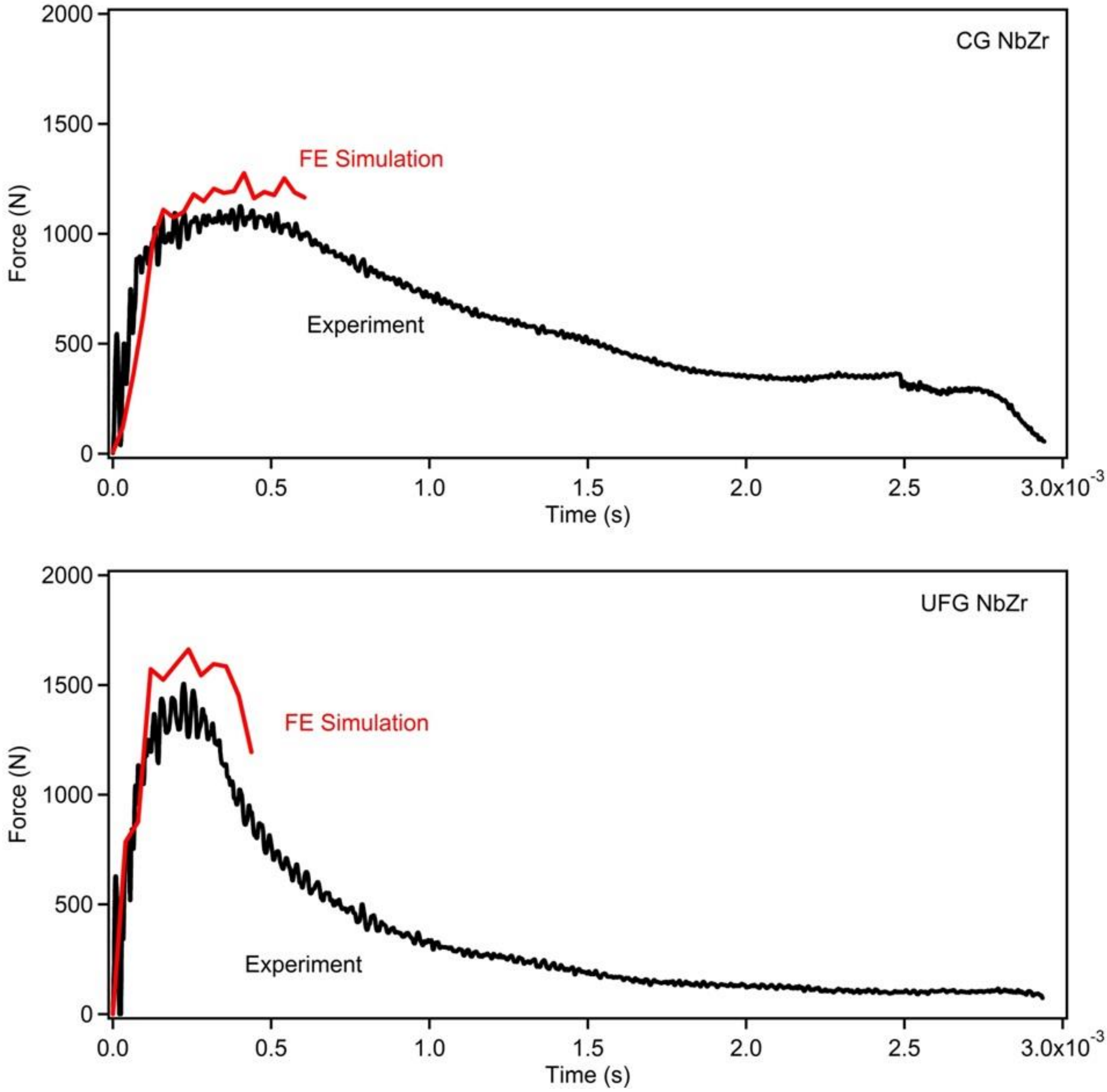

Figure 4. 14 Force vs. time comparison of FE simulations coupled with VPSC and experimental results for CG and UFG materials after impact test [34].

It is inferred from Fig. 4.14 that the approach presented by the authors can capture the force – time response under the action of impact loads for both NbZr variants. As new simulations in the light of current approach (Figure 4.14) are compared with the initial simulations incorporating experimental uniaxial deformation response (Figure 4.8), significant improvement is obvious in predicting the impact response. Specifically, this improvement in the case of UFG NbZr is more remarkable than that of its CG counterpart. It was evidenced previously that the texture of UFG NbZr plays a more dominant role on the deformation behavior as compared to that of CG NbZr [11 – 13]. This implies the more improvement in the UFG NbZr scenario while the initial textures are incorporated stemming from the success of the multi – scale modeling approach presented herein.

4.4 Discussion

Successful prediction of impact response relies on the detailed microstructure analysis as demonstrated by the current modeling approach. The multi – scale approach presented by the authors evidences the more accurate predictions (Figure 4.14) as compared to the typical FE analysis without considering the microstructural effects (Figure 4.8). This approach also sheds light on the need of determining multi – axial stress state in order to establish hardening rule of the materials.

It is admitted by the authors that further improvement should be made although the current approach is successful to predict the impact response of both NbZr variants under the consideration of different microstructures. In particular, the powerful crystal modeling tool VPSC plays a major role to predict the equivalent deformation response of the NbZr biomedical alloys considering the microstructural mechanisms for FE impact simulations. It is inferred from the inverse pole figures in Fig. 4.10 that the initial textures of UFG and CG NbZr are quite analogous. However, equivalent deformation responses obtained from the utility of VPSC (Fig. 4.13) regarding the experimental uniaxial stress – strain states (Fig. 4.1) demonstrate the different stress levels for CG and UFG microstructures.

The experimental initial texture is used as input in VPSC for the purpose of determining the orientation of each grain as this leads to activate deformation mechanisms at the micro – level [39 – 41]. It has been mentioned in the previous section that the grain boundary misorientation angle (GBMA) distribution is an important part of texture and it has a big impact on the deformation response of the materials, particularly for the UFG NbZr case [11 – 13, 26 – 28, 39, 42]. Consequently, in order to implement GBMA distribution effects into the VPSC simulations, an algorithm had been brought into focus such that a three – dimensional grain neighborhood were built concerning the experimental texture data [39, 42]. It has been observed that more reliable results were obtained in both NbZr materials in terms of predicting the impact response while the GBMA distribution is implemented into both microstructures. However, this approach was off – topic in the current work, instead establishment of multi – scale modeling approach has been brought into focus to predict the impact response of the NbZr alloy accurately. The implementation of the GBMA distribution into VPSC is left for further work as the success of the current approach is promising.

4.5 Conclusions

The current study was carried out for the purpose of establishing a multi – scale modeling approach implementing the anisotropy into implant design. With this motivation, the service life of implants can be increased with predicting or preventing mechanical failure at the design process. The influence of anisotropy on the impact response of NbZr material was investigated considering different microstructures of CG and UFG variants. Furthermore, the anisotropy effects were incorporated into impact analysis with the successful coupling of a crystal plasticity code VPSC and FE simulations. In particular, the VPSC model predicts the equivalent deformation responses of both CG and UFG NbZr materials concerning the experimental uniaxial stress – strain states as well as initial textures. The equivalent deformation responses were utilized to determine an appropriate flow rule for FE impact simulations considering microstructural evolution and geometric effects. The success of the current approach, specifically incorporation of the texture, anisotropy and flow rule relies on the close proximity with the predictions of experimental impact response of both NbZr variants. The major findings indicate that texture and anisotropy have considerable effects on the impact response. More importantly, a multi – scale modeling approach is in great demand in order to predict the impact response precisely. Consequently, the current approach sheds light on the design of NbZr based dental and orthopedic implants under the consideration of texture.

For a more detailed understanding of the role of microstructural features on the impact response of different materials including strain rate effects, the current approach was extended to strain-rate sensitive high manganese austenitic steels, which is detailed in the following chapter.

4.6 References

[1] T. Duerig, A. Pelton, D. Stöckel, An overview of nitinol medical applications, Materials Science and Engineering A 273 (1999) 149

[2] R.Z. Valiev, I.P. Semenova, E. Jakushina, V.V. Latysh, H. Rack, T.C. Lowe, J. Petruzelka, L. Dluhos, D. Hrusak, J. Sochova, Nanostructured SPD processed titanium for medical implants, Materials Science Forum 584 (2008) 49

[3] S.M. Toker, D. Canadinc, H.J. Maier, O. Birer, Evaluation of passive oxide layer formation – biocompatibility relationship in NiTi shape memory alloys, Materials Science and Engineering C 36 (2014) 118

[4] A.Y. Imam, B. Yilmaz, T.B. Özçelik, E. McGlumphy, Salvaging an angled implant abutment with damaged internal threads: a clinical report, The Journal of Prosthetic Dentistry 109 (2013) 287

[5] F. Zarrone, R. Sorrentino, T. Traini , D. Di Lorio, S. Caputi, Fracture resistance of implant supported screw- vs cement-retained porcelain fused to metal single crowns: SEM fractographic analysis, Dental Materials 23 (2007) 296

[6] C.H. Li, C.T. Chou, Bone sparing implant removal without terephine via internal separation of the titanium body with a carbide bur, International Journal of Oral and Maxillofacial Surgery 43 (2014) 248

[7] N.J. Hallab, S. Anderson, M. Caicedo, J.J. Jacobs, Zirconium and niobium affect human osteoblasts, fibroblasts, and lymphocytes in a similar manner to more traditional implant alloy metals, Journal ASTM International 3 (2006) JAI12817.

[8] H. Matsuno, A. Yokoyama, F.Watari, M. Uo, T. Kawasaki, Biocompatibility and osteogenesis of refractory metal implants, titanium, hafnium, niobium, tantalum and rhenium, Biomaterials 22 (2001) 1253

[9] H.G. Kim, S.Y. Park, M.H. Lee, Y.H. Jeong, S.D Kim, Corrosion and microstructural

characteristics of Zr–Nb alloys with different Nb contents, Journal of Nuclear Materials 373 (2008) 429

[10] F. Rubitschek, T. Niendorf, I.Karaman, H.J Maier, Corrosion fatigue behavior of a Biocompatible ultrafine-grained niobium alloy in simulated body fluid, Journal of the Mechanical Behavior of Biomedical Materials 5 (2012) 181

[11] T. Niendorf, D.Canadinc, H.J.Maier, I. Karaman, G.G. Yapici, Microstructure – mechanical property relationships in ultrafine-grained NbZr, Acta Materialia 55 (2007) 6596

[12] T. Niendorf, H.J. Maier, D. Canadinc, G.G.Yapici, I. Karaman, Improvement of the fatigue performance of ultrafine-grained Nb-Zr alloy by nano-sized precipitates formed by internal oxidation, Scripta Materialia 58 (2008) 571.

[13] S.M. Toker, F. Rubitschek, T. Niendorf, D. Canadinc, H.J. Maier, Anisotropy of ultrafine-grained alloys under impact loading: The case of biomedical niobium–zirconium, Scripta Materialia 66 (2012) 435.

[14] M. Cehreli, S.Sahin, K. Akca, Role of mechanical environment and implant design on bone tissue differentiation: current knowledge and future contexts, Journal of Dentistry 32 (2004) 123.

[15] C. Anunmanaa, K.J. Anusavicea, Jr. JJ. Mecholsky, Interfacial toughness of bilayer dental ceramics based on a short-bar, chevron-notch test, Dental Materials 26 (2010) 111.

[16] H.S. Gupta, P. Zioupos, Fracture of bone tissue: the „hows‟ and the „whys‟, Medical Engineering and Physics 30 (2008) 1209

[17] M. Moazen, A.C. Jones, Z. Jin, R.K. Wilcox, E.Tsiridis, Periprosthetic fracture fixation of the femur following total hip arthroplasty: a review of biomechanical testing, Clinical Biomechanics 26 (2011) 13

[18] P. Kannus, J. Parkkar, J. Poutala, Comparison of force attenuation properties of four different hip protectors under simulated falling conditions in the elderly: an in vitro

biomechanical study, Bone 25 (1999) 229

[19] Y. Fukuda, S. Takai, N.Yoshino, K. Murase, S.Tsutsumi, K. Ikeuchi, Y. Hirasawa Impact load transmission of the knee joint-influence of leg alignment and the role of meniscus and articular cartilage, Clinical Biomechanics 15 (2000) 516

[20] A. Verteramo, B.B. Seedhom, Effect of a single impact loading on the structure and mechanical properties of articular cartilage. Journal of Biomechanics 40 (2007) 3580

[21] N. Wakaoa, A. Harada, Y. Matsui, M. Takemura, H.Shimokata, M. Mizuno, M. Itod, Y. Matsuyamaa, N. Ishiguro, The effect of impact direction on the fracture load of osteoporotic proximal femurs, Medical Engineering and Physics 31 (2009) 1134

[22] T.P. Pinilla, K.C. Boardma, M.L. Bouxsein, E.R. Myers, W.C. Hayes, Impact direction from a fall influences the failure load of the proximal femur as much as age-related bone loss, Calcified Tissue International 58 (1996) 231

[23] Jr. J.W. Morris, Stronger, tougher steels, Science 320 (2008) 1022

[24] R. Song, D. Ponge, D. Raabe, Mechanical properties of an ultrafine grained C–Mn Steel processed by warm deformation and annealing, Acta Materialia 53 (2005) 4881

[25] Y. Kimura, T. Inoue, F. Yin, K. Tsuzaki, Inverse temperature dependence of toughness in an ultrafine grain-structure steel, Science 320 (2008) 1057

[26] P. Gabor, D. Canadinc, H.J. Maier, R.J. Hellmig, Z. Zuberova, J. Estrin, The influence of zirconium on the low-cycle fatigue response of ultrafine-grained copper, Metallurgical and Materials Transactions A 38 (2007) 1916

[27] D. Canadinc, H.J. Maier, M. Haouaoui, I. Karaman, On the cyclic stability of nanocrystalline copper obtained by powder consolidation at room temperature, Scripta Materialia 58 (2008) 307

[28] T. Niendorf, D.Canadinc, H.J. Maier, I. Karaman, S.G. Sutter, On the fatigue behavior of ultrafine-grained IF steel, International Journal of Materials Research 97 (2006) 1328

[29] E.M. Viatkina, W.A.M. Brekelmans, M.G.D. Geers, The role of plastic slip anisotropy in the modelling of strain path change effects, Journal of Materials Processing Technology 209 (2009) 186.

[30] I.J. Beyerlein, L.S. Tóth, Texture evolution in equal-channel angular extrusion, Progress in Materials Science 54 (2009) 427

[31] M.R. Bache, W.J. Evans, Impact of texture on mechanical properties in an advanced titanium alloy, Materials Science and Engineering A 319 (2001) 409

[32] B.B. Martin, D.B. Burr, N.A. Sharkey, Skeletal Tissue Mechanics, Springer, Verlag, NY, 1998

[33] J.Y. Rho, L. Kuhn-Spearing, P. Zioupos, Mechanical properties and the hierarchical structure of bone, Medical Engineering and Physics 20 (1998) 92

[34] O.Onal, B.Bal, S.M.Toker, M.Mirzajanzadeh, D.Canadinc, H.J.Maier, Microstructure – based Modeling of the Impact Response of a Biomedical Niobium – Zirconium Alloy, Journal of Materials Research 29 (2014) 1123

[35] K. Kormi, D.C. Webb, W. Johnson, The application of the FEM to determine the response of a pretorsioned pipe cluster to static or dynamic axial impact loading, Computers and Structures 62 (1997) 353

[36] S.L. Raykhere, P. Kumar, R.K. Singh, V. Parameswaran, Dynamic shear strength of adhesive joints made of metallic and composite adherents, Materials and Design 31 (2010) 2102

[37] W. Goldsmith, Impact: the theory and physical behavior of colliding solids, Toronto, Dover, 2001.

[38] Z.Q. Feng, C. Vallee, D. Fortune, F. Peyraut, The 3e hyperelastic model applied to the modeling of 3D impact problems, Finite Elements in Analysis and Design 43 (2006) 51

[39] D. Canadinc, E. Biyikli, T. Niendorf, H.J. Maier, Experimental and numerical investigation of the role of grain boundary misorientation angle on the dislocation–grain boundary interactions, Advanced Engineering Materials 13 (2011) 281

[40] D. Canadinc, H. Sehitoglu, H.J. Maier, P. Kurath, On the incorporation of length scales associated with pearlitic and bainitic microstructures into a visco-plastic self-consistent model, Materials Science and Engineering A 485 (2008) 258

[41] R.A. Lebensohn, C.N. Tomé, A self-consistent anisotropic approach for the simulation of plastic deformation and texture development of polycrystals: Application to zirconium alloys, Acta Metallurgica et Materialia 41 (1993) 2611

[42] E. Biyikli, D.Canadinc, H.J. Maier, T. Niendorf, S.Top, Three-dimensional modeling of the grain boundary misorientation angle distribution based on two-dimensional experimental texture measurements, Materials Science and Engineering A 527 (2010) 5604

CHAPTER 5: APPLICATION OF MULTI-SCALE MODELING TO OTHER PROBLEMS: THE IMPACT RESPONSE OF A STRAIN RATE SENSITIVE HIGH-MANGANESE AUSTENITIC STEEL

5.1 Introduction

Austenitic high-manganese (Mn) steels, a class of high strength steels, have received considerable attention since they offer a rare combination of exceptional work hardening capacity, high wear and abrasion resistance, high strength and significant ductility [1-3]. These extraordinary mechanical properties have been subject to several studies [3-9], many of which revealed that the main mechanism underlying the observed mechanical behavior is the presence of twins in the microstructure accompanied by additional microstructural features, such as stacking faults, dynamic strain aging (DSA) and interaction of twins with dislocations [6-9]. Simultaneous activity of all of the aforementioned micro-deformation mechanisms result in the improved strength and work hardening capacity of this class of steels, where all these mechanisms constitute obstacles against gliding dislocations [6-9]. However, the complexity of the deformation behavior of these materials makes it difficult to clearly distinguish between the relative contributions of the hardening mechanisms.

A very good example to this complicated microstructure is that of Hadfield steel, a high-Mn austenitic steel with a face-centered cubic (fcc) structure at room temperature. Hadfield steel is well known for its deformation by both slip and twinning [6, 10], where the two mechanisms interact and further promote work hardening concomitant with increasing strain. To add further to the complexity of micro-deformation mechanisms, glide dislocations tend to form high-density dislocation walls (HDDWs), which effectively hinder active glide dislocations from moving further, contributing to the unusual strain hardening exhibited by this material [11, 12]. However, dislocations are prevented from gliding not by twin boundaries or HDDWs only, but also by carbon (C), which can diffuse within the matrix throughout the deformation, as it becomes easily excited by the energy provided by the applied stresses [13].

The excited C atoms diffuse within the matrix, however; when they meet dislocations at interstitial zones, they prevent dislocations from gliding further, which is referred to as pinning of the dislocation by the C atom [1, 13]. This, indeed, gives way to DSA [1, 13], which further adds to the complexity of the microstructure by promoting strain rate sensitivity (SRS) and negative strain rate sensitivity (NSRS) [13]. Specifically, as steel is deformed at a faster rate, the rate of generation of forest dislocations increases, as well, leading to an increased level of stress at the same strain value, which is known as the SRS [13].In Hadfield steel, however; the diffusion velocity of C also increases concomitant with strain rate. At lower strain rates, the C atoms stay longer at an interstitial site, potentially pinning a dislocation for a longer period, which is a positive contribution in terms of strain hardening. However, as the deformation rate increases, C atoms start to diffuse much faster, and they cannot pin dislocations for extended periods, which indeed takes away an important contribution to the overall hardening: the result is softening, and even though the strain rate increases, the material attains lower levels of stress at the same strains, which is known as the NSRS [13]. The NSRS, however; is eliminated at very high strain rates, such that the missing contribution to the overall hardening due to the pinning of dislocations becomes negligible as compared to the significant forest hardening, which constitutes the major mechanism of hardening at elevated rates of deformation [13].

Despite their complicated micro-deformation mechanisms, other high-Mn austenitic steels with similar microstructures, such as the twinning-induced plasticity (TWIP) steels, continue to attract attention and find use in applications, mainly owing to their superior mechanical properties [9, 14-16]. Automotive industry and other load bearing applications utilize high-Mn steels at an increasing rate, and ballistic applications constitute another potential area that may utilize this class of steels. For all these applications, however; resistance to impact loading and understanding the deformation response under impact becomes of utmost importance [10]. Considering the design process of any commercial product, on the other hand, one realizes that the capability to realistically predict the impact response of these alloys by numerical modeling is warranted, which constitutes the motivation of the current work.

The impact performance of a material is governed by its microstructure, and the corresponding parameters, such as grain boundaries, grain size, precipitates and delaminations, and the material's ductile-to-brittle transition temperature (DBTT) altogether dictate the response to impact loading [17-20]. Another important parameter affecting the impact response is the texture of the material, which defines the grain boundary – dislocation interactions, and thus, the crack propagation behavior under impact loading, as well as the degree of anisotropy, which dictates the relative slip activity in each grain [17], warranting incorporation of anisotropy effects into the design process.

The current study was undertaken with the motivation of addressing this issue, such that a combined experimental and numerical approach is proposed to predict the impact response of high-Mn austenitic steels in a realistic manner. For this purpose, uniaxial tensile deformation and impact responses of Hadfield steel were experimentally monitored, where the uniaxial deformation experiments featured four different strain rates ranging from moderate to high in order to also assess the role of NSRS exhibited by this material. Finite element (FE) simulations of the impact experiments were carried out, where the roles of texture, geometry and strain rate sensitivity were successfully taken into account all at once by incorporating the proper multi-axial material flow rule obtained from crystal plasticity simulations into the FE analysis. Specifically, crystal plasticity was utilized to obtain the multi-axial flow rule at different strain rates based on the experimental deformation response under uniaxial tensile loading, and the equivalent stress – equivalent strain response was then incorporated into the FE model for the sake of a more representative hardening rule under impact loading. The current results demonstrate that reliable predictions can be obtained by proper coupling of crystal plasticity and FE analysis even if the experimental flow rule of the material is acquired under uniaxial loading and at moderate strain rates that are significantly slower than those attained during impact loading. Overall, the approach presented herein constitutes an important guideline for the design process of impact bearing applications utilizing high-Mn austenitic steels.

5.2 Materials and Methods

The material investigated in this study is Hadfield steel, an high-Mn austenitic steel with a fcc structure, and has a chemical composition of 12.44 wt% Mn, 1.10 wt% C and balance iron. Small-scale dog-bone shaped tension samples were extracted from railroad frogs taken from service with the aid of electro-discharge machining to avoid any process-induced residual stresses and strains on the samples. The room temperature (RT) monotonic tensile deformation experiments were carried out on a servo-hydraulic test frame equipped with a digital controller and a miniature extensometer of 3 mm gauge length. The results revealed a significant SRS prevalent in Hadfield steel polycrystals within the strain rate range of 1×10^{-4} 1/s to 1×10^{-1} 1/s (Figure 5.1). A serrated flow was exhibited by the material at all strain rates, however; the associated instability was much more prominent at 1×10^{-3} 1/s, where NSRS was prevalent as evidenced by the lower stress levels attained despite the ten-fold increase in the strain rate from 1×10^{-4} 1/s to 1×10^{-3} 1/s.

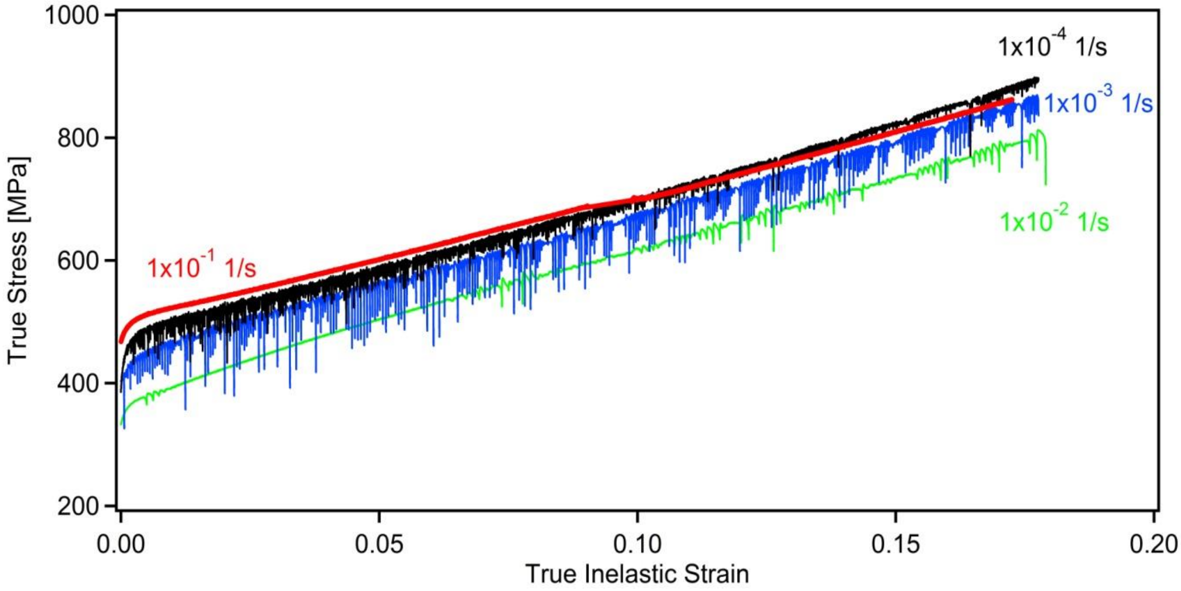

Figure 5. 1 RT uniaxial tensile deformation response of Hadfield steel obtained at different strain rates, demonstrating the NSRS. Data was recompiled from [13].

The impact samples were extracted from both the same Hadfield railroad frog with dimensions of 2.8 mm × 25 mm × 4 mm, featuring a 60˚ notch with a radius of 0.1 mm and a depth of 1 mm [17]. The specimens were mechanically polished down to a 4000 grit size in order to minimize the detrimental effects of machined surfaces on the impact response. The impact experiments were conducted at RT, and the specimens were subjected to deformation with an impact energy of 50 J and at a velocity of 3.8 m/s, where 8000 data points were collected during each experiment with a data acquisition frequency of 2 MHz. For both uniaxial deformation and impact experiments, three companion samples were tested in each case in order to ensure repeatability. The initial textures of the samples prior to deformation were determined by X-ray diffraction.

5.3 Results and Discussion

5.3.1 Finite Element Simulations of Experimental Impact Response of Hadfield Steel

It is well known that very large deformations taking place within very short time periods constitute the major difficulty of FE simulations of impact loading [17, 21, 22]. Specifically, the available time period is insufficient for the stabilization of the computed displacements in the case of impact loading, such that the material's behavior significantly deviates under this dynamic type of loading from that under normal conditions owing to the nonlinear behavior under dynamic loading [17]. The current FE simulations of the impact behavior were carried out utilizing the ANSYS® 15 commercial software and the FE analysis was based on an explicit dynamics system, where the LS-DYNA® solver was employed in computations for the sake of a reliable nonlinear dynamic analysis.

The Lagrangian formulation and multilinear isotropic hardening were chosen to represent the nonlinearity and the plastic flow, respectively. A fine "MultiZone" mesh was constructed with 13530 nodes and 11060 quadrilateral elements, where the geometry was automatically decomposed into a hex mesh, increasing both the accuracy and computational efficiency of the simulations. The notch region was meshed with an element size of 0.1 mm, and the mesh had an orthogonal quality of 0.98 (out of 1.0). All contact regions of the impact sample were assumed to be frictional, and the corresponding static and dynamic friction coefficients were set to 0.2 and 0.09, respectively [17]. As for the boundary conditions, a nodal displacement was imposed on the top notch surface and fixed supports were placed at the right/left sides and on the bottom surface. Beyond the fracture point of the specimens, i.e. where the sample – hammer contact terminates, the equivalent plastic strain (EPS) criterion was utilized to define failure of the material, namely an EPS of 0.68 was preset as the failure initiation point. The Cartesian coordinate system was considered while designating the dimensions and constraints.

The first set of simulations made use of the experimental RT uniaxial tensile deformation response of Hadfield steel obtained at a strain rate of 1×10^{-4} 1/s to define the multilinear isotropic hardening rule (Figure 5.2). This strain rate is rather a moderate strain rate typically utilized in laboratory experiments employed to characterize the material's deformation response [17]. It is evident that the corresponding simulation result significantly differs from the experimentally measured impact behavior, indicating that the flow rule of the material should be based on experiments featuring much higher strain rates as the impact deformation itself takes place very rapidly. Thus, in order to assess the role of strain rate, FE simulations considering higher rates of deformation, namely 1×10^{-1} 1/s, 1×10^{-2} 1/s and 1×10^{-3} 1/s, were carried out (Figure 5.3). As expected, a comparison of experimental and simulated impact responses (based on four different strain rates) expressed in terms of force-time data (Figures 5.2 and 5.3) indicates the best predictions are made when the flow rule is based on the experimental deformation response obtained at the strain rate of 1×10^{-3} 1/s. A further look at the results presented in Figures 2 and 3 reveal a more interesting fact: the second best prediction is obtained when the flow rule is defined based on the uniaxial tensile deformation response obtained at a strain rate of 1×10^{-4} 1/s. This implies that the experimental data obtained within the NSRS range should not be utilized to define the hardening rule when constructing a FE model to predict impact response, regardless of the strain rate.

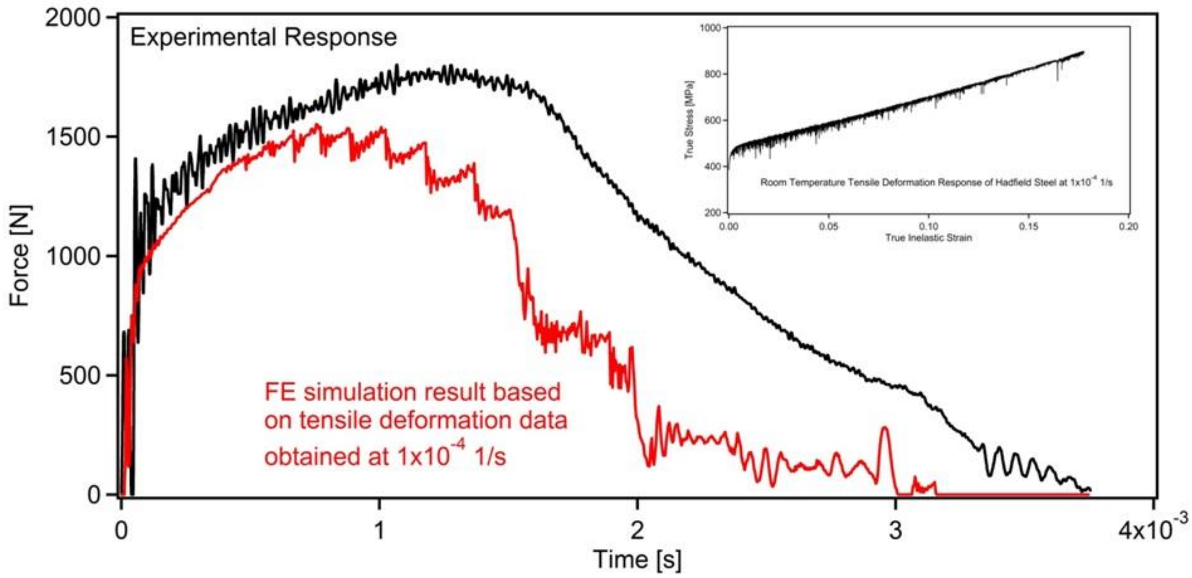

Figure 5. 2 The RT experimental impact response of Hadfield steel and the corresponding FE simulation result, where the flow rule was defined based on the experimental uniaxial tensile deformation response obtained at a strain rate of 1×10^{-4} 1/s [23].

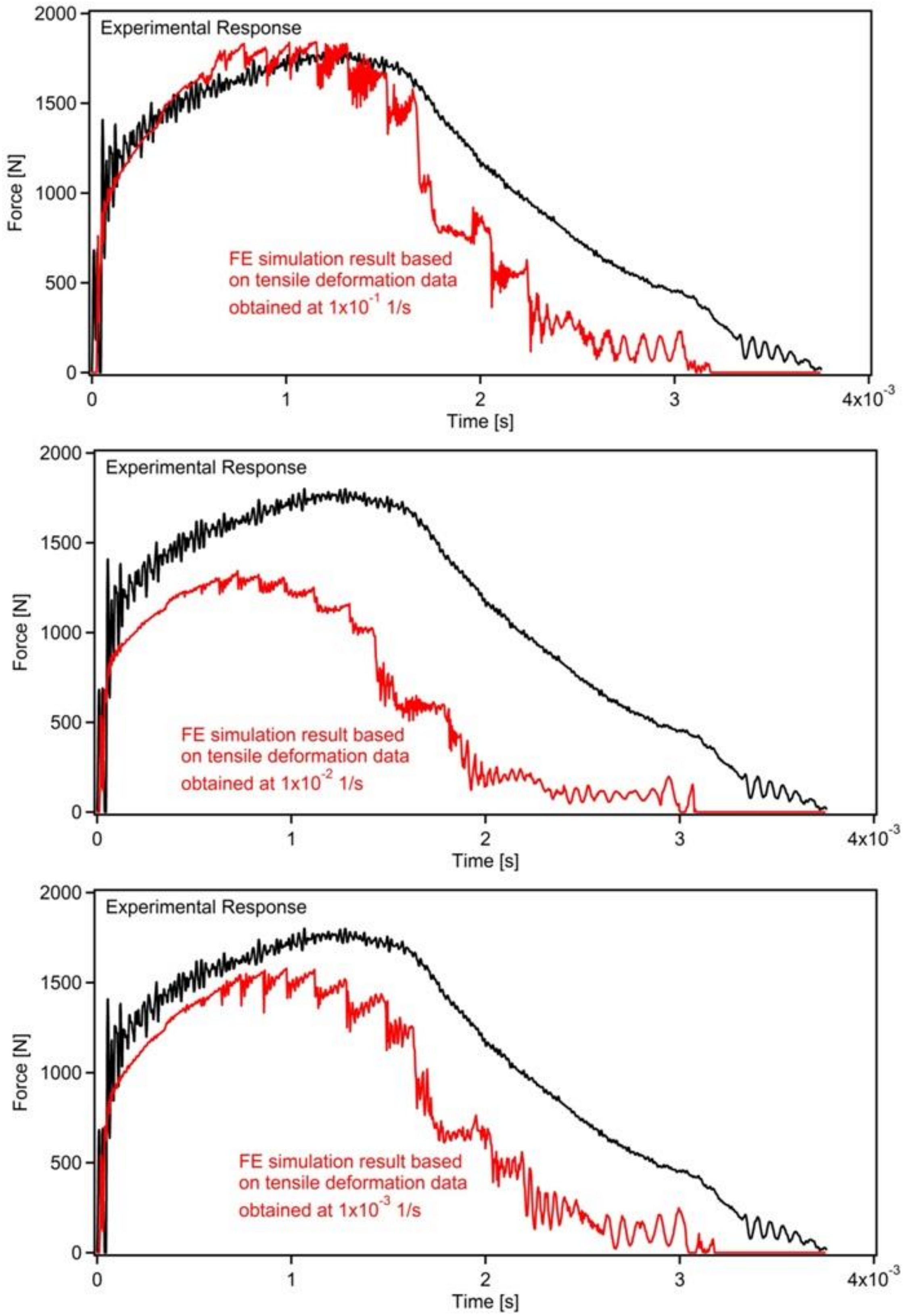

Figure 5. 3 A comparison of the RT experimental impact response of Hadfield steel and the corresponding FE simulation results, where the flow rule was defined based on the

experimental uniaxial tensile deformation responses obtained at strain rates of 1×10^{-1} 1/s, 1×10^{-2} 1/s and 1×10^{-3} 1/s [23].

Overall, all of the FE simulation results presented in Figures 5.2 and 5.3 exhibited noticeable deviation from the experimental impact response, implying that the provided hardening response based on the experimental uniaxial tensile deformation data was not sufficiently representative of the material's mechanical behavior under impact loading at any of the considered strain rates. Further simulations featuring a finer mesh were also carried out in order to question the numerical procedure, however; the same deviation from the experimental results persisted.

It has recently been demonstrated that a multiaxial stress-strain state is present in the critical region of the sample [17], and a comparison of normal and von Mises stress distributions reveals that employment of the uniaxial tensile deformation data as the input defining the material's flow rule under impact loading is not appropriate (Figure 5.4). Even though this approach might be appropriate for an isotropic material, it falls far from being realistic for a textured material exhibiting a significant degree of anisotropy [17]. The numerical analyses carried out until this point (Figures 5.2-5.4) clearly demonstrate the need for a proper representation of microstructure under impact loading, in addition to the strain rate effects.

5.3.2 Incorporation of the Role of Microstructure into the Finite Element Simulations through Crystal Plasticity

In order to utilize a proper flow rule to define hardening of Hadfield steel during impact, and account for the role of texture and the corresponding anisotropy – in addition to the strain rate effects – in the current FE simulations, a crystal plasticity approach was adopted. Specifically, based on the aforementioned analysis of stress-strain distributions upon impact loading (Figure 5.4), a flow rule based on equivalent stress-strain response was defined. In order to do so, a visco-plastic self-consistent (VPSC) algorithm was utilized to predict the von Mises stress-strain behavior of the material based on the experimental uniaxial tensile deformation data. Even though an alternative way of establishing the equivalent stress-strain response would have been carrying out multiaxial deformation experiments, the current methodology is much more efficient due to the impractical multiaxial experiments, especially in the case of high strain rates.

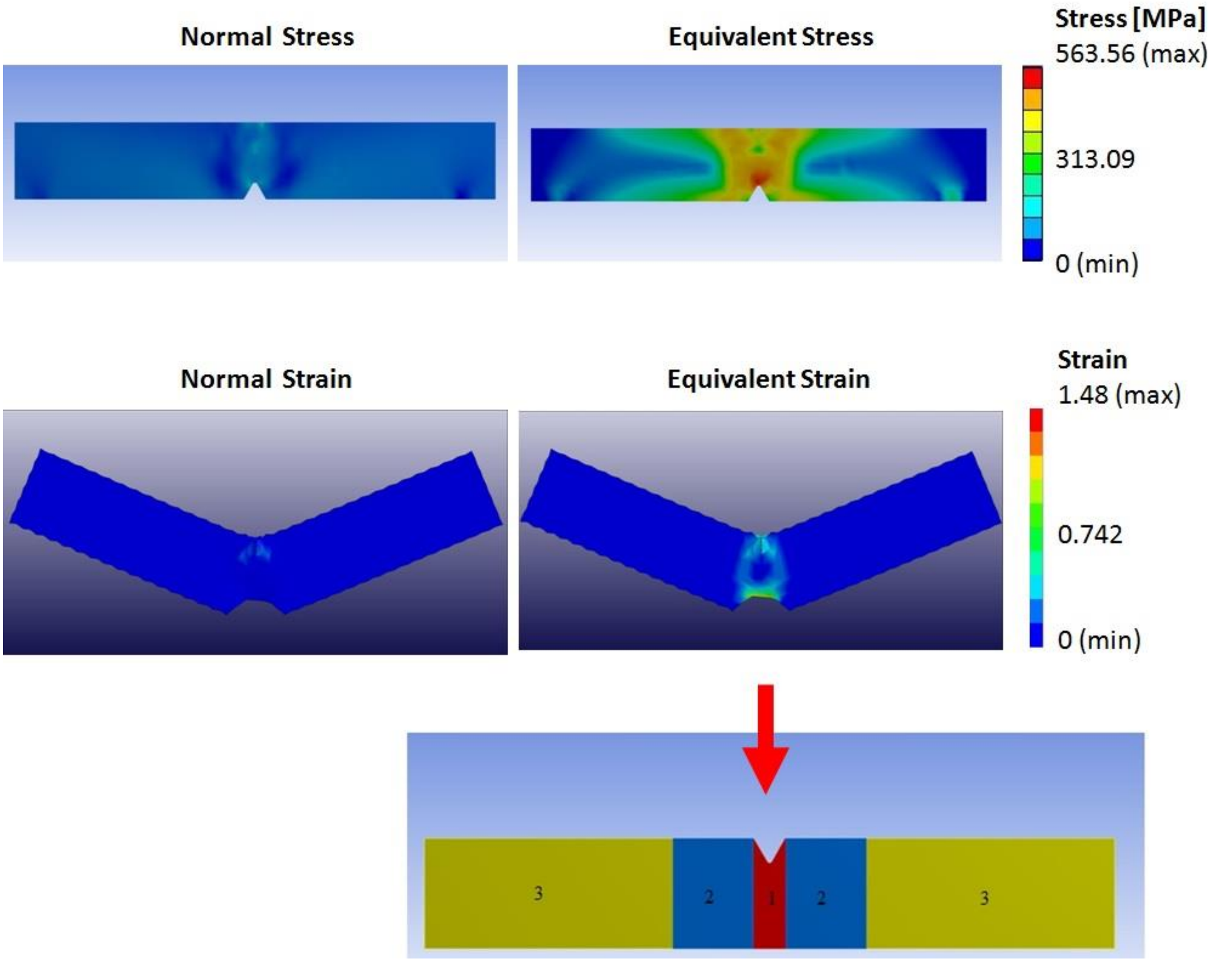

Figure 5. 4 A material-independent FE simulation of impact loading demonstrating the typical distribution of normal and equivalent stress-strain fields (above the arrow), and the corresponding division of sample geometry based on stress intensities within the sample [17, 23].

A successful crystal plasticity model should both predict the macroscopic deformation response and capture the deformation characteristics at the slip system level [24], such that the deformation response could be predicted under any type of loading [25]. With this motivation, the deformation of Hadfield steel was modeled at the microscopic level for each strain rate considered herein based on the corresponding experimentally obtained uniaxial deformation response (Figures 5.5-5.8). The VPSC model utilizes the initial texture of the material as an input, such that the loads on each grain, and thereby the slip activities in each grain, are dictated by the texture of the material [26-28]. Thereafter, the same micro level model established for each strain rate was utilized to predict the corresponding equivalent stress-strain response (Figure 5.5-5.8), which can be utilized as a proper flow rule for the impact simulations, as discussed before.

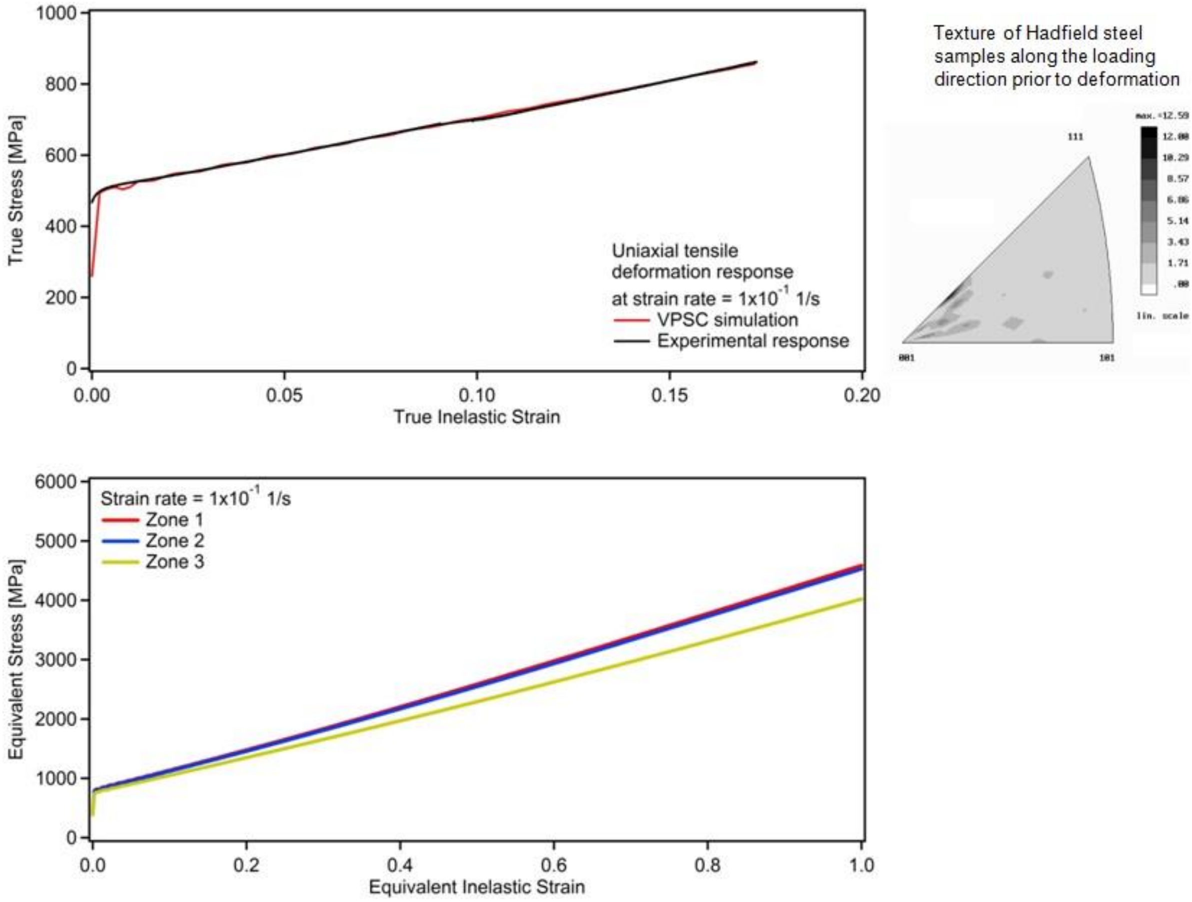

Figure 5. 5 Top: VPSC simulation of the RT experimental uniaxial tensile deformation of Hadfield steel at a strain rate of 1×10^{-1} 1/s, and the corresponding initial texture along the loading direction (representative of the texture of all companion samples). Bottom: the corresponding predicted equivalent stress-strain response for each zone within the impact sample based on the distribution of stress concentration (Figure 5.4) [23].

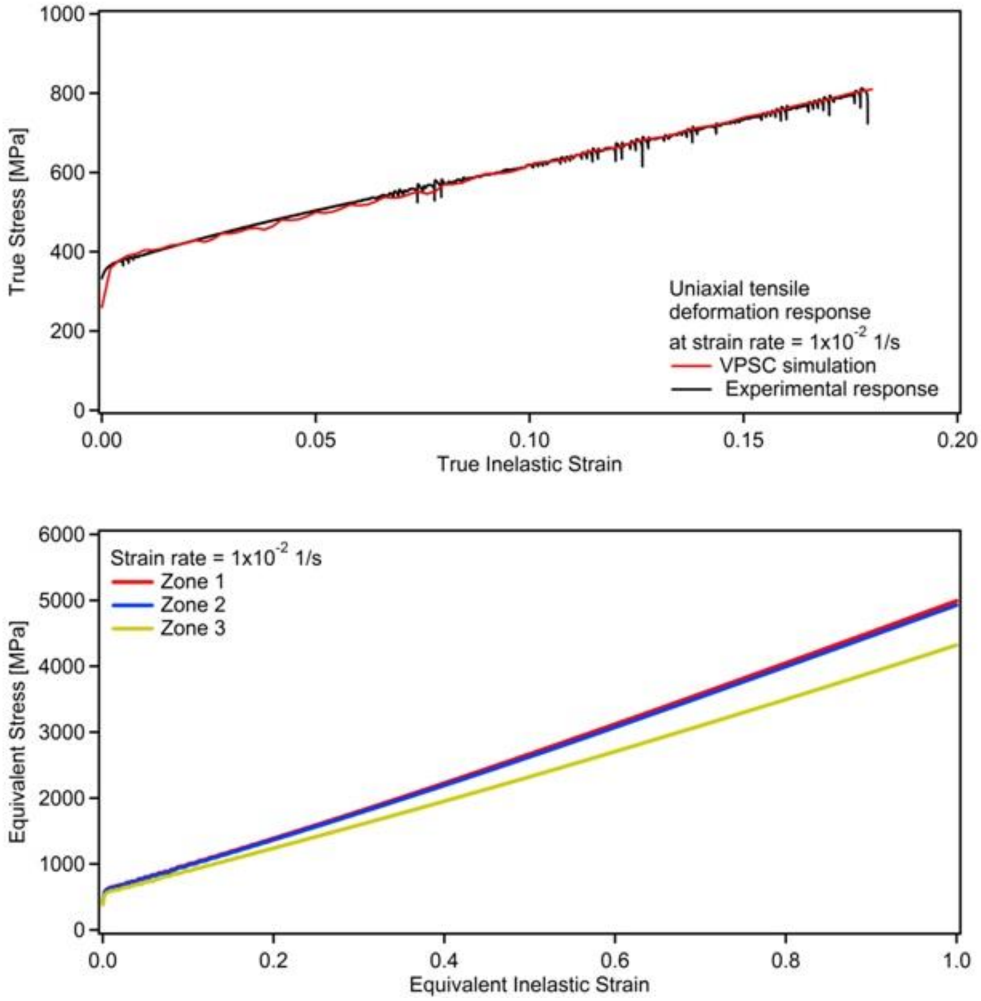

Figure 5. 6 Top: VPSC simulation of the RT experimental uniaxial tensile deformation of Hadfield steel at a strain rate of 1×10^{-2} 1/s. Bottom: the corresponding predicted equivalent stress-strain response for each zone within the impact sample based on the distribution of stress concentration (Figure 5.4) [23].

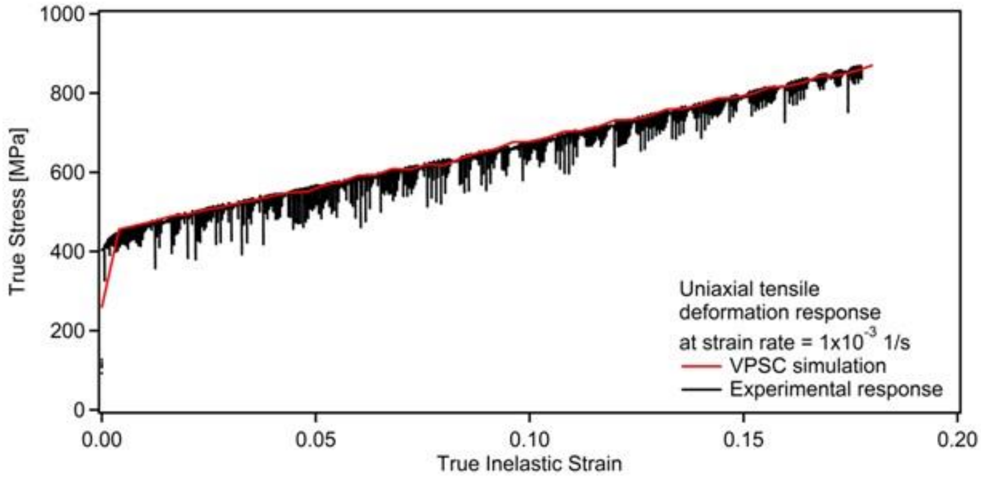

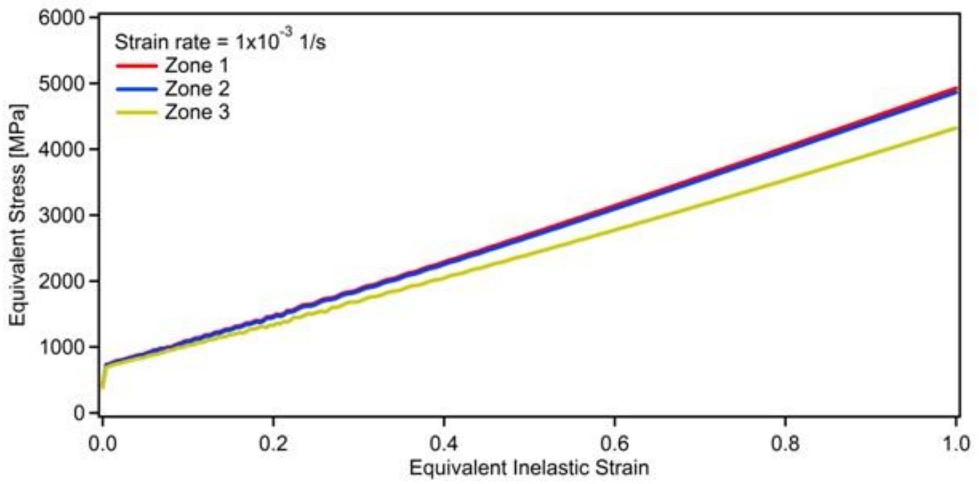

Figure 5. 7 Top: VPSC simulation of the RT experimental uniaxial tensile deformation of Hadfield steel at a strain rate of 1×10^{-3} 1/s. Bottom: the corresponding predicted equivalent stress-strain response for each zone within the impact sample based on the distribution of stress concentration (Figure 5.4) [23].

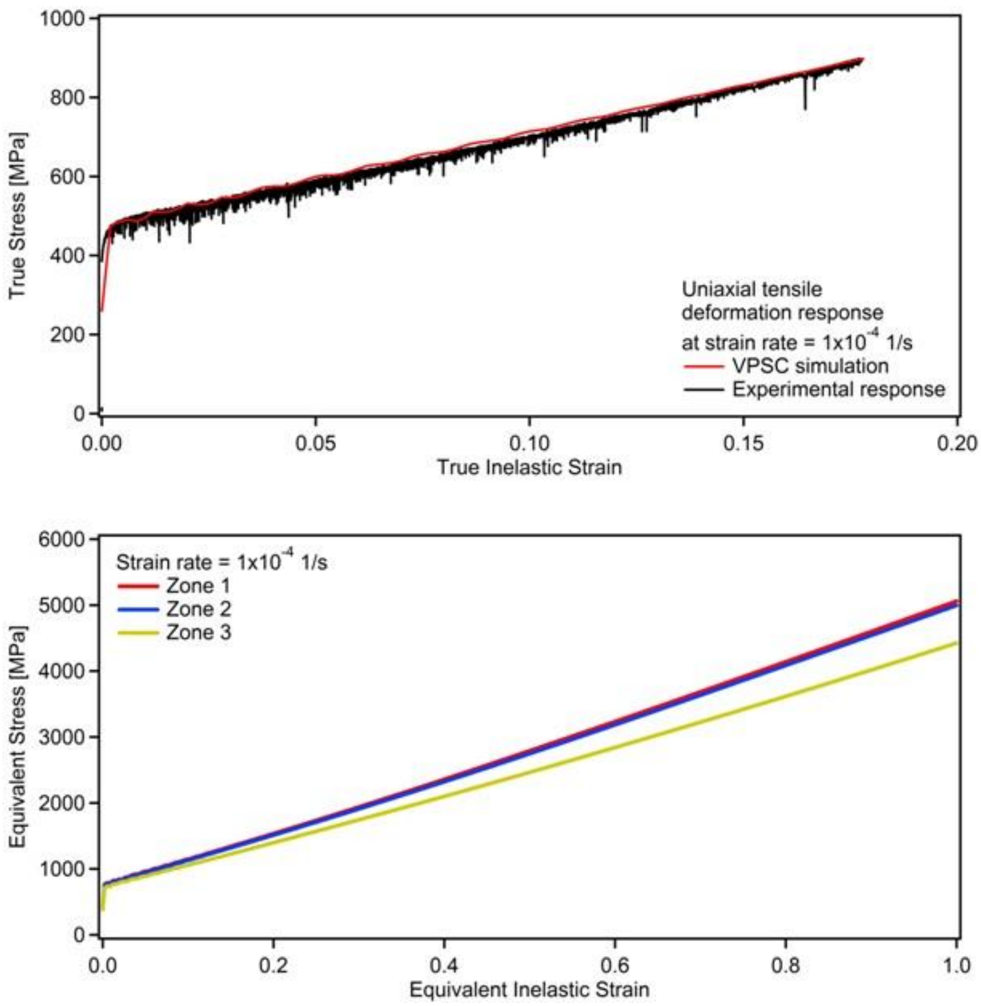

Figure 5. 8 Top: VPSC simulation of the RT experimental uniaxial tensile deformation of Hadfield steel at a strain rate of 1×10^{-4} 1/s. Bottom: the corresponding predicted equivalent stress-strain response for each zone within the impact sample based on the distribution of stress concentration (Figure 5.4) [23].

The VPSC algorithm employed in the current study was explained in detail in chapter 2. The current VPSC model was employed to solve for the stresses corresponding to the given strains throughout the deformation. The experimentally determined initial texture of Hadfield steel (inset of Figure 5.5) was utilized as input, and the macroscopic deformation responses were predicted as presented in Figures 5.5-5.8 for all the strain rates considered in this work. The corresponding Voce hardening parameters for each strain rate are provided in Table 5.1.

Table 5.1 Voce hardening parameters utilized in the current VPSC simulations.

Strain rate (1/s)	τ_0 *[MPa]*	τ_1 *[MPa]*	θ_0 *[MPa]*	θ_1 *[MPa]*
1×10^{-1}	132	925	53×10^{4}	350
1×10^{-2}	132	147	43×10^{3}	408
1×10^{-3}	132	1580	60×10^{4}	390
1×10^{-4}	132	918	55×10^{4}	398

In order to define a proper hardening rule for the FE simulations of the impact deformation, the current VPSC model was employed to predict the equivalent stress-strain response of Hadfield steel based on the uniaxial deformation responses at all four strain rates considered herein (Figures 5.5-5.8). Specifically, the successful prediction of the experimental data (Figures 5.5-5.8) is a strong indication that the materials' deformation was successfully modeled at the micro-deformation level, and therefore, the same VPSC model was utilized to predict the equivalent stress-strain response for each strain rate utilizing the same hardening parameters for each strain rate. Since the material-independent consideration of the stress-strain distribution under impact loading (Figure 5.4) had also demonstrated that the distribution of stresses and strains throughout the sample is heterogeneous, the FE mesh for each sample was divided into three different zones with three different flow rules (Figure 5.4), such that a more homogeneous stress-strain distribution can be obtained within each zone upon impact loading. Therefore, the VPSC model was utilized to predict the corresponding equivalent stress-strain state response for each zone at all four strain rates (Figures 5.5-58). Specifically, the same hardening parameters as in the VPSC model predicting the experimental uniaxial deformation response were employed in all three simulations for each strain rate. The corresponding deformation of the polycrystalline aggregate within each zone was defined to the VPSC algorithm through velocity gradient tensors, which were determined based on the material-independent strain distributions under impact loading (Figure 5.4). The corresponding velocity gradient tensors for each zone were computed as:

$$\dot{U}_1 = \begin{bmatrix} 4.2 & 1.0 & 0 \\ 1.0 & -2.1 & 0 \\ 0 & 0 & -2.1 \end{bmatrix},$$

$$\dot{U}_2 = \begin{bmatrix} 3.0 & 1.0 & 0 \\ 1.0 & -1.5 & 0 \\ 0 & 0 & -1.5 \end{bmatrix} \text{ and}$$

$$\dot{U}_3 = \begin{bmatrix} 0.3 & 1 & 0 \\ 1 & -0.15 & 0 \\ 0 & 0 & -0.15 \end{bmatrix}$$

for zones 1, 2 and 3, respectively [17].

The corresponding VPSC simulation results demonstrating the equivalent for each zone are presented in Figures 5.5, 5.6, 5.7 and 5.8 for the strain rates of 1×10^{-1} 1/s, 1×10^{-2} 1/s, 1×10^{-3} 1/s and 1×10^{-4} 1/s, respectively. It should be noted that the strength levels attained by the equivalent deformation curves for each strain rate follows the same trend as that of the experimental uniaxial curves. This is not surprising since both the plastic deformation and the hindering of dislocations by diffusing C atoms are considered at the slip system level, where the latter leads to NSRS in Hadfield steel. Moreover, for each strain rate, higher stresses were obtained for zone 1 as compared to zones 2 and 3, and zone 3 exhibited the lowest stress levels (Figures 5.5-5.8), which stands in good agreement with the stress intensities demonstrated in Figure 5.4, where the stresses decrease as one moves from zone 1 that contains the notch towards zone 3 with the least stress concentration factors.

The results of the FE simulations incorporating the roles of microstructure and NSRS texture through crystal plasticity are presented in Figure 5.9. Even though the predictions are much better for all strain rates as compared to those of the initial FE simulations that defined hardening based on the experimental uniaxial deformation response only (Figures 5.2 and 5.3), there is an important difference between the two cases in terms of strain rate dependence. Specifically, the results of the initial simulations revealed that the best predictions were obtained by defining the flow rule for Hadfield steel based on the uniaxial deformation response recorded at the highest strain rate (1×10^{-1} 1/s in the current work), in addition to the fact that the worst predictions were based on the flow rules defined within the NSRS range. Upon incorporation of microstructure into the FE model through crystal plasticity, however; it was evident that the best prediction was obtained by defining the flow rule based on the VPSC predictions of the equivalent stress-strain response at 1×10^{-2} 1/s (Figure 5.9), which is the second highest strain rate and within the NSRS range (Figure 5.1). This contradictory result clearly demonstrates that reliable predictions can be obtained by proper coupling of crystal plasticity and FE analysis even if the experimental flow rule of the material is acquired under uniaxial loading and at strain rates that fall within the NSRS range. This is especially important in terms of utilizing standard laboratory experiments to characterize a material's fundamental properties, which are simple and may be restricted to strain rates within the NSRS owing to practical limitations, while predicting its deformation response under complicated loading scenarios, such as impact loading.

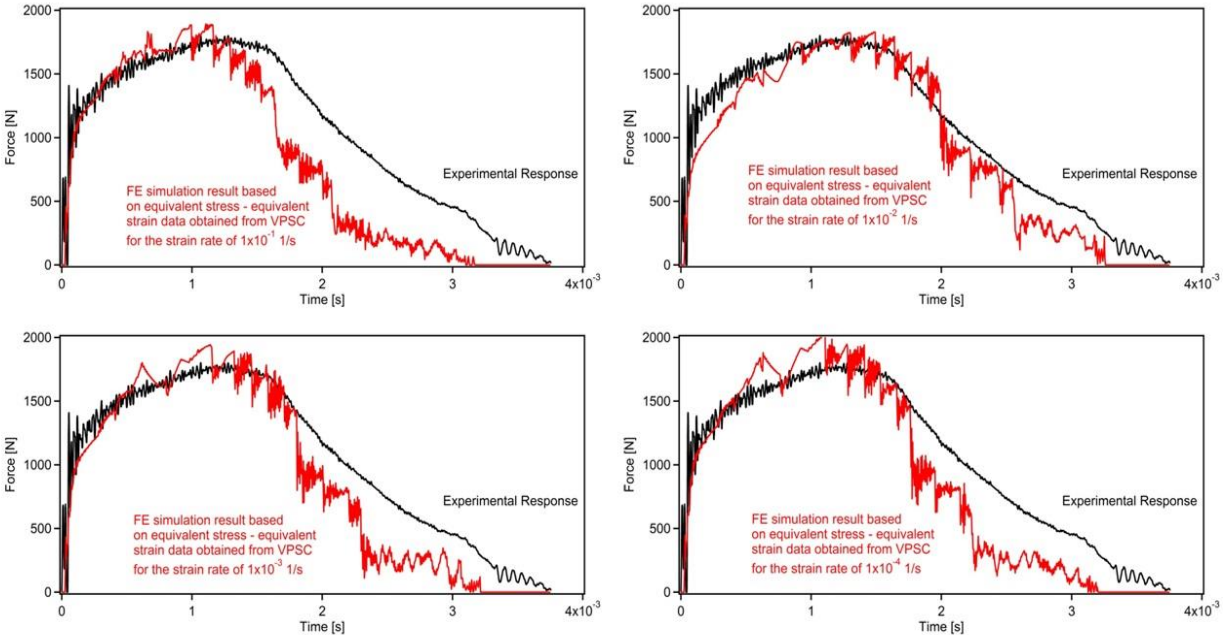

Figure 5. 9 Comparison of the experimental impact response and results of the FE simulations incorporating equivalent stress-strain responses predicted by crystal plasticity for all strain rates considered [23].

5.4 Conclusions

The room temperature impact response Hadfield steel was studied with the aid of a multi-scale modeling approach coupling crystal plasticity and finite element (FE) analysis. The roles of texture, geometry and strain rate sensitivity were successfully taken into account all at once, where crystal plasticity was utilized to obtain the multi-axial flow rule at different strain rates based on the experimental deformation response under uniaxial tensile loading. The FE simulation results demonstrated that the utility of equivalent stress – equivalent strain response for defining the hardening rule under impact loading resulted in improved predictions. Interestingly, the simulation results indicated that a multiaxial definition of the material flow rule is the major parameter dictating the success of the predictions of impact loading deformation even in the presence of negative strain rate sensitivity, as in the case of Hadfield steel. Finally, the current set of results also demonstrated that reliable predictions can be obtained by proper coupling of crystal plasticity and FE analysis even if the experimental flow rule of the material is acquired under uniaxial loading and at moderate strain rates that are significantly slower than those attained during impact loading. This observation opens the venue for utilizing more practical and simpler laboratory experiments to characterize a material's fundamental properties while predicting its deformation response under complicated loading scenarios, such as impact loading.

5.5 References

[1] W. S. Owen, M. Grujicic, Strain aging of austenitic Hadfield manganese steel, Acta Materialia 47 (1999) 111

[2] O. Bouaziz, S. Allain, C.P. Scott, P. Cugy, D. Barbier, High manganese austenitic twinning induced plasticity steels: A review of the microstructure properties relationships, Current Opinion in Solid State and Materials Science 15 (2011) 141

[3] E. Bayraktar, F. A. Khalid, C. Levaillant, Deformation and fracture behaviour of high manganese austenitic steels, Journal of Materials Processing Technology 147 (2004) 145

[4] T. Niendorf, F. Rubitschek, H.J. Maier, J. Niendorf, H.A. Richard, A. Frehn, Fatigue crack growth – microstructure relationships in a high-manganese austenitic TWIP steel, Materials Science and Engineering A 527 (2010) 2412

[5] T. Niendorf, C. Lotze, D. Canadinc, A. Frehn, H.J. Maier, The role of monotonic pre-deformation on the fatigue performance of a high-manganese austenitic TWIP steel, Materials Science and Engineering A 499 (2009) 518

[6] I. Karaman, H. Sehitoglu, K. Gall, Y. I. Chumlyakov, H. J. Maier, Deformation of single crystal Hadfield steel by twinning and slip, Acta Materialia 48 (2000) 1345

[7] I. Karaman, H. Sehitoglu, Y.I. Chumlyakov, H.J. Maier, I.V. Kireeva, Extrinsic stacking faults and twinning in Hadfield manganese steel single crystals, Scripta Materialia 44 (2001) 337

[8] R. Ueji, N. Tsuchida, D. Terada, N. Tsuji, Y. Tanaka, A. Takemura, K. Kunishige, Tensile properties and twinning behavior of high manganese austenitic steel with fine-grained structure, Scripta Materialia 59 (2008) 963

[9] B. Hutchinson, N. Ridley, On dislocation accumulation and work hardening in Hadfield steel, Scripta Materialia 55 (2006) 299

[10] S.M. Toker, D. Canadinc, A. Taube, G. Gerstein, H.J. Maier, On the role of slip-twin interactions on the impact behavior of high-manganese austenitic steels, Materials Science and Engineering A 593 (2014) 120

[11] D. Canadinc, H. Sehitoglu, H.J. Maier, Y.I. Chumlyakov, Strain hardening behavior of aluminum alloyed Hadfield steel single crystals, Acta Materialia 53 (2005) 1831

[12] D. Canadinc, H. Sehitoglu, H.J. Maier, The role of dense dislocation walls on the deformation response of aluminum alloyed Hadfield steel polycrystals, Materials Science and Engineering A 454 (2007) 662

[13] D. Canadinc, C. Efstathiou, H. Sehitoglu, On the negative strain rate sensitivity of Hadfield steel polycrystals, Scripta Materialia 59 (2008) 1103

[14] Y.H. Wen, H.B. Peng, H.T. Si, R.L. Xiong, D. Raabe, A novel high manganese austenitic steel with higher work hardening capacity and much lower impact deformation than Hadfield manganese steel, Materials and Design 55 (2014) 798

[15] S. Xu, D. Ruan, J.H. Beynon, Y. Rong, Dynamic tensile behavior of TWIP steel under intermediate strain rate loading, Materials Science and Engineering A 573 (2013) 132

[16] J.S. Jeong, W. Woo, K.H. Oh, S.K. Kwon, Y.M. Koo, In situ neutron diffraction study of the microstructure and tensile deformation behavior in Al-added high manganese austenitic steels, Acta Materialia 60 (2012) 2290

[17] O. Onal, B. Bal, S.M. Toker, M. Mirzajanzadeh, D. Canadinc, H.J. Maier, Microstructure-based modeling of the impact response of a biomedical niobium–zirconium alloy, Journal of Materials Research 29 (2014) 1123

[18] Jr. J.W. Morris, Stronger tougher steels, Science 320 (2008) 1022

[19] R. Song, D. Ponge, D. Raabe, Mechanical properties of an ultrafine grained C–Mn steel processed by warm deformation and annealing, Acta Materialia 53 (2005) 4881.

[20] Y. Kimura, T. Inoue, F. Yin, K. Tsuzaki, Inverse temperature dependence of toughness in an ultrafine grain-structure steel, Science 320 (2008) 1057

[21] K. Kormi, D.C. Webb, W. Johnson, The application of the FEM to determine the response of a pretorsioned pipe cluster to static or dynamic axial impact loading, Computers and Structures 62 (1997) 353

[22] S.L. Raykhere, P. Kumar, R.K. Singh, V. Parameswaran, Dynamic shear strength of adhesive joints made of metallic and composite adherents, Materials and Design 31 (2010) 2102

[23] O.Onal, C.Ozmenci, D.Canadinc, Multi-scale modeling of the impact response of a strain-rate sensitive high-manganese austenitic steel, Frontiers in Materials (Section: Computational Materials Science) 1 (2014) 16

[24] D. Canadinc, E. Biyikli, T. Niendorf, H.J. Maier, Experimental and numerical investigation of the role of grain boundary misorientation angle on the dislocation – grain boundary interactions, Advanced Engineering Materials 13 (2011) 281

[25] D. Canadinc, H. Sehitoglu, H.J. Maier, P. Kurath, On the incorporation of length scales associated with pearlitic and bainitic microstructures into a visco-plastic self-consistent model, Materials Science and Engineering A 485 (2008) 258

[26] R.A. Lebensohn, C.N. Tomé, A self-consistent anisotropic approach for the simulation of plastic deformation and texture development of polycrystals: Application to zirconium alloys, Acta Metallurgica et Materialia 41 (1993) 2611

[27] U.F. Kocks, C.N. Tomé, H.R. Wenk, Texture and anisotropy (1998) Cambridge University Press: New York.

[28] E. Biyikli, D. Canadinc, H.J. Maier, T. Niendorf, S. Top, Three-dimensional modeling of the grain boundary misorientation angle distribution based on two-dimensional experimental texture measurements Materials Science and Engineering A 527 (2010) 5604

CHAPTER 6: CONCLUSIONS

The motivation of the current work was to investigate thickness reduction and crack initiation sites in PHE’s utilized in combi boilers during die forming operation. The zones of reduced thickness are considered as perfect crack initiation sites. This inhomogeneity based on the process could lead to catastrophic failure in the PHE’s, significantly shortening their service life. In order to overcome this problem, a multi-scale modeling approach was adopted that includes proper coupling of crystal plasticity and FE analysis. Specifically, the role of anisotropy and microstructure were considered by incorporating multi-axial material hardening rule obtained from crystal plasticity modeling into the FE forming simulations (Chapter 2). The findings of this analysis demonstrated the success of the multi-scale modeling approach in predicting the thickness reduction and crack initiation sites during die forming. However, it was evidenced in this analysis that undesired failure of PHE’s can be prevented during forming operation.

The crack initiation phenomenon was extended to rail steels (pearlitic and bainitic steel) in the following chapter. One should note that railroad industry is considerably benefited in terms of costs by prolonging rail life. For this purpose, the deformation behavior of both steels was investigated under rolling contact loading utilizing JS model. The crack initiation life of both steels was predicted considering ratcheting and multi-axial fatigue damage in the JS model (Chapter 3). These results exhibited that bainitic steel is preferable over pearlitic steel when the shear tractions are low whereas their performances showed proximity as the shear tractions ascended. Another important consequence was that the crack initiation was controlled by fatigue damage when shear tractions are low but ratcheting damage governed the crack initiation with increasing loads. This analysis indicated that realistic prediction of crack initiation under rolling contact was successfully made by this methodology.

The utilization of multi-scale modeling approach was extended to predict the impact response of a biomedical Nb-Zr alloy considering the microstructure – mechanical property relationship. It is noteworthy that Nb-Zr alloy is a potential implant material and implants are subjected to impact loading in the case of falling or jumping. Therefore, understanding the impact response is vital for safety of the implant material during service. For this purpose, the impact response of coarse grained and ultrafine-grained Nb-Zr alloys were investigated with proper coupling of crystal plasticity modeling and FE analysis. In particular, the effects of texture and geometry based distribution of stresses and strains were accounted for by incorporating multi-axial hardening rule acquired from crystal plasticity modeling into the FE analysis (Chapter 4). This analysis clearly showed that combined experimental and computational approach was successful in predicting the impact response when compared with experimental findings. This evidences that microstructure has a significant influence on the impact response of metallic implants. A notable consequence is that mechanical failure of implants can be prevented at the design process by considering anisotropy and microstructure.

For the purpose of further analysis of microstructure-mechanical property relationship, the utility of multi-scale modeling approach was extended to predict the room temperature impact response of a conventional metallic material, high manganese austenitic steel. This type of steel is strain rate sensitive and is an important member of structural metallic materials having a complex deformation behavior. Furthermore, this steel is commonly used in automotive industry, load-bearing and ballistic applications which require high impact resistance. Specifically, in this analysis, the effects of texture, geometry and strain rate sensitivity were considered by implementing multi-axial hardening rule at different strain rates regarding experimental uniaxial deformation behavior acquired from crystal plasticity simulations into the FE analysis (Chapter 5). The results showed that improved impact predictions were observed with the utility of appropriate hardening rule. It was also evidenced that appropriate coupling of crystal plasticity and FE simulations was necessary for accurate impact predictions.

Overall, the current thesis indicated that multi-scale modeling approach presented herein is of great importance in order to predict deformation behavior of metallic materials considering microstructural effects. This approach constitutes an important guideline for the design of new materials as a result of decreasing manufacturing costs. Eventually, understanding the microstructure-mechanical property relationship in metallic materials is of utmost significance for safety and adequate service life.

Part of the study was dedicated to the thickness reduction problem in plate heat exchangers in forming operation. Considering large plastic strains in metal forming, the deformation response of plate heat exchangers can be investigated under cyclically applied thermal and mechanical loads. This loading type provides information about evolution of accumulated plastic strains and residual stresses such that fatigue life of PHE’s can be estimated. Specifically, crack initiation prediction under fatigue loading can be made utilizing semi-analytical Jiang-Sehitoglu model. Hence, a scientific methodology is planned to be introduced to predict the fatigue response of metallic materials under thermo-mechanical loading.

Major part of the thesis demonstrated the need for multi-scale modeling approach in order to predict the deformation behavior of structural and biomedical materials. This multi-scale modeling approach is applicable to various materials under any type of complicated loading scenario once appropriate coupling of crystal plasticity and finite element analysis is achieved. Future work involves the application of this new multi-scale approach to different classes of alloys, especially biomedical alloys, where the design procedure of implants and other biomedical tools can vastly benefit from such realistic numerical analyses.